Institute of Physics
Polish Academy of Sciences

Tomasz Świetlik

LASER DIODES BASED ON GALLIUM NITRIDE - INVESTIGATION OF CARRIER INJECTION MECHANISMS, GAIN AND DISTRIBUTION OF THE ELECTROMAGNETIC FIELD

PH.D. DISSERTATION WRITTEN UNDER THE SUPERVISION OF
doc. dr hab. PIOTR PERLIN
AT
INSTITUTE OF HIGH PRESSURE PHYSICS
POLISH ACADEMY OF SCIENCES

Warsaw 2008

Table of Contents

Acknowledgements

I am grateful to everyone whose involvement contributed to the successful completion of this work.

In particular, I would like to thank doc. dr hab. Piotr Perlin, my supervisor, for his many suggestions and constant support during this research. I am also thankful to prof. Tadeusz Suski for his guidance through all years of my scientific work.

I would also like to thank the following:

– Gijs Franssen and Szymon Grzanka for countless discussions and useful remarks

– Przemek Wiśniewski and Alexander Khachapuridze for help and instructions during my experimental work

– Henryk Teisseyre for a productive cooperation in optical laboratory

– Robert Czernecki, Grzegorz Targowski, Michał Leszczyǹski, Paweł Prystawko, Czesław Skierbiszewski, Marcin Siekacz, Ania Feduniewicz-Żmuda for providing samples investigated in this work

– Kasia Komorowska, Łucja Marona, Jurek Plesiewicz for a nice atmosphere and cooperation

– Ulrich Schwarz for offering the opportunity to visit Regensburg University and perform SNOM measurements

– prof. Saulius Juršėnas and Saulius Miasojedovas for a warm welcome at Vilnius University and support in time-resolved spectral analysis

– Dionyz Pogany and Sergey Bychikhin for performing scans using TIM technique at the University of Vienna

– Tomasz Ochalski from University College Cork for help in collection high resolution electroluminescence spectra of laser devices

– Irena Makarowa, Wiktor Krupczyǹski, Renata Wis̀niewska for the sample preparation

– All colleagues at the Semiconductor Laboratory of Unipress and TopGaN company for their support and goodwill

I also want to thank Roma for her love and constant support and my family members. Without their engagement and patience this work would never have come into existence.

Subject and the major goals of the dissertation

Rapid development made recently in the technology of III-nitride semiconductors lead to a few important breakthroughs that enabled a successful commercialization of efficient blue light emitters. Despite many efforts devoted to investigate basic physical phenomena governing the operation of nitride-based optoelectronic devices, there is still a considerable amount of knowledge that has not been unveiled until now.

The following dissertation is devoted to yield information on the major physical mechanisms that influence the external parameters of laser diodes fabricated at Institute of High Pressure Physics of Polish Academy of Sciences. The unique features of these devices rely greatly on an original concept regarding deposition of all epitaxial layers on the native bulk GaN crystals. These substrate crystals are grown by a unique technique of a high pressure synthesis. They boast their advantages over commonly used SiC, Al_2O_3 and overgrown GaN in terms of either quality, electrical and thermal conductivity or lattice mismatch.

Throughout the following dissertation we will try to deal with all the major aspects of the device features grown homoepitaxially on the high pressure GaN substrates. The material will be divided into two major parts. We will start with the background concerning physical mechanisms and peculiarities of nitride-based devices. Subsequently, the experimental data and a detailed analysis will be presented.

In Chapter 2 we will briefly go through the principles of a semiconductor laser operation and define the major device parameters that will be related to later on. Specific features and constrains of the nitride technology such as the inhibited charge transport, excess internal electric fields, peculiarities of the thermal management as well as the role and importance of the structural quality of an active material will be also introduced and discussed in

Chapter 3.

Chapter 4 will acquaint the reader with the structural details of the samples used in the following research. In particular, we will discuss the pre-growth substrate preparation procedure, the design and a sequence of the epitaxial layers consisting of (InAl)GaN compounds and the final device processing. We will then go over specific features of two alternative growth techniques, i.e. MOCVD and MBE, in terms of growth temperatures, rates and film quality. Both of them claim their position at the cutting edge of the nitride technology, despite some initial superiority of MOCVD.

The experimental part will be divided into two major sections. First of all, the microscopic phenomena that take place within the active region will be considered including carrier injection and recombination. In Chapter 5 major issues regarding carrier transport and quantum well confinement will be analyzed. The influence of the quantum well and barrier width, electron blocking layer and inhomogeneous carrier distribution on the device's thermal stability will be studied. Some of the obtained results remain contrary to the intuitive knowledge derived from other material systems. They will be explained specifically on grounds of the nitride technology, dealing with the concepts of the ballistic transport and inhomogeneous carrier injection. Subsequently, Chapter 6 will undertake the problems of the radiative recombination and optical gain in laser structures with different quantum well indium content grown by MOCVD, which is still regarded as the major growth technique. From the optical measurements we will also derive values of internal propagation losses. This analysis will be followed by a comparative study of optical properties determined for a similar laser structures grown alternatively by MOCVD and MBE.

Starting from Chapter 7, more macroscopic phenomena will be dealt with. We will try to investigate details of the heat management, identify the major regions generating excess Joule heat and determine thermal resistance of different packaging schemes by means of the infrared thermography. In turn, Chapter 8 will consider aspects of the spatial and temporal evolution of resonant cavity modes. Using near-field optical microscopy we will discuss the problems of filamentation, antiguiding and mode leakage into the lossy bulk GaN substrate.

Finally, based on the analysis of a true spontaneous emission spectra, Chapter 9 estimates the value of the material gain necessary to reach lasing and suggests some possible device optimization steps concerning the length of the resonant cavity and the quantum well number.

The results presented throughout this dissertation have been published in the following articles:

1. T. Świetlik, G. Franssen, C. Skierbiszewski, R. Czernecki, P. Wiśniewski, M. Kryśko, M. Leszczyński, I. Grzegory, P. Mensz, S. Juršėnas, T. Suski, and P. Perlin, ***"Comparison of gain in group-III-nitride laser structures grown by metalorganic vapour phase epitaxy and plasma-assisted molecular beam epitaxy on bulk GaN substrates"***, Semicond. Sci. Technol. **22**, 736 (2007)

2. T. Świetlik, G. Franssen, R. Czernecki, M. Leszczyński, C. Skierbiszewski, I. Grzegory, T. Suski, P. Perlin, C. Lauterbach, and U. T. Schwarz, ***"Mode dynamics of high power (InAl)GaN based laser diodes grown on bulk GaN substrate"***, J. Appl. Phys. **101**, 083109 (2007)

3. T. Świetlik, P. Perlin, T. Suski, M. Leszczyński, R. Czernecki, I. Grzegory, and S. Porowski, ***"Optical gain and saturation behavior in homoepitaxially grown InGaN/GaN/AlGaN laser structures"***, Phys. Status Solidi (c) **4**, 82 (2007)

4. T. Świetlik, C. Skierbiszewski, R. Czernecki, G. Franssen, P. Wiśniewski, M. Leszczyński, I. Grzegory, P. Mensz, T. Suski, and P. Perlin, ***"Comparison of optical properties of InGaN/GaN/AlGaN laser structures grown by MOVPE and MBE"***, Proc. SPIE **6473**, 64731E (2007)

5. S. Bychikhin, T. Świetlik, T. Suski, S. Porowski, P. Perlin, and D. Pogany, ***"Thermal analysis of InGaN/GaN (GaN substrate) laser diodes using transient interferometric mapping"***, Microelecronics Reliability **47**, 1649 (2007)

6. T. Świetlik, G. Franssen, P. Wiśniewski, S. Krukowski, S. P. Łepkowski, Ł. Marona, M. Leszczyński, P. Prystawko, I. Grzegory, T. Suski, S. Porowski, and P. Perlin, ***"Anomalous temperature characteristics of single wide quantum well InGaN laser diode"***, Appl. Phys. Lett. **88**, 071121 (2006)

7. P. Perlin, T. Suski, M. Leszczyński, P. Prystawko, T. Świetlik, Ł. Marona, P. Wiśniewski, R. Czernecki, G. Nowak, J.L. Weyher, G. Kamler, J. Borysiuk, E. Litwin-Staszewska,

L. Dmowski, R. Piotrzkowski G. Franssen, S. Grzanka, I. Grzegory, and S. Porowski, ***"Properties of InGaN blue laser diodes grown on bulk GaN substrates"***, J. Cryst. Growth **281**, 107 (2005)

Other papers published in international journals:

8. K. Komorowska, P. Wiśniewski, R. Czernecki, M. Leszczyński, T. Suski, I. Grzegory, S. Porowski, S. Grzanka, T. S̀wietlik, Ł. Marona, T. Stacewicz, and P. Perlin, ***"16 nm tuning range of blue InGaN laser diodes achieved by 200 K temperature increase"***, Proc. SPIE **6894**, 68940Q (2008)

9. P. Perlin, P. Wis̀niewski, R. Czernecki, P. Prystawko, M. Leszczyǹski, T. Suski, I. Grzegory, Ł. Marona, T. S̀wietlik, K. Komorowska, and S. Porowski, ***"Load dislocation density broad area high power CW operated InGaN laser diodes"***, Proc. SPIE **6184**, 61840H (2006)

10. P. Wis̀niewski, R. Czernecki, P. Prystawko, M. Maszkowicz, M. Leszczyǹski, T. Suski, I. Grzegory, S. Porowski, Ł. Marona, T. S̀wietlik, and P. Perlin, ***"Broad-area high-power CW operated InGaN laser diodes"***, Proc. SPIE **6133**, 61330Q (2006)

11. P. Perlin, Ł. Marona, T. S̀wietlik, M. Leszczyǹski, P. Prystawko, P. Wis̀niewski, R. Czernecki, G. Franssen, S. Grzanka, G. Kamler, J. Borysiuk, J. Weyher, I. Grzegory, T. Suski, S. Porowski, T. Riemann, and J. Christen, ***"Properties of violet laser diodes grown on bulk GaN substrates"***, Proc. SPIE **5738**, 72 (2005)

12. R. Czernecki, G. Franssen, T. Suski, T. S̀wietlik, J. Borysiuk, S. Grzanka, P. Lefebvre, M. Leszczyǹski, P. Perlin, I. Grzegory, and S. Porowski, ***"Localization effects in InGaN/GaN double heterostructure laser diode structures grown on bulk GaN crystals"***, Jap. J. Appl. Phys. **44**, 7244 (2005)

Chapter 1

Introduction

1.1 Laser diodes and their applications

Over the recent years semiconductor laser diodes (LDs) have become one of the most popular type of laser devices. Their widespread applicability, portability and potential commercial perspectives have drawn a focussed attention of many research groups and companies worldwide beginning from the early 60'ies.

During decades light-emitting diodes (LEDs) started to be regarded as a perfect light source for displays because of high brightness, durability and limited power consumption. On the other hand, LDs have found applications in many different areas of every-day life such as compact disc players, optical communication systems, printing devices, contaminant sensing or photosensitive medical treatment and surgery.

Rapid development of the above-mentioned applications would go even further if it where not for the lack of materials that emit blue light efficiently. Shifting the energy of laser emission toward higher values was anxiously looked forward. Despite its advantageous impact on spectroscopic applications, optical storage systems and display technology would also potentially benefit which was even more desirable and profitable from a commercial point of view [1].

The diffraction limit which establishes inverse proportionality between the square of the wavelength and a focusing spot size leads straightforwardly to a conclusion that a shorter wavelength can be focused more sharply. Thus increased storage capacity of optical discs, improved resolution of printing devices and more precise positioning of medical treatment are only a few potential advantages to be named. Additional benefits from blue-shifting of laser emission originate from the fact that many biochemical reagents, pollutants and drugs have optimum response frequency in a spectral region covering a wavelength range between 380-490 nm.

Three primary colors (red, green and blue) needed for efficient white-light emitters, full-color displays or a future type of LD-based TV sets required the usage of material systems with different band gap energy. III-V compounds such as AlGaAs or GaInP have proven to be advantageous in the red color range. On the other hand, II-VI materials were originally considered as a promising emitters in green and blue spectral regions. However, CdZnSe (green spectral range) and ZnSe (blue spectral range) suffered from very short lifetimes and never reached maturity. Finally GaN, AlN and InN and their solid solutions became the materials of choice for short-wavelength optoelectronics [2]. The room-temperature band gap energy of AlGaInN compounds varies between 0.7 eV for pure InN through 3.4 eV for GaN up to 6.2 eV for AlN and can be easily controlled by alloy composition. This material system not only have direct band gap, covers the large spectrum of emission wavelengths from infrared to near ultraviolet but also is characterized by such properties as an excellent thermal conductivity (1.3 W $cm^{-1}\,K^{-1}$ for GaN versus 0.55 W $cm^{-1}\,K^{-1}$ for GaAs [3]) as well as a physical and chemical stability, which are equally important for practical applications.

1.2 Milestones in early nitride research

The first major problem that had to be dealt with in nitride-related technology was a lack for a proper, lattice-matched substrate for the subsequent deposition of III-nitride compounds. Although GaN was synthesized for the first time in the early years of condensed matter research [4], it was extremely difficult to obtain large, high quality bulk GaN crystals due to its thermodynamic properties setting very high melting temperature around 2490°C achieved under the equilibrium nitrogen pressure of 60 kbar [5]. Due to these unfavorable conditions, III-nitride compounds could not be grown from a stoichiometric melt by the Czochralski or Bridgman methods commonly used in other material systems.

This fact turned the attention of engineers involved in design of optoelectronic devices towards other substrate materials, which could be obtained more easily. Sapphire turned out to be the most important one, despite the lack of a total compatibility to GaN in terms of a lattice constant and the thermal expansion coefficient.

First high quality GaN layers on sapphire were obtained in the 60'ies from a vapor phase by Hydride Vapor Phase Epitaxy (HVPE) [6]. In this method gallium was transported as a chloride after a reaction with HCl. Alternatively, nitrogen was obtained from NH_3 at the growth temperature of 900℃. High concentration of electrons in GaN crystals was revealed due to unintentional contamination with oxygen. The attempts to achieve p-type conductivity failed. High background electron concentration, passivation of acceptors by hydrogen atoms and a low mobility of holes made it extremely difficult to obtain the net p-type conductivity in GaN. The development of the nitride technology was hampered for almost two decades.

It was not until the mid 80'ies, when the development of MOCVD technique marked the next milestone in the nitride technology. The usage of low temperature AlN [7, 8] and GaN [9] buffer layers led to a successful growth of high quality GaN films with mirror-like flat surfaces in spite of a 15% lattice mismatch between a sapphire substrate and GaN.

Another breakthrough was achieved by overcoming difficulties with obtaining p-type conductivity in GaN. Unavailability of p-type GaN films hampered the development of nitride-based devices until 1989 when Amano *et al.* obtained p-type GaN films using Mg as an acceptor impurity. Their approach to obtain p-type conductivity from initially highly resistive material was based on post-growth irradiation by a low-energy electron beam (LEEBI). The research was followed by a demonstration of the first III-nitride-system-based p-n junction light emitting diode (LED) [10].

From the very beginning, Mg was the most promising candidate for an effective acceptor impurity. However, large concentration of dopants was required due to the relatively high (between 150-250 meV in GaN) ionization energy limiting the fraction of activated acceptors to 1% at room temperature. Additionally, the MOCVD growth of the device's structure taking place in ammonia atmosphere promoted the formation of electrically inactive Mg-H complexes. The origin of the acceptor compensation mechanism was not correctly recognized until Nakamura *et al.* obtained p-type GaN films using post-growth thermal annealing in nitrogen atmosphere instead of ammonia [11, 12]. LEEBI treatment was not necessary anymore. Formation of neutral Mg-H complexes was identified as a major mechanism of acceptor compensation responsible for a resistivity increase of p-type films grown in ammonia atmosphere. The discovery was further confirmed by theoretical calculations by Neugebauer *et al.* [13].

Further improvement of the MOCVD technique, led to the deposition of a high quality InGaN films designed to form the active region of the blue light emitting devices. Using a novel two-flow MOCVD reactor Nakamura *et al.* [14] managed to grow an InGaN multiple quantum well (MQW) structure with enhanced photoluminescence intensity [15]. This was the starting point for the mass production technology of blue and green light emitting diodes (LEDs) deposited on the sapphire substrate.

After optimizing the growth technology and improving a structure design, the fist room temperature (RT) pulse-operated LD was demonstrated [16] followed by fabrication of the first III-nitride-system-based LD working in continuous wave (CW) regime [17]. Further improvements concerning a demonstration of strained AlGaN/GaN superlattices allowing for thicker cladding layers [18] and low defect density GaN substrates achieved by epitaxial lateral overgrowth (ELO) [19] enabled considerable prolongation of the device's lifetime and led to the successful commercialization of the entire production technology [20]. Finally, the elusive dream that for a few decades focused the attention of many scientists and engineers involved in optoelectronic industry came true.

Chapter 2

Principles of a semiconductor laser diode operation

2.1 Carrier and photon confinement

A semiconductor laser is a diode structure created by materials of the opposite (negative and positive) conductivity types. Once these materials are physically connected, the majority carriers start to diffuse along the concentration gradient leaving behind ionized donors and acceptors. The space charge formed by ionized dopants sets up the electric field directed oppositely to the direction of carrier diffusion. Processes of drift and diffusion continue until the equilibrium is reached, which is reflected in a bending of conduction and valence band profiles along the growth axis as a result of the formation of a constant Fermi level throughout the entire laser structure. The application of the forward bias disturbs the equilibrium. The net movement of carriers through the laser stack appears. The oppositely charged carriers generated by the electrical excitation need to recombine radiatively in the active region as depicted in Figure 2.1(a).

For low injection currents, light is emitted incoherently in a way that is similar to the LED case. In order to reach lasing action, one need to supply a sufficiently high concentration of carriers within the active region, which is necessary to induce the population inversion. Photons generated this way travel through epitaxial layers and induce further carrier recombination events. Under a sufficiently high excitation, an avalanche-like process of photon-stimulated optical recombination takes place. The device starts to act as an optical amplifier.

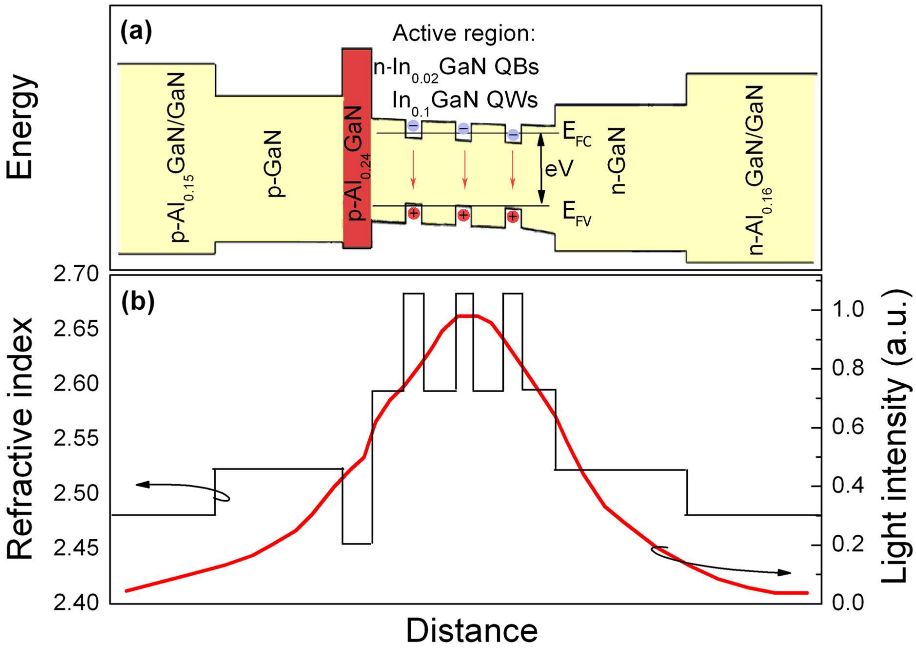

Figure 2.1: Schematic picture of the conduction and valence band profiles of a forwardly biased p-n junction (a); refractive index and light intensity distributions in transverse direction of a laser stack (b).

The effect of an optical amplification can be most efficiently accomplished by the utilization of a separate confinement heterostructure (SCH). The idea employs a concept of an independent confinement of injected carriers and emitted photons. In case of the nitride-based devices, the approach is carried out by a thin (within a nanometer range) active layer consisting of a series of thin InGaN quantum wells (QWs) and quantum barriers (QBs), which serve as a carrier confinement (See Figure2.1(a)). They are sandwiched between n- and p-type GaN-based optical waveguide and AlGaN/GaN superlattices used as cladding layers for an optical waveguide. Due to an increased excited carrier concentration, the probability of the radiative recombination also increases. Emitted photons are effectively guided in a transverse direction by a proper refractive index profile, which is high in the vicinity of QWs and decreases in the direction away from the active region (Figure 2.1(b)).

Resonant cavity established by reflecting facets at both ends of the device induces an

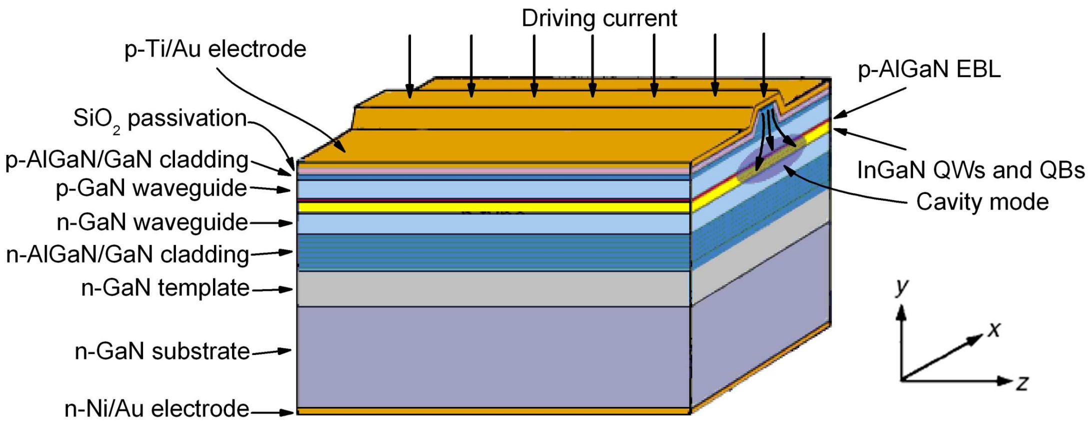

Figure 2.2: Schematic picture of an (InAl)GaN laser diode.

optical feedback. These facets are formed by a mechanical cleavage of the crystal along its crystallographic planes. If a net optical amplification is large enough to compensate for all possible optical losses, photons oscillating back and forth form a steady-state electromagnetic wave, which finally emerges out of the laser device as a coherent optical beam. A schematic picture of a practical realization of a laser device is depicted in Figure 2.2. A more detailed approach will be presented in Chapter 4 to fulfill the need of an overview of the studied samples.

2.2 Carrier injection and recombination

In every practical case, electrical current applied to device's contact electrodes plays a role of a source of excited carrier population established in the active region. Efficient carrier injection is one of the major factors necessary to approach specific conditions under which lasing occurs. After injection, as a consequence of the intraband carrier-carrier scattering, excess electrons and holes equilibrate instantly. Even under conditions of dynamic injection, occupation probabilities of ground (E_1) and excited states (E_2) follow Fermi-Dirac distribution functions as derived for a population of fermions under thermal equilibrium. Separate occupation levels for conduction (E_{FC}) and valence band (E_{FV}) established this way are usually separated by a little less than the voltage applied to the p-n junction (Figure 2.1(a)).

$$f_1 = \frac{1}{\exp\left[\frac{E_1 - E_{FV}}{kT}\right] + 1} \quad (2.2.1)$$

$$f_2 = \frac{1}{\exp\left[\frac{E_2 - E_{FC}}{kT}\right] + 1} \quad (2.2.2)$$

Charge neutrality principle requires that the total charge density in quantum well or in entire active region equals zero. Because quantum wells are usually undoped or lightly doped it can be assumed that electron concentration (N) equals hole concentration (P). Thus it is possible to extract information on a carrier density dependance of recombination mechanisms only by tracking solely the injected electron density.

2.3 Basic radiative transitions

Temporal dependance of the excited electron concentration can be enclosed in one carrier rate equation that takes into consideration all possible carrier recombination mechanisms taking place in unit active volume per unit time interval ($s^{-1}m^{-3}$):

$$\frac{dN}{dt} = G - R. \quad (2.3.1)$$

Carrier injection caused by applied electrical voltage enters through generation rate G. Total carrier recombination rate R depends in turn on many different recombination mechanisms consisting of the following recombination rates: spontaneous recombination (R_{sp}), net stimulated recombination (R_{st}), nonradiative recombination (R_{nr}) and carrier leakage (R_l).

$$R = R_{sp} + R_{st} + R_{nr} + R_l. \quad (2.3.2)$$

The first two terms contribute constructively to the formation of a coherent electromagnetic wave. Especially R_{st} which is the main photon generation term above threshold. On the other hand the latter two constitute a source of a carrier loss that needs to be efficiently suppressed as they deteriorate a device's performance.

2.3.1 Spontaneous Emission

Stimulated and spontaneous radiative recombination processes are of profound importance in understanding clearly the mechanisms of semiconductor gain in laser diode. Stimulated recombination occurs under the incidence of a real electromagnetic wave, while spontaneous emission is triggered by a vacuum field oscillations having a field strength equal to a strength of a real electromagnetic wave induced by one real photon. Downward transitions from excited to ground state create a new photon into the same optical mode as the stimulating one, no matter whether it is a real or a vacuum-field photon. The newly created photons appear not only in the same optical mode but also have the same phase contributing to the incident field constructively. As a result, the optical mode can build up as it travels along the active region and forms a coherent wave. Unfortunately, vacuum field phase is not correlated with phase of a real photon field. New photons introduced through spontaneous emission have random phases in contradiction to coherent field created by stimulated emission. Additionally, they are emitted uniformly into every direction of a solid angle. As a result, only a small fraction of them propagates along the waveguiding layers with a desired phase contributing to the formation of the lasing mode of the cavity. In order to take into account a fraction of a total amount of spontaneous emission that reinforces the mode of interest, the spontaneous emission factor β_{sp} is introduced which is roughly equal to the reciprocal of the total number of all possible modes in a resonant cavity.

Spontaneous emission spectrum is peaked just above the bandgap energy (because injected electrons and holes mostly gather at the band edges) and in case of a nondegenerate semiconductor decays towards higher energies following the tail of the Boltzmann distribution function. As the injected carrier density is being increased to reach higher excitation level of the material, spontaneous emission rate also increases inevitably. This process is important and needs to be considered because for each photon emitted spontaneously a new carrier needs to be injected into the active region. In case of devices based on wide bandgap materials this mechanism of carrier recombination represents the largest contribution to the total amount of current that needs to be injected in order to reach a desired level of material excitation. Analysis of total spontaneous recombination rate that takes into account components from all possible optical modes allows one to determine the radiative part of the injected current.

Thus stimulated emission becomes the major recombination mechanism supplying photons into the lasing mode. However, the spontaneous emission cannot be completely ignored. Although it is a source of a relatively small number of photons compared to the overall amount of stimulated emission photons (β_{sp} equals 10^{-4} - 10^{-5} depending on a material system and active region volume), their population is large enough to be responsible for deterioration of a complete coherence in a laser, inducing *relative intensity noise* - an important parameter in all data storage applications.

2.3.2 Stimulated Emission

There are two mechanisms of the stimulated recombination that have to be considered jointly: stimulated absorption and emission. Photons with given energy $h\nu$ induce upward and downward transitions only between those electronic state pairs which converse both: energy (E_2 - E_1 = E_{21}) and momentum ($\mathbf{k}_1 = \mathbf{k}_2$) implying that direct transitions in $E-k$ space are preferred.

Both mechanisms compete with each other since one of them generates photons into a given mode while the other takes them away. These processes occur only between filled initial and empty final states which are taken into consideration through Fermi distribution functions f_1 and f_2. The transitions are described by the rates of stimulated absorption (R_{12}) and emission (R_{21}) per unit time per unit active volume ($s^{-1}m^{-3}$), respectively. Thus it is the most convenient to introduce *net stimulated recombination rate*:

$$R_{st} = R_{21} - R_{12} = R_r(f_2 - f_1), \tag{2.3.3}$$

where R_r represents the total radiative rate that would exist if all state pairs were available to participate in a transition at a given energy. R_r gives the number of transitions per unit active volume occurring in a unit time interval as described by *Fermi's Golden Rule* for semiconductor:

$$R_r = \frac{2\pi}{\hbar}|H'_{21}|^2\rho_r(E_{21}) \tag{2.3.4}$$

R_r is proportional to the density of allowed transition pairs existing at transition energy of interest given by the *reduced density of states* ρ_r. R_r depends mainly on the spatial overlap of initial (Ψ_1) and final (Ψ_2) electronic wavefunctions under the time-harmonic perturbation (H'_{21}) induced by a stimulating electromagnetic wave. Since all possible electronic states form orthogonal set of wavefunctions mainly those with an overlap integral close to unity take part in the transition. Although a perfect orthogonality is disturbed by differences in electron and hole effective masses and barrier heights in a conduction and valence bands, wavefunction overlap leads to the k-selection rule which requires that an electron in the initial and the final energetic state propagates along the same direction.

The two possible transition states must be in resonance with oscillations of incident electromagnetic wave. The strength of an interaction between them is determined by the matrix element $|H'_{21}|^2$ defined as:

$$|H'_{21}|^2 \propto | < \Psi_2 | \hat{e} \cdot \mathbf{p} | \Psi_1 > |^2 \tag{2.3.5}$$

It depends not only on the envelope wavefunctions of initial and final electronic states and their overlap but also on the polarization of incident light provided that the material has a preferred axis of symmetry. Particular symmetries of the conduction and valence band Bloch functions in quantum well lasers cause that the interaction between conduction and heavy-hole states is much stronger for electric fields polarized in the plane of the well than in the direction perpendicular to it. As a result about 90% of stimulated emission in nitride-based LDs is coupled into the TE mode polarized in the junction plane [21].

2.4 Material gain

When a material is excited by an external source injecting excess carrier population, the balance between stimulated absorption and emission changes. At some level of injection emission processes prevail over absorption. As a result *material gain* appears which is reflected in the onset of optical amplification. The photon density propagating along some direction in a material is subject to the proportional growth in population over a given distance.

Considering the stimulated emission and absorption rates at a given transition energy (E_{21}) one can take into account the ratio between them:

$$\frac{R_{21}}{R_{12}} = \exp[\frac{\Delta E_F - E_{21}}{kT}] \tag{2.4.1}$$

Net stimulated emission rate and consequently optical gain will become positive when separation of Fermi levels (ΔE_F) will be larger than the transition energy of interest E_{21}. Thus the following relation needs to be satisfied:

$$\Delta E_F < E_{21} < E_g, \tag{2.4.2}$$

implying that the voltage across the junction must be grater than the bandgap to achieve gain in the active region.

Using Fermi's Golden Rule material gain at a given transition energy g_{21} can be described by:

$$g_{21} = \frac{2\pi}{\hbar} \frac{|H'_{21}|^2}{v_g N_p} \rho_r(E_{21})(f_2 - f_1) \tag{2.4.3}$$

It is possible to divide the origin of the optical gain into two components. One of them reflects injection level through Fermi distribution functions (f_1 and f_2). The other is strictly material dependent and relies on:

- incident perturbation to the system Hamiltonian (H'_{21}),
- photon population in a considered mode (N_p),
- the group velocity (v_g) of electromagnetic wave.

The material-dependent component defines the maximum material gain possible when carrier population is totally inverted (f_1=0 and f_2=1). In case of nitrides the maximum value of material gain reaches about 10^4 cm^{-1}.

Usually only about 30% of a maximum material gain is necessary to obtain lasing. Selection rules arising from the symmetry and the overlap between wavefunction envelopes suggest that transitions between state pairs of the same number are preferred and yield a dominant contribution to the total gain spectrum. For quantum well lasers usually states with n=1 are of the highest importance.

The total gain at a given transition energy E_{21} is a result of contributing transitions between all possible state pairs separated by this energy. It occurs only under population inversion conditions which require that $f_2 > f_1$. Exact positions of quasi-Fermi levels for conduction and valence bands does not play a significant role. What really matters is the magnitude of their separation.

2.5 Radiative recombination mechanisms in nitrides

A commonly used active region of nitride-based emitters consist of quantum wells and barriers based on Ga-rich $In_xGa_{1-x}N$ alloy with indium concentrations ranging mainly between x=0.02 and x=0.2 depending on the desired emission energy and carrier confinement. Because of the lack of a lattice-matched substrate the early devices suffered from extremely large threading dislocation densities ranging from 10^9 cm^{-2} to 10^{10} cm^{-2} [22, 23]. Nowadays they are reduced down to 10^5 - 10^6 cm^{-2} because of the usage of overgrowth [24] and high pressure growth [25] techniques. What would definitely hinder an effective radiative emission in AlGaAs- and AlInGaP-based devices turned out not to be as much critical for a new material system. Radiative efficiency of InGaN emitters shows superiority over other III-V semiconductor compounds. In order to explain insensitivity of radiative recombination processes to structural defects of the material different phenomena have been proposed. The most widely accepted one concerns In inhomogeneities as a major carrier localization effect [23]. Its origin is attributed to the low miscibility of In in GaN resulting in clustering of In which causes difficulties in obtaining homogenous Ga-rich InGaN layers [26]. Spatial fluctuations of the In content lead to band profile inhomogeneities that induce carrier confinement and isolation from nonradiative recombination centers. The strength of this effect is reflected in magnitude of photoluminescence and carrier decay times which are only slightly influenced by changes in a threading dislocation density [27]. The same effect has been argued to be caused by potential changes because of well thickness variations or by band bending at V-shaped defects [28].

Deviations from designed QW thickness and In content increase additionally the density of available states which give rise to *inhomogeneous broadening* of a gain curve through appearance of band-tail states. With elevated carrier injection the band-tail states together with the lowest conduction band states become populated. Additionally, screening of internal electric fields takes place. As a combined effect of these two phenomena a blueshift in the emission energy appears. On the other hand Coulomb effects redshift the emission energy mostly due to bandgap renormalization with a smaller impact of dephasing and screening [29]. The spectral shift of the resulting gain curves is a net effect of these processes and will be subject to the analysis in the next chapters.

Intensified experimental work devoted to identification of the major radiative recombination processes has been carried out so far. Because of the lack of heavy doping within quantum wells the main radiative processes involved in the generation of light are band-to-band transitions. Their specific features are governed by the excitation level. It is commonly agreed that the origin of spontaneous emission comes from recombination of excitons localized at bandedge potential minima [23] introduced by In clustering. Compositional imperfections induce fluctuation of excitonic transition energy. They are reported to remain in the range between 30 meV [30] and 250 meV [31] in different samples which is considerably larger than 10 meV expected for a simple random alloy [32]. As a result the exciton transition energy observed even at room temperature can occur below the lowest n=1 quantized level [31]. Although excitonic behavior has been theoretically predicted to disappear at elevated injection levels [33, 34] and the lasing action should originate from recombination of electron-hole plasma [35], it is difficult to verify this fact experimentally. The combined effects of bandfilling, screening of strong spontaneous and piezoelectric fields and Coulomb interactions together with the band-gap renormalization form a complex set of phenomena that define the optical characteristics of InGaN-based quantum wells. They cannot be analyzed separately. Considered together they effectively mask the origin of stimulated emission in nitrides. Despite the initial attribution of lasing to recombination of deeply localized [36] or free excitons [37], the latest results based on the detailed analysis of the spontaneous electroluminescence spectra tend to assume that exciton pairs become unstable at threshold [38]. The 60 meV exciton binding energy predicted for low carrier density in quantum well [39] becomes considerably reduced while approaching lasing due to bandfilling and screening effects. Thus the assumption suggesting that the free electron-hole plasma yields the major contribution to lasing confirms the early reports made by Nakamura *et al.* [40]. However, it is still not clear whether the optical properties of nitride devices should be explained on grounds of quantum well physics or rather by gain models assuming the formation of quantum-dot-like structures [41].

2.6 Optical modes of a resonant cavity

Optical energy of a diode laser is stored in a standing electromagnetic wave of a resonant cavity. The resonant mode, originating from radiative recombination within InGaN quantum wells, is guided by a GaN-based waveguide and $Al_{0.16}Ga_{0.84}N/GaN$ strained layer supperlattice cladding. These layers account for transverse (across the epitaxial layers) optical confinement. Lateral confinement (parallel to the junction plane) is induced by shallow etching (down to the middle of a p-type waveguide) to form a mesa stripe (see Figure 2.2).

Electrically insulating layer of SiO_2 deposited on both sides of the mesa stripe limits the carrier injection only to this region, reduces current spreading and defines the axis and the width of a resonant cavity. Since a charge flow is limited only to a narrow stripe region, so called *gain guiding* appears. Although a gain guided mode has a diverging wavefront [42], a spatial variation in a distribution of injected carriers induces a constant mode width in a lateral direction. Increased losses beyond the border between electrically excited and unexcited regions keep a semiconductor material below the optical transparency level. Spatially varying distribution of injected carriers defines a gain stripe below the p-type contact electrode along which a guided mode can be sustained. The effect of a lateral confinement is additionally strengthened by the mesa stripe inducing a weak *index guiding*, which makes use of a difference between refractive indices of a GaN waveguide and surrounding SiO_2 layer.

The analysis originating from Maxwell's theory leads to the derivation of time- and space-dependent wave equation:

$$\nabla^2 E = \mu\varepsilon \frac{\partial^2 E}{\partial t^2} \tag{2.6.1}$$

In case of a semiconductor laser, this relation can be satisfied by time-harmonic field propagating in a dielectric waveguide along the resonator direction oriented parallel to z-axis:

$$E(x, y, z, t) = \widehat{\mathbf{e}}_i \, E_0 \, U(x, y) \, e^{i(\omega t - \widetilde{\beta} z)} \tag{2.6.2}$$

The unit vector $\widehat{\mathbf{e}}_i$ defines either TE or TM polarization, E_0 gives the wave amplitude in units of volts and U(x,y) describes the scalar normalized electric field profile in the plane perpendicular to the propagation direction. Optical gain and internal propagation loss are taken into account through the complex propagation constant $\widetilde{\beta}$.

Once equation 2.6.2 is plugged into 2.6.1, it straightforwardly appears, that the electric field distribution U(x,y) must satisfy a time-independent relation:

$$\nabla^2 U(x, y) + [\,\widetilde{n}^{\,2} k_0^2 - \widetilde{\beta}^{\,2}\,]\, U(x, y) = 0 \tag{2.6.3}$$

where k_0 and $\widetilde{n}$ stand for the free-space wave vector and the effective refractive index of a given mode, respectively. All modes are unique solutions of Maxwell's equations, satisfying constrains imposed by continuity conditions of the tangential fields at the boundaries. Thus U(x,y) describes the distribution of the intensity profile of a standing electromagnetic wave in a laser cavity. In every practical case the transverse field profile of a guided mode of interest has a maximum at the active region and takes the form of evanescent waves as the distance from the quantum wells increases (Figure 2.1).

In order to account for the reduction in gain induced by the spreading of the mode away from the active region, optical confinement factor needs to be defined as a spatial overlap of the volume occupied by injected carriers (i.e. quantum wells, where the actual optical amplification takes place) to the entire volume containing the electromagnetic wave. Since the photon field of edge emitting lasers almost totally fills the resonator along its axis, the integration in this direction can be omitted as it yields a unity and the optical confinement consists in the first approximation of transverse and lateral component. Thus a three-dimensional relation reduces to:

$$\Gamma = \frac{\int_0^{w_x} \int_0^{w_y} |U(x,y)|^{\,2}\, dx\, dy}{\int_{-\infty}^{+\infty} \int_{-\infty}^{+\infty} |U(x,y)|^{\,2}\, dx\, dy} \tag{2.6.4}$$

The differences of refractive index values between the subsequent components of a multi-layered dielectric waveguide are in a range of 1 percent. They account for a relatively weak waveguiding and significant mode spreading. The optical confinement typically remains not larger than a few percent. This relatively low value is enough to reach lasing for a reasonable range of injection currents. However, care needs to be taken in order to get a detailed insight into the optical properties of the waveguide.

2.7 Threshold for lasing action

Lasing action for a given mode can be reached only when both mirror loss α_m as well as internal propagation loss $< \alpha_i >$ are compensated. This means that at threshold the electric field E described by Equation 2.6.2 should replicate itself after one round-trip within the cavity. Practically this condition requires that E(0)=E(2L), defining the threshold relation between material gain g_{mat}, optical confinement Γ, resonator length L and mirror reflectivity coefficients r_1 and r_2.

$$\Gamma\, g_{mat}^{\,th} = < \alpha_i > + \frac{1}{L}\, ln \frac{1}{r_1 r_2} \tag{2.7.1}$$

If the injection current is increased above its threshold value, carrier density N and material gain g_{mat} (related to N monotonically) increase temporarily as well. The amount of the net stimulated recombination rate R_{st} also increases instantly reducing finally the above-threshold carrier concentration and the material gain down to their threshold values. All excess carriers are consumed by the stimulated emission and corresponding recombination energy appears as increased optical power at laser output. As a result gain and carrier density clamp at their threshold values with oscillating changes in the range of nanoseconds. If it were not for the fact that the material gain stays constant for any given current above threshold, the optical power within the resonator would increase without bounds. The principle of energy conservation would be violated.

2.8 Laser characteristics above threshold

Once the carrier injection reaches the threshold level, a coherent electromagnetic wave emerges out of the resonant cavity evidencing the dominant onset of the stimulated emission. In order to establish the lasing action in continuous wave regime, input electrical power at threshold should be minimized. Reduced device heating and degradation can be achieved by maximizing the injection efficiency. Ideally, the entire injected carrier population should recombine in the active region and convert into photons. In a real device carriers are subject to the current leakage out of the active region followed by recombination events (either radiative or nonradiative) that does not contribute to the cavity mode.

Although theoretically carrier concentration and material gain should remain pinned to their threshold values, inhomogeneities in carrier injection and internal loss distribution observed in real devices introduce non-uniformities of threshold conditions throughout the entire active region. Thus the number of carriers that recombine within the active region is not equal to the total number of carriers injected into the device. The fraction of the above-threshold current that results in stimulated emission is usually defined as the *internal quantum efficiency* η_i.

To assure the maximum possible carrier injection level modern diode laser have evolved to heterostructure devices consisting of adjacent epitaxial layers formed by compounds of similar lattice constant and crystal symmetry but having different bandgaps. An alloy with the lowest bandgap is used within a depletion region of a diode to form a quantum-well-based active region which confines injected electrons and holes, increases carrier concentration and improves radiative recombination rates leading to enhanced optical gain and reduced carrier losses. As a result lower operating current densities can be achieved this way.

As it can be derived from the carrier- and photon-rate equations [43] the relation between output power P_{out} versus driving current I above threshold I_{th} (so called L-I characteristic) can be enclosed in the equation taking into account injection and radiative efficiencies, internal propagation and mirror loss and emission energy hν.

$$P_{out} = \eta_i \left(\frac{\alpha_m}{< \alpha_i > + \alpha_m}\right)\frac{h\nu}{q}(I - I_{th}) \tag{2.8.1}$$

A typical light-current and voltage-current curves and the emission spectra of a CW-operated laser device are depicted in Figure 2.3(a) and (b), respectively. The device was stabilized at 18°C by a thermoelectric cooler.

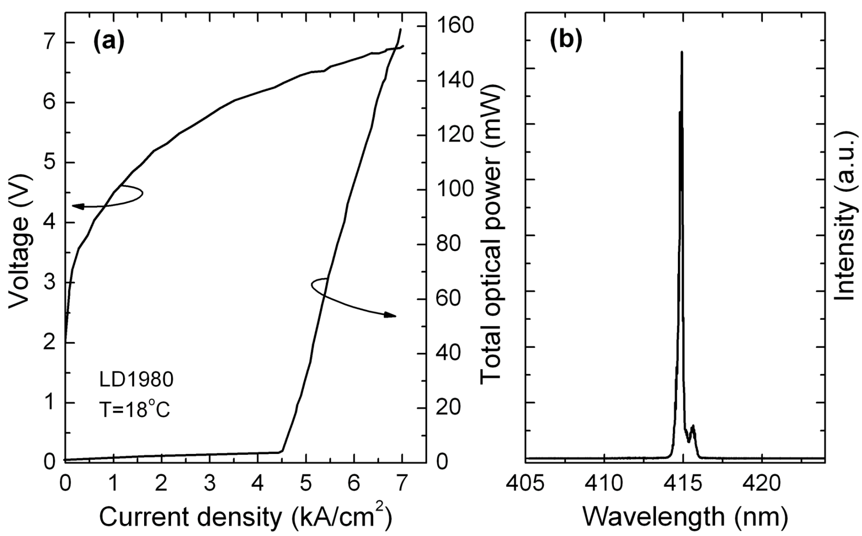

Figure 2.3: Typical light-current and voltage-current curves (a) and the emission spectra (b) of a CW-operated LD.

The output power above threshold is a linear function of current. Ideally, if all of the carriers recombined radiatively in quantum wells and all internal propagation losses were eliminated, the L-I slope would reach about 3 W/A for the emission energy of GaN-based device close to 400 nm. The linearity of the laser output can be however broken when spatial inhomogeneities in carrier and temperature distribution induce changes in effective index of refraction forcing the switch between the resonator modes reflected by the appearance of kink in the L-I curve. What is even more important, if the excess heat generated by the current flow cannot be efficiently dissipated by the cooling system, thermal roll-over appears. At high temperature the potential barriers in the active region do not confine carriers efficiently any more and thermal energy allows them to escape out of the quantum wells. The deterioration in the output power appears.

2.9 Near-field and far-field patterns

In an ideal situation of a uniform and real-index waveguide, the guided electromagnetic wave propagating along the resonator axis has a form of a planar wave-front (Equation 2.6.2) with a field distribution $U(x, y)$ on a laser facet. As the wave emerges out of the cavity, it diffracts into the air, where it is usually captured by the external optics after traveling some distance. Diffraction theory refers to a planar field on a laser facet as a *near field*. Near field waves are approximately planar, but gradually start to exhibit a considerable curvature. Some critical distance away from the facet, usually about $\frac{w^2}{\lambda}$, where w is the spatial dimension of a source emitting radiation of a given wavelength λ, planar waves diffract completely and transform into field of a spherical geometry referred-to as a *far field*.

According to an approach introduced originally by Huygen, each area element at the emitting facet is a source of a spherical 'wavelet', which propagates into the air and contributes to the overall diffraction pattern. The field is a superposition of periodic functions of different periods and orientations. It can be expanded into propagating and evanescent waves [44]. The amount of the evanescent waves depend on the amount of details in the field distribution U(x,y), that are smaller than the incident wavelength. The on-axis wave vector component of any given evanescent wave is imaginary. For this reason such waves propagate mainly in x-y plane and they are absent in the far-field picture. The smaller the detail, the greater weight of the evanescent distribution in the on-axis direction. Consequently, the fine peculiarities of the on-facet field distribution are unresolvable from the distance larger than a few nanometers. They are, however, critically important in a process of optimizing the properties of the waveguide, as they give a picture of a guided mode shape and its evolution in time. Figure 2.4 depicts example near-field and far-field intensity profiles collected by a near-field optical microscope. Details of such an analysis will be given in Chapter 8. Once the spatial near-field distribution U(x,y) is known, the angular far-field intensity profile can

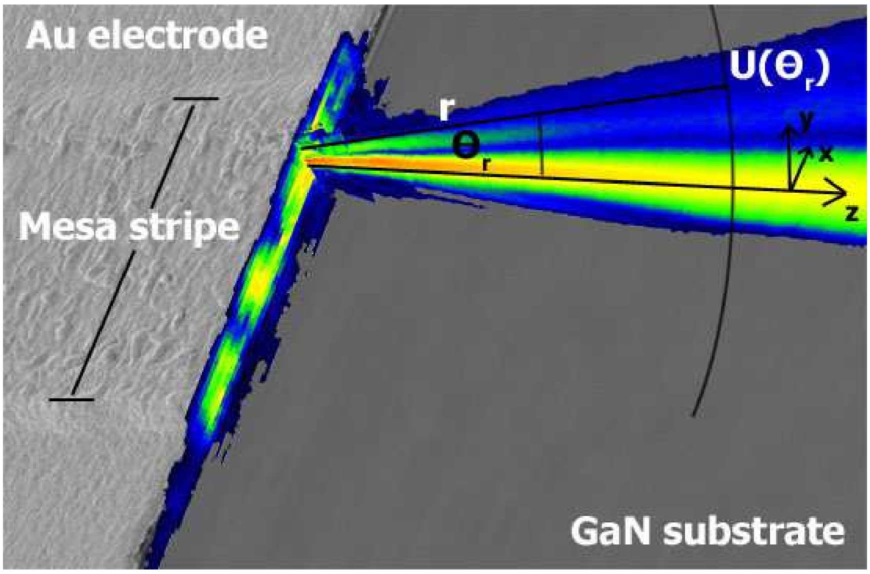

Figure 2.4: Examples of near-field pattern and transverse far-field profile collected by near-field optical microscope overlayed on an SEM image of a laser facet.

be deduced using the designations made in Figure 2.4 [43]:

$$U_F(\theta_r) = \int\int U(x,y)\frac{e^{-ikr}}{r}[\frac{i}{\lambda}cos\theta_r]dxdy \quad (2.9.1)$$

In case of in-plane edge-emitting lasers dimensions of the waveguide in transverse direction are much smaller than the ridge width of the mesa stripe. As a result the angular spread of the far field in lateral and transverse directions is considerably asymmetric approaching 9° and 25° off the resonator axis, respectively [45]. Although the angular intensity spectrum follows the elliptical distribution, Equation 2.9.1 indicates, that the emitted beam does not loose its spherical symmetry as it propagates in space.

The most important practical applications require stability and uniformity of the guided electromagnetic wave. Chapter 8 will present the results of the analysis regarding the spacial and temporal behavior of resonant cavity modes, which was carried out by means of a time-resolved scanning near-field optical microscopy. A detailed analysis of the waveguiding properties of the laser structure as well as the evolution of the near-field into the far-field constitute a powerful tool capable of examining the efficiency of a given laser design, as it will be presented later on.

Chapter 3

Challenges of the nitride-based laser technology

Although semiconductor laser technology has been developed for a few decades by now employing a wide variety of materials, the knowledge concerning the processes, which determine the features of III-nitrides, is far from the complete understating due to unique properties of this material system. The difficulties to overcome in case of the nitride-based LDs relate to physical phenomena that deteriorate the device's performance and impose some serious technological drawbacks that are absent for their arsenide- and phosphide-based counterparts.

3.1 Crystal quality

Rapid development of blue light emitting optoelectronic devices based on GaN and its compounds was possible due to tremendous progress in metal-organic vapor phase epitaxy (MOVPE) improved in order to meet the requirements of nitride-related alloys. Although the initial efforts concentrated on the epitaxial growth on sapphire [14] as the most easily obtainable and cost-saving substrate, considerable lattice mismatch between the substrate and all epitaxial layers triggers the creation of high density of crystal defects (mainly threading dislocations) with densities approaching 10^8-10^{10}cm^{-2} [46] that release most of the accumulated strain. Efficient luminescence can be achieved from InGaN QWs despite extremely large (more than five orders of magnitude) concentration of non-radiative recombination sites [2] when compared to other compound semiconductor devices. The surprisingly low impact of threading dislocations is not fully understood yet. Responsibility for this fact is often attributed to In composition fluctuations [36] or potential barriers surrounding each V-shaped fault [28] that confine carriers keeping them away from non-radiative recombination centers. The band-edge potential fluctuations can act as efficient traps for LEDs under low excitation. However high power LDs operate under much more elevated carrier injection levels. Potential minima induced by indium clustering are too shallow to confine all the carriers. They fill rapidly and deteriorate the efficiency of LEDs as well as LDs, being much more crucial in case of the latter. Generally speaking, GaN-based devices are very sensitive to the structural quality of the material and suffer from high crystal defects. High quality epitaxial growth is impeded this way. Additionally, at the current stage of the development, mean time to failure of GaN-based LDs is mainly determined by the density of dislocations. Thus to obtain prolonged device's lifetimes reaching even 100 000 h, the density of dislocations needs be reduced down to 10^6cm^{-2} or even lower (10^4cm^{-2}) [47].

3.2 Operating voltage and charge transport

The issue of reducing the operating voltage is one of the crucial points in a device optimization. This goal can be partially achieved by finding the proper contacts to p-type GaN with a low ohmic resistance [48], which is however very difficult to accomplish. Responsible for this fact is the lack of a metal with an appropriately corresponding work function. As a result, a commonly used p-type Ti/Au or Pd/Au electrodes have usually Schottky barrier at the metal/semiconductor interface inducing a considerable voltage drop.

On the other hand, the enhanced p-type doping can help reduce the voltage drop across the epitaxial layers. However, there are significant problems in obtaining high-quality p-type nitride-based compounds. Mg was found to be the most efficient acceptor dopant. The obstacles originate in self-compensation and the deep nature of the Mg acceptor and its large activation energy in GaN (ranging between 150 meV and 250 meV [49]), which is assumed to increase by 3 meV per % of Al in AlGaN [50] while Si donor activation energy is only about 20 meV [51]. Low percentage of acceptor ionization (about 1% at 300 K [52]) result in the need of high doping densities reaching $10^{20}cm^{-3}$ in order to achieve free hole concentration of about 10^{18}. Such a heavy doping density diminishes the hole mobility, setting it as low as $10cm^2V^{-1}s^{-1}$, which in turn deteriorates the positive charge transport across the epitaxial layers. In order to increase the average hole concentration and to reduce the series resistance of the p-type cladding, the use of a modulation-doped GaN/AlGaN superlattices was proposed [53]. This technique has been still under development in terms of a precise epitaxial deposition and doping profile.

On the contrary, the electron mobility is as high as 2000 $cm^2V^{-1}s^{-1}$. As a consequence, there is a strong tendency for the electron overflow into the p-type layers followed by an unintentional radiative and nonradiative recombination away from the active region unless an additional electron-blocking layer (EBL) is utilized. Unfortunately, the EBL deposited in the vicinity of QWs on the side of p-type layers forms a potential barrier not only for electrons but also obstructs the hole injection. The combined impact of EBL together with the presence of potential barriers between subsequent QWs causes inhomogeneous hole distribution within the active region leading to the enhanced absorption and limiting the optical gain in some part of it. Thus a role of EBL, its impact on carrier injection and recombination mechanisms, the optimum structural design and doping still need to be unveiled.

3.3 Spontaneous and piezoelectric polarization

Unlike the other III-V semiconductors like GaAs or InP, which crystallize in the zinc blende structure, GaN and its alloys are grown mostly in the hexagonal symmetry of wurtzite. All state-of-the-art laser devices available commercially are presently deposited along [0001] (c-axis) crystallographic direction of wurtzite-symmetry substrates. Although a zinc-blende structure can be successfully obtained experimentally through the use of cubic substrates like Si [54] or GaAs [55], its character is metastable and leads to a significantly lower crystal quality. Unfortunately, crystals grown in hexagonal symmetry are subject to strong polarization induced-electric fields along c-axis. They are negligible in other III-V compounds crystallizing a zinc blende structure due to the high symmetry of the crystal along [001] nonpolar axis, which defines a growth direction for these materials. In case of the nitrides, the electric fields cannot be ignored.

There are two phenomena inducing material polarization in the wurtzite-symmetry nitrides. The first one originates from an intrinsic asymmetry of the bonding in the equilibrium crystal structure. Lower symmetry of the wurtzite induces a net displacement of the negative charge towards nitrogen along [0001] direction [56] leading to the formation of *spontaneous polarization.*

The other component of the internal electric field is induced by a mechanical stress and originates in a lattice mismatch between a GaN substrate and InGaN-based QWs. As a result of this mismatch, QWs in the active region are subject to compressive biaxial strain induced in a junction plane. In order to retain the volume of a unit cell, additional distortion along c-axis appears leading to *piezoelectric polarization.* Piezoelectric constants are an order of magnitude higher in GaN that in GaAs.

The total polarization present within a crystal is the sum of the spontaneous polarization and piezoelectric polarization. Electric field induced this way is directed towards Ga-face of a GaN substrate. However, in order to obtain the entire electric field across quantum wells sandwiched between p- and n-type layers of a laser stack, one needs not to forget about a junction electric field which is pointed in opposite direction since n-type layers are deposited on GaN substrate at first. The total amount of internal electric fields range within 1-2 MV/cm for a typical QW In content of less than 10%. This phenomena was shown originally by means of *ab-initio* calculations [57] and was then confirmed by experimental the evidence [58].

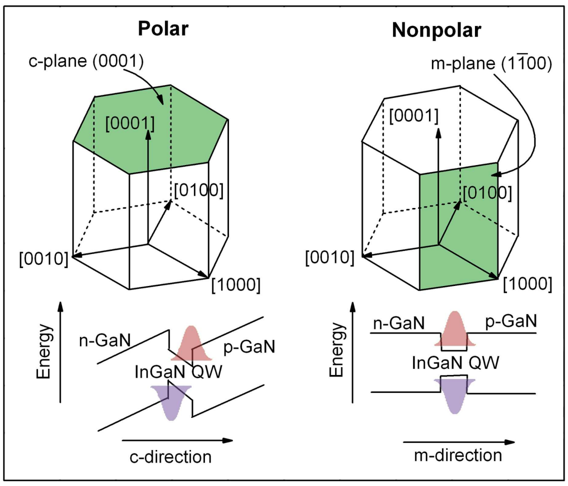

Figure 3.1: Orientation of crystal planes exposed to the epitaxial growth in polar (c-plane) and nonpolar (m-plane) direction with corresponding energy band diagrams and the position of electron and hole wavefunctions.

Polarization difference between the adjacent atomic layers implies a net spatial separation of charge. As a result a bound charge appears on each interface. This surface charge is a source of a step-like change in electric field as predicted by the *Gauss law.* The total electric field change across a certain volume of polarized material can be taken into account by summing all contributions across interfaces between atomic layers of different polarity.

Presence of the electric field induces a spatial separation of electron and hole envelope wavefunctions towards triangular potential minima at opposite interfaces of a QW (see Figure 3.1). Limited spatial overlap results in reduction of oscillator strength which in turn deteriorates radiative recombination rate and consequently optical gain which retards device's performance [59]. It is commonly agreed that internal fields in quantum wells can be efficiently screened either by heavy barrier doping with Si donors (as high as 10^{19} cm^{-3}) or by high carrier injection [60]. Although both conditions are satisfied in case of laser diodes, the QW thickness is usually kept within an effective Bohr radius $a^*{}_B$, which remains in the range of a few nanometers and prevents the reduction of a spatial wavefunction overlap.

Apart from spatial separation of charge across quantum wells, large electric fields induce band profile bending that shifts the emission towards lower energy in a current-dependent way and is often referred to as a *quantum confined Stark effect* [61].

The problem internal electric fields becomes more pronounced for active regions comprising of thick InGaN QWs with a high indium content designed for an operation in a blue-green spectral range. For this reason the operation of InGaN laser devices is limited by now to wavelengths shorter than 482 nm [62].

The promising way to overcome these limitations is the epitaxial growth along crystallographic directions which reduce $(11\bar{2}2)$ [63] or even totaly eliminate internal piezoelectric fields ($(1\bar{1}00)$ m-plane [64] or ($(11\bar{2}0)$ a-plane [65]). There are, however, some serious challenges that need to be dealt with:

- availability of large-area, low-cost nonpolar and semipolar GaN substrates
- elimination of nonradiative recombination cites
- efficient doping technology taking into account its dependance on the crystal orientation and the growth surface

- reliability and lifetime of devices grown on different crystal orientations

3.4 Thermal properties

The combined impact of a large bandgap energy, high resistivity of p-type layers and p-type contact electrode together with a high density of electronic states require applying high voltage and high injection current in order to achieve the population inversion. Significant amount of the electrical power applied to the device's terminals is responsible for the pronounced heat generation. If the thermal stability of a given laser diode is not sufficient, self-heating limits considerably its performance. Although the thermal conductivity of GaN (typically in the range between 130 $Wm^{-1}K^{-1}$ and 200 $Wm^{-1}K^{-1}$ [66] are more than three times larger than that of GaAs, it is still too little to assure required heat dissipation, which at threshold can be even twenty times larger for nitride-based devices. Excess heat triggers the carrier escape from the active region. As a result, special design considerations and different laser mounting schemes need to be taken into account in order to achieve CW operation within a reasonable range of driving currents. Once this aspect is considered, it is possible to limit the degradation rate and fabricate more reliable laser devices.

3.5 Guiding of the optical mode

Optical confinement of the guided mode and the total internal propagation loss are important parameters characterizing a resonant cavity. They cannot be omitted as the former defines the lasing threshold and the latter influences the external quantum efficiency. Thus the optimized structure of the optical waveguide providing the best overlap of the cavity mode with the active region as well as the lowest possible propagation loss is a crucial task for finding the optimum design for a laser device.

The above-mentioned difficulties, often remaining unresolved in case of III-nitride laser technology, make the modern devices still far from the optimum. Most of these aspects will be addressed to in the next chapters, familiarizing the Reader with the major issues introduced and conclusions drew throughout this work.

Chapter 4

Laser structures under investigation

The laser structures studied in the following dissertation were deposited epitaxially on the bulk GaN crystals supplied by the Crystallization Laboratory of the Institute of High Pressure Physics, Polish Academy of Sciences. Depending on an intended measurement method, the samples were either in the form of unprocessed epitaxial layers deposited on a bulk GaN crystal or operation-ready optoelectronic devices.

4.1 High pressure growth technology of bulk GaN substrates

In order to achieve the best growth results in terms of the surface morphology and the crystal structure, the undisturbed step-flow growth mode is necessary. Threading dislocations disturb the optimum growth mode leading to a complicated and chaotic step structure. Much effort has been undertaken in order to reduce the dislocation density in laser structures by introducing the substrate different from sapphire. Although blue LDs were demonstrated successfully on SiC [67] and spinal $MgAl_2O_4$ [68] substrates, no significant technological progress was achieved. GaN remains the best possible material candidate for bulk substrate used for epitaxial growth due to its almost perfect matching in terms of a lattice constant and thermal expansion which promote homoepitaxy with respect to heteroepitaxy.

The high-pressure- and high-temperature-growth of GaN from the nitrogen solution in liquid gallium [25] is the major technique developed at Institute of High Pressure Physics in order to supply high quality bulk GaN crystals. The growth synthesis requires the presence of relevant reactants in three phases: nitrogen gas particles (N_2), liquid gallium and semiconductor GaN solid. The atoms in all three phases are strongly bonded. The dissociation energy of diatomic nitrogen is as high as 9.76 eV [69], making it an extremely stable molecule. Additionally, strong bonding of GaN atoms (9.12 eV per atomic pair) result in unusually high solid GaN melting temperature of about 2200°C. These features require that the crystal growth takes place under the pressure of 1.5 GPa and temperature of about 1500°C. In such conditions nitrogen particles dissociate at a hot surface of liquid gallium, dissolve and are transported into the colder part of a crucible by diffusion and convection where the spontaneous nucleation process takes place. The growth synthesis is initiated by heterogenous crystallization of GaN on gallium surface. Through the formation of dominant growth centers the entire process ends up at the bottom of the crucible in a mode where the growth of a small number of single crystals appears in the supersaturated solution of N in liquid Ga.

The 300-hour-long growth process, which takes place at very slow rate of about 0.1 mm/hour, is strongly anisotropic. It occurs about 100 times faster in $[10\bar{1}0]$ direction perpendicular to c-axis [70]. As a result the crystals are wurtzite symmetry [0001] face (c-plane) hexagonal platelets with mirror-like flat and transparent surfaces. Hexagonal shape posses the lowest surface energy for this crystal orientation. GaN substrates obtained this way have perfect morphology suggesting stable layer-by-layer growth. However the supersaturation conditions need to be precisely controlled as they are crucial for the growth of large GaN crystals. Proper growth temperature and its gradient across the crucible together with relevant mass transport conditions assure that the accelerated unstable growth at crystal edges and corners can be avoided.

Standard dimensions of the crystals obtained by high-pressure growth remain in the range of 8-12 mm having constant thickness of about 60 μm. Significant residual oxygen doping yields high free electron concentration $5 \times 10^{19}\ cm^{-2}$ which is responsible for highly conductive properties. They are beneficial from the point of view of the laser fabrication, because they enable an easy preparation of the back side n-type electrode, ensuring more uniform current flow and an easier processing.

The high pressure synthesis is capable of delivering GaN bulk crystals with threading dislocation density as low as 10^2 cm^{-2} as confirmed by the defect selective etching technique [71]. X-ray diffraction rocking curves confirm the excellent crystal quality of the material by a narrow full width at half maximum close to 30arcsec [25]. However, limited dimensions of bulk GaN crystals pose some serious difficulties that are important from technological point of view:

- The quality of epitaxial growth can be influenced by a turbulent flow of the carrier gases above a small substrate surface
- Insufficient thickness induce substrate bowing after deposition of strained epitaxial layers which impedes processing and limits its precision
- Crystal uniformity and device yield should be increased in order to commercialize the production technology

By the expected future increase of the substrate dimensions by utilization of HVPE technique and by successful elimination of threading dislocations, numerous improvements are expected to be obtained: device's efficiency, emission wavelength shift towards UV region achieved for QWs without indium, reduced dislocation-related strain and increased level of Mg doping are the most important ones to be named.

4.2 Substrate preparation procedures

Growth of epitaxial layers on dislocation-free substrates needs to be processed by surface preparation. Mechanical polishing is primarily used on both sides of crystal in order to remove the surface layer containing oxygen and other excess impurities incorporated during the final cooling stage of the high-pressure growth in nitrogen atmosphere. Formation of standard substrates with uniform thickness is of a fundamental importance for a subsequent device growth.

Because Ga- and N-terminated sides of bulk GaN crystal have different chemical properties, relevant preparation techniques need to be optimized separately. N-terminated side of GaN crystal is chemically active. Surface preparation consist of mechanical polishing and chemical etching in 1:5 water solution of KOH. The procedure leads to the creation of a perfectly flat surface without nonuniformities such as hills, valleys and defects introduced by polishing. On the other hand Ga-terminated facet remains rather chemically inert. Surface preparation employs different strategies consisting of a mechano-chemical polishing or alternatively the reactive ion etching (RIE) followed by annealing in ammonia and nitrogen atmosphere.

Considerable inertness of Ga-terminated side to chemical reactions is not profitable mainly because only this side of the crystal allows to obtain strong optical emission from QWs necessary to achieve efficient light emitting devices which have not been obtained so far on N-polarity side despite much effort directed in this field [72, 73].

4.3 MOCVD as the major growth technique

Metal organic chemical vapor deposition (MOCVD) is one of the major techniques for the fabrication of nitride-based LDs at Institute of High Pressure Physics. The epitaxial process employs a vertical-flow reactor with SiC-coated graphite susceptor heated by an inductive coil that enforces current flow defining the growth temperature. Purified (to parts-per-billion level) molecular nitrogen (N_2), hydrogen (H_2) and ammonia (NH_3) are used. Tri-methyl gallium (TMG), tri-methyl aluminum (TMA) and tri-methyl indium (TMI) serve as sources of group-III metals. Cp2Mg and SiH_4 are utilized for Mg and Si doping, respectively. The growth takes place at relatively high temperatures: 1050℃ for GaN, 800℃ for InGaN and 1090℃ for AlGaN. The rate of the process is monitored by a laser reflectometry with a fine resolution of a few angstrom, which is necessary to precisely control the width of the MQW structure.

4.4 Typical laser structure

The active region of a typical laser diode is composed of one to five $In_xGa_{1-x}N$ QWs. In composition can vary from 0.02 to 0.15 to match the desired emission wavelength chosen from the range of 380-430 nm. The thickness of QWs is usually set between 35 Åand 45 Åin order to achieve an effective carrier capture and confinement. Quantum barriers are composed of $In_{0.02}Ga_{0.98}N$:Si layers for 415-430 nm emission and InAlGaN quaternary compound in case of UV devices designed to emit around 380 nm. The typical barrier thickness remains close to 70 Å. The MQW-based active region is followed by 200Åof

$Al_{0.2}Ga_{0.8}N$:Mg electron blocking layer. The undoped 70-90 nm-thick upper GaN and n-type 100 nm-thick lower GaN films serve as waveguiding layers. They are sandwiched between 500 nm-thick n-type $Al_{0.16}Ga_{0.84x}N$/GaN:Si (110 x 24Å/24Å) and 370 nm-thick p-type $Al_{0.15}Ga_{0.85x}N$/GaN:Mg (80 x 23Å/23Å) superlattices, which serve as a bottom and upper cladding layers,respectively. They are designed to efficiently confine photons generated within active region. Also 40 nm-thick GaN layer heavily doped with Mg is finally utilized as a contact layer of a p-type electrode. Detailed schematics can be found by the reader in Appendix A.

A typical device is processed as a ridge-waveguide, oxide-isolated laser with a mesa structure etched down to about 300 nm, i.e. roughly to the middle of the upper cladding layer. The current flow is then defined by isolation of the surface by deposition of ZrO_2 or SiO_2 layer with a thickness of 100 nm. Photolithography is then used to create an opening through the isolating layer followed by evaporation of Ni/Au contacts of a typical low-current resistance of $10^{-3} - 10^{-4}$ Ωcm^2. Contacts to highly conductive n-GaN substrate consist of Ti/Al alloy. The stripe width can be set between 5 and 50 μm and the resonator length varies from 500 to 1000 μm. In order to improve mirror reflectivity, lasers facets are coated with quarter-wavelength TiO_2/SiO_2 dielectric Bragg reflectors.

4.5 Laser processing and major parameters

As revealed by selective etching techniques, threading dislocation density throughout the epitaxial layers raises from the initial number of 10^1- 10^2 cm^{-2} to the level of 5×10^4 - 5×10^5 cm^{-2}. Creation of dislocations is a result of a lattice mismatch and subsequent strain release between GaN and its ternary compounds (InAl)GaN [74]. Although the thickness of the epitaxial layers and the lattice mismatch is kept so that the magnitude of strain stays away from the critical value for which the cracking takes place [74], the strain is large enough to raise the density of dislocations. Most of them originate in highly lattice-mismatched AlGaN electron blocking and propagate through the p-type layers towards the surface without affecting the QWs. Despite a considerable increase, the number of dislocations throughout the active region is still low.

The major optimization procedure is being executed for LDs emitting around 415 nm. The emission spectra has a multimode character and an average linewidth of 0.5-1.5 nm. The best values of threshold current densities and the threshold voltage measured for this class of devices remain close to 3.2 kA/cm^2 and 5 V, respectively. A typical L-I, I-V characteristics and a typical emission spectra in CW operation are presented in Figure 2.3(a,b). The major contribution to the overall voltage drop originates in high resistance of a p-type AlGaN/GaN superlattice and a p-type contact electrode that need to be further optimized. The input electrical power at threshold is typically about 24 kW/cm^2. Taking into account that only a small fraction of applied energy is converted into useful photons, one gains a picture of the amount of heat to be dissipated by the laser's mounting system.

4.6 Plasma-assisted molecular beam epitaxy as a fabrication alternative

Although the major technological progress in the field of blue optoelectronics has been achieved by MOCVD, numerous technological drawbacks still live much space for a potential improvement. The usage of ammonia results in p-type passivation by incorporation of hydrogen atoms. High temperatures and growth rates lead to band profile fluctuations and significant interface roughness. Their influence on the device's operation has not been clearly understood yet and the question concerning advantages and disadvantages of such fluctuations remains unanswered. Having in mind all these features, which can be regarded as obstacles impeding the further development of MOCVD technology, one could pose a serious question whether molecular beam epitaxy (MBE) can become a viable alternative. As a growth technique characterized by ultra-high purity source materials, a reduced point defect density, a precise and accurate doping profile and atomically flat single layer growth, MBE claims the position on the cutting edge of the research related to III-nitride-based material systems.

The origin of the difficulties related to MBE should be traced back to thermodynamic arguments that require assurance of about half of the material's melting temperature in order to achieve optimum epitaxial deposition [75]. Unfortunately, temperatures as high as 1050-1100℃ lead to a rapid decomposition of GaN epilayers, which starts to occur at 800℃ in vacuum and increases exponentially with raising temperature. This effect can be minimized considerably by a carefully chosen flow of species consisting of active nitrogen, which is needed to promote the growth of the film. MOCVD uses the flow of ammonia with all its detrimental consequences. In case of MBE best results are achieved by the usage of ammonia-free, plasma-assisted MBE (PAMBE), in which the active nitrogen atoms are created from diatomic molecules by radio frequency plasma cell. In order to achieve high quality step flow growth mode, group-III-metal-rich conditions need to be assured [76, 77]. When a thin dynamically stable layer of Ga or In is formed on the sample surface, the significant reduction of the potential barrier (from 1.3 eV to 0.5 eV) for the lateral diffusion of nitrogen adatoms can be achieved [78]. As a result, the high-quality growth of laser structures is possible at temperatures as low as 600℃ [79] - considerably lower than expected from estimates considering GaN melting temperature.

High-pressure-grown bulk GaN substrates characterized by an extremely low threading dislocation density are also of fundamental importance. Once the step-flow growth mode is achieved in PAMBE reactor, threading dislocations mediate the spiral growth leading to formation of hillocks [80]. These morphological forms induce In fluctuations during the deposition of MQW active region. The device's performance deteriorates this way by increased density of energetic states and by the separation of electron and hole wavefunctions.

The basics of a typical laser structure grown by PAMBE remains mainly the same as those grown by MOCVD. The major differences originate from necessity of using group-III metal species to form precisely controlled dynamic layer on the surface of epitaxially deposited films. Under such conditions In atoms incorporate into all epitaxial layers as well. The difference is mostly pronounced throughout the waveguiding and electron blocking layers, which do not contain indium in case of the MOCVD growth and consist of InAlGaN quaternary alloy after the PAMBE growth as a result of utilization of indium as a surfactant. For further details the reader is referred to Appendix A.

From the point of view of an efficient operation n- and p-type doping are of crucial importance. Hall effect measurements reveal that the electron and hole concentrations are $5 \times 10^{18}\,cm^{-3}$ and $2 \times 10^{18}\,cm^{-3}$, respectively [81]. P-type doping is an important factor influencing the performance of each device based on formation of a p-n junction. Because of high activation energy of Mg acceptors in GaN and compensating influence of Ga vacancies and atomic H, only about one percent of dopants supplies holes into the valence band. In order to reach a desired carrier concentration, Mg doping levels as high as $10^{20} cm^{-3}$ need to be assured. Due to the lack of ammonia, the post-growth annealing is not necessary to activate p-type conductivity in case of PAMBE. As a result, the atomic diffusion is not observed and the smooth interfaces and sharp doping profiles are present across deposited films [82].

The major phenomenon limiting achievement of high Mg content is the polarity inversion from Ga to N which decreases abruptly the efficiency of Mg incorporation and deteriorates dramatically the crystal quality [83, 84]. Additionally, the effect of the improved quality of p-type layers induced by an order of magnitude higher hole concentration (as compared to MOCVD-grown structures) is counteracted by the increased resistivity of a contact electrode to p-type GaN. As a result, the overall operating voltage do not reveal considerable improvement.

Although the electrical properties of LDs grown by MOCVD and PAMBE remain comparable, the efficiency of InGaN QWs obtained from PAMBE reactor lags behind those grown by MOCVD. The poor quality of MQW active region can be attributed to spiral step-flow growth mode mediated by threading dislocations [80]. The extent to which the spiral morphology develops depend strongly on the growth conditions, i.e. the growth temperature and the ratio of group-III to group-V species [85].

The wavelength-dependent optical properties of the active region as well as the comparative study concerning the light amplification features of the optimized laser structures grown by MOCVD and PAMBE will be subject to an extensive study carried out by means of photoexcitation experiments in Chapter 6.

Chapter 5

Carrier injection and recombination

The goal of this chapter is to present processes that occur and govern the operation of each LD. We will try to consider the major transport and recombination mechanisms and analyze the influence they impose on an operation of real devices. Within the framework of the experimental part of this chapter we will be concerned with typical laser device parameters such as a threshold current, slope efficiency and their temperature dependance. They rely on the internal quantum efficiency and internal losses, which depend strongly on mechanisms of carrier transport.

5.1 Impact of annealing effects on a laser performance

The measured devices belong to the class of LDs characterized by threshold current densities ranging between 4 kA/cm^2 and 7 kA/cm^2. These values depend partially on a mesa stripe width, which varies from 5 μm to 50 μm influencing the contribution of the lateral current spreading effects [86]. The threshold voltage ranges from 7.5 V to 10 V and needs to be further optimized.

Figure 5.1(a,b) presents typical light-current (L-I) and current-voltage (I-V) curves of a commonly used LD design denoted as LD3460. The active region of the device consisted of five 4.5 nm thick QWs made of $In_{0.1}Ga_{0.9}N$. The mesa stripe had a width of 20 μm. The characteristics were collected at room temperature (RT) and 113℃. The device was driven in a pulse mode with a duty cycle of 0.05% (pulse width 50 ns, repetition rate

10 kHz) in order to reduce self-heating. The temperature of the device was stabilized by a thermoelectric Peltier heater.

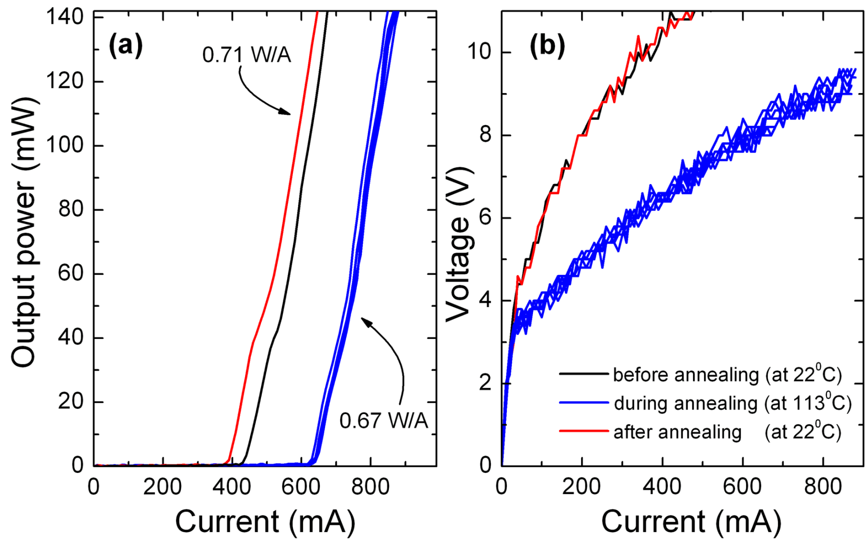

Figure 5.1: Pulsed L-I (a) and I-V (b) characteristics of LD3460 collected before (black line), during (blue line) and after (red line) current/temperature annealing.

The analysis of the data presented in Figure 5.1 indicate a few problems, that need to be dealt with. First of all, one can observe a temperature induced shift of a threshold current, which is a typical feature of all semiconductor LDs. There are however some peculiarities characteristic only for nitride-based devices such as a limited reduction of the L-I slope efficiency with rising temperature and the effects of annealing.

In order to present the combined effect of a current- and temperature-induced annealing, after the initial characterization marked in black in Figure5.1(a,b), the device was heated up to 113℃ and driven in CW regime by 20 mA current for 1 hour. The pulsed electrical characterization was performed each 10 min as designated in blue in Figure 5.1(a,b).

Although the 90℃ temperature increase is responsible for a clearly visible 200 mA shift of a threshold current, the initial L-I slope efficiency of 0.71 W/A changes to 0.67 W/A, which is a strikingly low reduction. On the other hand, the operating voltage at threshold is reduced by 20% (from 10 V at RT to 8 V at 113℃̃) despite a considerable threshold current shift. This reduction can be attributed to the enhancement in ionization of Mg acceptors induced by elevated temperature, which leads to improved properties of the p-type layers and consequently reduces their electrical resistivity.

The electrical properties of the device including operating voltage and L-I slope collected every 10 min remained unchanged during the annealing procedure as designated in blue in Figure 5.1(a,b). Thus we can rule out the influence of rapid degradation mechanisms such as diffusion of Mg or a mirror damage on a device performance.

Once the device was again cooled down to a RT, a 10% reduction in a laser threshold (from 427 mA to 383 mA) was observed as depicted in red in Figure 5.1(a). It is a feature commonly observed for many of analyzed devices. This reduction of the threshold counteracts the normal threshold current increase caused by the thermal escape and more efficient nonradiative processes. In order to understand this reduction, it is necessary to take into account the possible changes in the microstructure of the device caused by annealing under the high current in a relatively low temperature. The most intuitive approach suggests that under this type of annealing the activation of magnesium acceptors, that takes place by breaking Mg-H complexes, results in an increased number of holes reaching the active region. Figure 5.1(b) indicates however, that the reduction in laser threshold is not accompanied by a corresponding shift of the I-V curve. The possible explanation could supposedly involve the annealing, that appears predominantly in the vicinity of the active region, improving the quality of the EBL. The microstructure of the p-type cladding and the subcontact layer, which are the major sources of the total amount of a series resistance, may remain unchanged.

5.2 Sensitivity of laser threshold to temperature changes

The tendency of LD's threshold to increase under the influence of the elevated temperature within the active region is governed mainly by the reduction of the internal quantum efficiency. Every temperature increase makes the electron overflow over the active region more probable.The rate of carrier escape out of QWs is also accelerated. Significant temperature induced increase of the leakage current is mainly governed by the height of the confining barrier E_B and varies with the position of the Fermi level for the QW-confined conduction electrons E_{Fc}, as determined roughly by the factor: $exp\,[\frac{E_{Fc}-E_B}{kT}]$. The potential barrier for electrons leaking out of the active region is usually established by the 20 nm thick film of $Al_{0.2}Ga_{0.8}N$. Figure 5.2 depicts that the supposed improvement of the EBL quality, taking place after the LD's annealing as discussed above, induced the reduction of the device's threshold within the wide range of ambient temperatures.

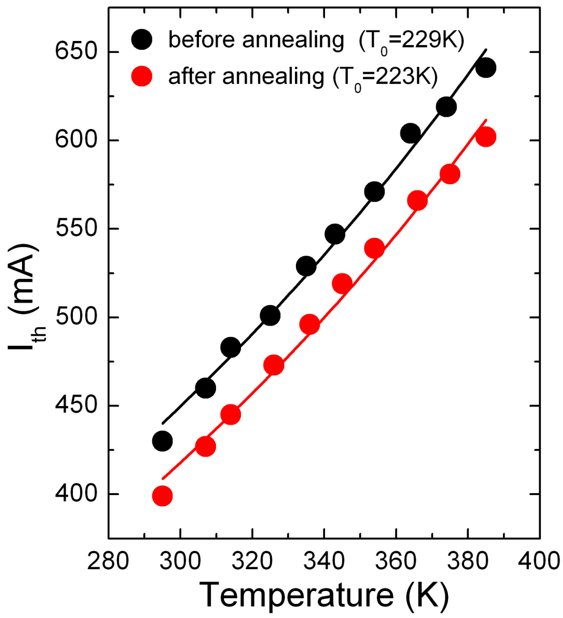

Figure 5.2: Temperature dependance of the threshold current determined for the sample LD3460 consisting of five 4.5-nm-thick $In_{0.1}Ga_{0.9}N$ QWs before and after annealing.

Data presented in Figure 5.2 concerning the thermal sensitivity of the threshold current was collected for the sample LD3460, the same as discussed above. The data was then fitted with an empirical equation:

$$I_{th} = I_0\, exp[\frac{T}{T_0}], \tag{5.2.1}$$

where T_0 is a phenomenological parameter that jointly represents all the temperature driven mechanisms that influence the LDs threshold. The higher value of T_0, the better the thermal performance of a given LD. The T_0 values of about 220 K determined before and after annealing remained roughly unchanged. Typical values of T_0 determined for the majority of nitride LDs vary between 100 K and 190 K [87, 46]. Compared to these values, the data presented above seems to be promising. However, the more commonly observed temperature stability of LDs with the active region consisting of five 4.5-nm-thick $In_{0.1}Ga_{0.9}N$ QWs can be described rather by values of T_0 parameter ranging between 120-140 K.

Despite a strong contribution from the carrier leakage, there are also other mechanisms that influence the temperature dependance of LD's threshold by modification of the device's material gain. The temperature dependance of the threshold current is fundamentally determined by the spontaneous recombination current that is required to maintain a desired peak gain necessary to compensate for all cavity loss. The temperature enhanced carrier-carrier scattering smears all energy levels inducing the homogeneous broadening of a gain curve. Close lying energetic levels can easily degenerate modifying the effective density of states and shifting the transparency condition towards higher excitation. The carrier energy in each electronic state is distributed over a wider range of adjusting energy values. Consequently, the spectral broadening of the gain curve appears. Due to accelerated scattering processes, all carriers warm up and gain energy. The occupation of states in the high energy tail of the Fermi distribution function increases. A corresponding decrease in the occupation of states lying below Fermi level appears. Since these states are the only ones that contribute to a positive optical gain, the values of the peak gain and the differential gain are considerably reduced.

In order to compensate for the reduction in a peak material gain and to restore the threshold condition, a larger carrier population needs to be injected into the active region. Consequently, an increased free carrier absorption leads to the enlargement of the internal propagation loss $< \alpha_i >$.

The carrier density N can be related to the optical gain g by a logarithmic expression:

$$g = g_0 \, ln \frac{N}{N_{tr}}, \tag{5.2.2}$$

where g_0 and N_{tr} denote the differential gain coefficient and the transparency carrier density, respectively. By recognizing the fact that the generation term at threshold within an active volume V is dominated by a bimolecular recombination proportional to coefficient B, i.e.

$$\eta_i \frac{I_{th}}{qV} \approx BN^2, \tag{5.2.3}$$

equation 5.2.2 can be transformed to express the value of the threshold current:

$$I_{th} \cong \frac{qVBN_{tr}^2}{\eta_i} \, exp[\frac{2(< \alpha_i > + \alpha_m)}{\Gamma \, g_0}] \tag{5.2.4}$$

Equation5.2.4 introduced above includes many parameters that are often unknown or not determinable unambiguously. For this reason Equation5.2.1 is much more valuable from the practical point of view as a tool to compare independently the thermal stability of different devices.

5.3 Active region design versus thermal insensitivity

5.3.1 Quantum well confinement

Although the values of T_0 presented above compare well with the corresponding parameters of red and infrared arsenide- and phosphide-based lasers [43], there are still some prospects for further improvement. Mainly because of a weak carrier confinement in narrow QWs (usually 2-5 nm thick) commonly used in nitride LDs to reduce the negative influence of piezoelectric and spontaneous polarization. Such design of the active region pushes up electronic states towards the top of the well.

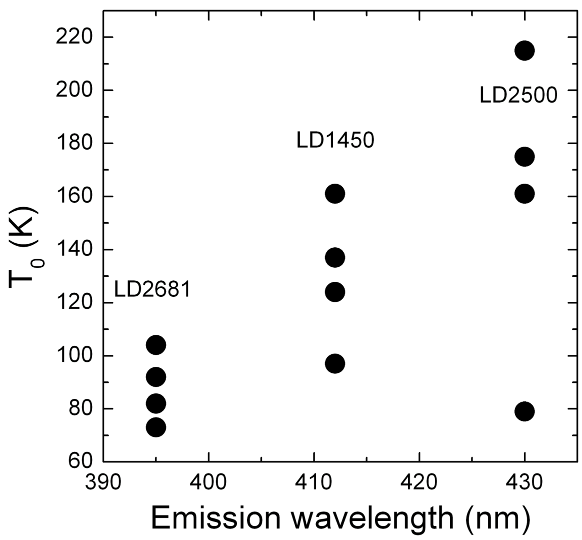

Figure 5.3: The dependance of T_0 parameter of five-QW-based LDs with different indium content.

QW band offsets can be easily enhanced by the excess addition of In. Our experience suggests, as confirmed in Figure 5.3, that the change in the QW In content from initial 8% up to 16% results not only in spectral shift of emission energy from 395 nm to 430 nm but also considerably improves T_0. It is usual to observe the evolution of the latter parameter from initial 80 K up to about 200 K when In content is changed within the range of 8-16%. Improved thermal stability is reached at the expense of increasing lattice mismatch of QWs and enhancement in the amount of the piezoelectric fields. As it was discussed in Chapter 2, due to the presence of the built-in electric field, the confined electronic states in QWs are modified in such a way that the peak material gain for a given transition energy decreases.

It was not until recently that the increasing amount of experimental evidence showed an efficient screening of the electric fields in 3 to 9-nm-thick QWs achieved by the usage of InGaN barriers highly doped (up to a level of $1 \times 10^{19}\,cm^{-3}$) with shallow Si donors [60, 88]. Internal electric fields are screened additionally by carriers injected into the LD's active region.

Commonly fabricated nitride LDs tend to rely on narrow multiple quantum well structures rather than a wider single quantum well. Contrary to common trends, the results of the earlier studies evidencing an almost total screening of the internal piezoelectric fields were treated as an encouragement to study the effect of a QW thickness on a laser performance.

In order to carry out this analysis, we choose a set of two different types of samples grown by MOCVD was chosen. Besides a typical waveguiding structure of the entire laser stack, the only difference between their internal design was the construction of the active region. From this point they will be designated as MQW LD and SQW LD. The active region of MQW LD consisted of five commonly used 5.5-nm-thick undoped $In_{0.1}Ga_{0.9}N$ QWs embedded between highly Si-doped $In_{0.02}Ga_{0.98}N$ QBs each of them having a thickness of 6.5 nm. The electron leakage into the p-type waveguide was suppressed by the growth of a 20-nm-thick $Al_{0.2}Ga_{0.8}N$ EBL. Alternatively, SQW LD was a single QW device with the active region consisting of one 9.5-nm-thick $In_{0.1}Ga_{0.9}N$ QW deposited on a highly Si-doped ($1 \times 10^{19}\mathrm{cm}^{-3}$), 10.5-nm-thick $In_{0.02}Ga_{0.98}N$ QB. The QWs were capped with 1.5 nm of the undoped GaN to avoid decomposition during a high temperature growth of the above-lying EBL. Finally both devices were processed as oxide isolated ridge LDs with a standard 500 μm long and 10 μm wide cavity. The facets were then coated with four periods of TiO_2/SiO_2 dielectric reflectors. The impact of different optical feedback and a current spreading effect on the devices' performance was limited this way. For the details of the structural design of both LDs the reader is referred to Appendix A.

The differences in QW thickness between the two analyzed laser designs was expected to reduce the electron confinement energy by at least 50 meV in favor of SQW LD. The amount of reduction is significantly large as compared to the height of a heterobarrier, which is typically between 200 meV and 250 meV. This fact should in turn correspond to the improved thermal behavior.

In an attempt to verify the temperature stability of the devices, their operation was examined in a series of temperature cycles in the range between 20℃ and 100℃. Electrical characterization was performed using a pulse current source with a 10 kHz repetition rate and 50 ns pulse duration. A low duty cycle was necessary to avoid self-heating of the device. The temperature dependance of threshold current of both LDs was determined by fitting the data with an exponential expression described by Equation 5.2.1. The obtained results are depicted in Figure 5.4. In order to validate the observations, many thermal cycles were performed. As it is nicely evidenced by the Figure 5.4(a), there was a significant

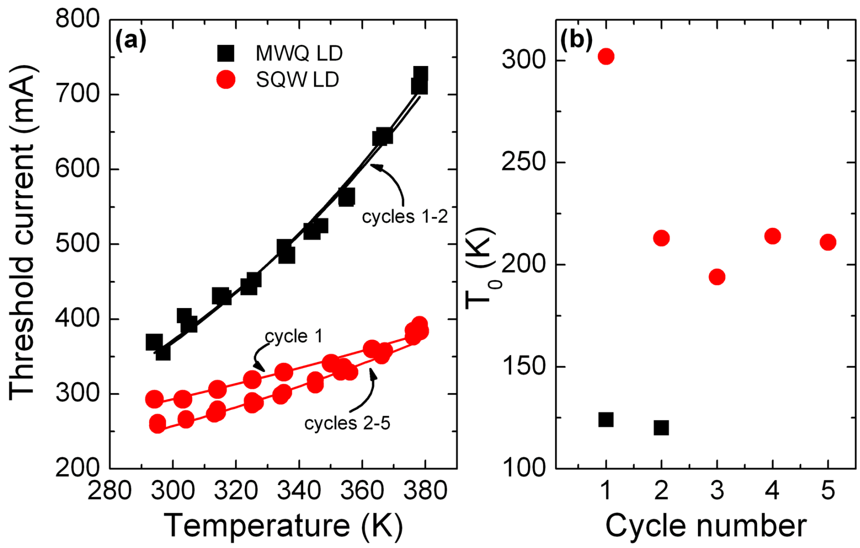

Figure 5.4: Integral of spontaneous emission spectra of a typical laser diode with an active region consisting of five quantum wells.

difference in the temperature behavior of the threshold current in favor of SQW LD. Despite the initial discrepancies in the room temperature threshold caused by the different active region volume, T_0 of about 302 K determined for SQW LD reflects superior thermal stability when compared to MQW LD characterized by T_0 as low as 120 K. However, many thermal cycles performed reveal that the initial value of T_0 determined for SQW LD during the first cycle drops down to 220 K and remains stable not undergoing any further evolution. The annealing mentioned at the beginning of this chapter seems to be completed. As evidenced by Figure 5.4(b), the latter value of T_0 is still considerably higher than the one determined for MQW LD.

The metastable character of the highest observed value of T_0, can be related to the braking of Mg-H complexes leading to the increased hole concentration in the LD's active region. A corresponding reduction of the room temperature threshold current appears. Simultaneously, the lack of any significant changes of the threshold for the highest temperatures can be observed in Figure 5.4(a) resulting in the reduction of T_0.

The activation of Mg-H complexes by an irradiation with electrons seems to be quite probable as it was already observed in a cathodoluminescence experiment leading to the first announcement of a p-type conductivity in GaN crystals [10]. It was also shown that even after the initial thermal annealing of MgH complexes, irradiation with a low energy electron beam can further improve the quality of p-type layers[89]. Current densities generated by an incident electron beam in a typical cathodoluminescence experiment (beam current 1-10 nA and beam diameter 0.5-1 μm) remain within the range of 1-10 kA/cm^2, which is a similar value compared to current densities used to excite nitride-based LDs.

It should be noted that the metastability observed in the thermal behavior of investigated device again was not reflected in the reduction of its series resistance as an indication of the structural changes that take place mainly in the vicinity of the active region.

The above-mentioned process seems to be completed during the first thermal cycle and the properties of the device do not change any more with the subsequent cycles. Consequently, the activation of the p-type layers rather than any mechanism of a rapid degradation is believed to cause an initial drop of T_0 parameter.

5.3.2 Temperature-induced enhancement of the QW carrier capture

A remarkable change in T_0 parameter from a typical 120 K for a 5.5-nm-wide QW to an astonishingly high value of about 220 K for a 9.5-nm-wide QW was not the only peculiarity that was observed during our study. A closer analysis of all L-I characteristics collected at different temperatures revealed additionally, that not only T_0 but also a slope efficiency varied in a way that is worth noticing as depicted in Figure 5.5. Let us first begin with MQW LD. The raising temperature led to a commonly observed decrease of the slope efficiency from initially collected 0.3 W/A down to 0.18 W/A. Above 70℃ the reduction accelerated dramatically. On the other hand a corresponding dependance observed for SQW LD revealed that the slope efficiency increased initially by roughly 20% up to about 60℃ contrary to the first expectations. Above this temperature a usual efficiency drop began. In the context of the above-mentioned arguments, which take into account the

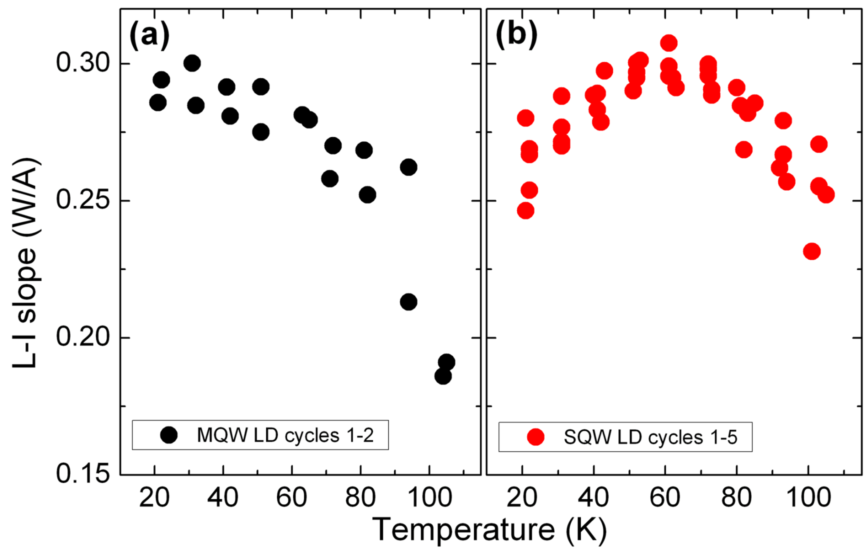

Figure 5.5: Temperature dependance of the slope efficiency of above-threshold L-I characteristics collected for: (a) MQW LD during two thermal cycles; (b) SQW LD during as many as five thermal cycles.

increased thermal stability with the rising QW width accompanied by the unusual slope behavior, one might pose a question whether an improved carrier confinement was the only factor responsible for such behavior. Such possibility is supported by some recent data concerning time-resolved photoluminescence study performed on similar structures with 9.5-nm-thick QW [88]. Those results demonstrated clearly the temperature independence of the radiative recombination time in such structures, which is a characteristic feature of light emitting zero-dimensional nano-objects [90]. However, their contribution to the lasing process is questionable, since the research carried out until now recognizes the recombination of the extended electron-hole plasma as a major source of the stimulated emission from nitride-based QWs [40, 38].

On the other hand, the anomalous temperature dependance of the slope efficiency cannot be explained neither by increased confinement nor by the Mg activation (i.e. dissociation of Mg-H complexes) due to the irreversibility of this process. However, in Mg-doped GaN a temperature rise leads to an almost three-fold increase of a hole concentration over a temperature range between 270 K and 370 K [91]. It was necessary to check if the temperature-induced increase in the hole concentration was responsible for the increase in LDs' efficiency. Numerical simulations solving drift-diffusion equations carried out for different values of a positive bias by means of the SILENSE package [92] allowed for the determination of the internal quantum efficiency calculated for the spontaneous emission at different temperatures. As presented in Figure 5.6, the calculation revealed an order of magnitude decrease of the internal efficiency in the range between 270 K and 300 K. This result excluded the thermal activation of holes as the cause of the observed anomaly.

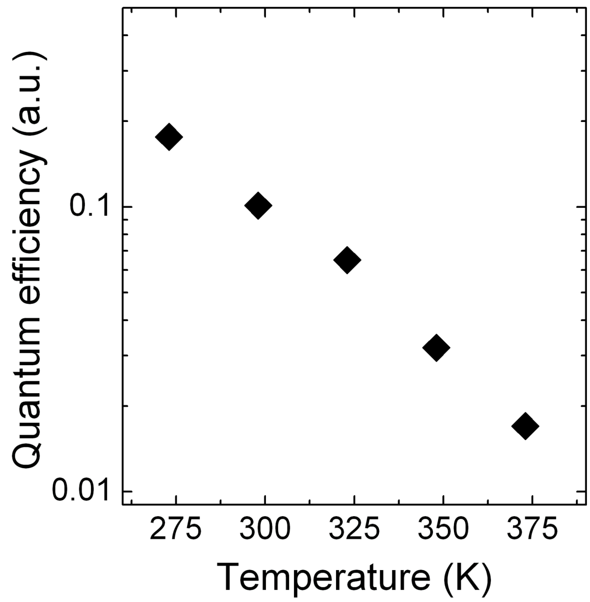

Figure 5.6: Theoretically calculated dependance of the below-threshold internal quantum efficiency on temperature of the active region.

Looking for another possible explanation, we have to find a carrier loss mechanism, that would not only reduce the internal quantum efficiency, but also would decrease with the rising temperature, providing the anomalous temperature dependance of the L-I slope efficiency. The existence of such mechanism was postulated previously, in order to explain the radiative properties of green-UV InGaN LEDs at temperatures below 300 K [93, 94, 95]. The analysis of L-I and I-V characteristics led to a suggestion that the electronic current overflow can be effectively reduced with the rising temperature once the ballistic transport of electrons through the active layer is taken into account.

In order to analyze the ballistic transport of electrons, we first need to distinguish between the two possible types of the carrier transport in QW-based LDs. The first one is the real space net transport describing carrier drift and diffusion across a positively biased separate confinement heterostructure (SCH) induced by the p-n junction electric field and tremendous carrier concentration gradients. The other type of transport involves the energy transfer regarding quantum capture and escape processes between the unconfined states (i.e. higher energy quasi three-dimensional bulk-like states) and the low energetic two-dimensional QW-confined states. These dynamic carrier transport mechanisms influence strongly the device's bandwidth and the frequency response [43]. Because of a significant impact on all high frequency laser applications, they are extensively studied in the literature taking into account a detailed balance between the carrier heating and different scattering mechanisms [96, 97, 98, 99].

Figure 5.7 presents a schematic preview of the major mechanisms governing the motion of carriers. The drift-diffusion transport is assumed to dominate in the bulk regions of the device, i.e. across waveguiding GaN-based layers and also the n-type $In_{0.02}Ga_{0.98}N$ underlying layer used in all studied laser structures as a way to increase a luminescence efficiency. The physical origin of an impact, that the latter layer imposes on the properties of QWs, has not been fully understood yet. Different explanations were proposed concerning the reduction of nonradiative recombination centers [100] or limiting the excess QW band profile fluctuations induced by the indium clustering [101] due to the modified strain distribution. Once the carriers reach the edge of the QW, they are injected into the quantum continuum states above the well. Since the mean free path of injected carriers is larger than the QW width, the probability that the injected carriers will cross the QW without being scattered cannot be neglected. Consequently, the incident carriers can either ballistically traverse the well or scatter into the bound states, where they distribute in a real space according to the envelope wavefunctions determined by Schrödinger equation. Once the carriers occur in the bound states of the QW, they either recombine or scatter back into the continuum.

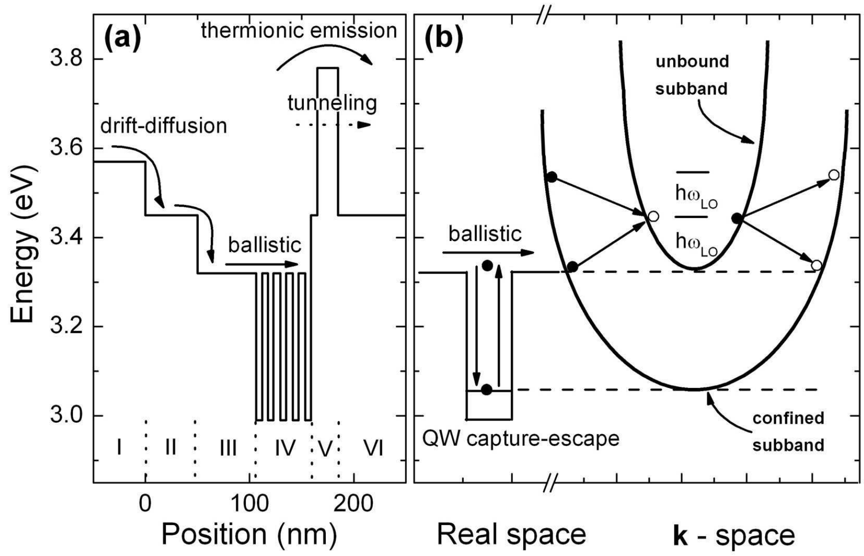

Figure 5.7: Transport mechanisms across different layers of a LD: I - n-type AlGaN/GaN cladding, II - n-type GaN waveguide, III - $In_{0.02}Ga_{0.98}N$ underlying layer, IV - $In_{0.1}Ga_{0.9}N$ QWs / $In_{0.02}Ga_{0.98}N$ QBs, V - EBL; VI - p-type GaN waveguide (a); schematic representation of scattering mechanisms governing the carrier capture-escape processes in QWs (b).

Both regions have their own quasi-Fermi levels describing the occupation probability of eigenstates characteristic for two coupled carrier populations.

The local capture and escape processes accompanied by the emission or absorption of LO phonons, as presented in Figure 5.7(b), determine the net capture current I_{net}, defined as:

$$I_{net} = I_{cap} - I_{esc} \tag{5.3.1}$$

where I_{cap} and I_{esc} stand for the capture and escape currents, respectively.

The higher temperature, the larger the occupation probability of electronic states lying at the high-energy tail of Fermi distribution function. Since the carrier scattering rate increases with carrier energy, it would be natural to expect that their mobility decreases. As a result, the mean free path of electrons is reduced and the QW carrier capture efficiency (reflected by the net carrier capture current I_{net}) raises [102]. On the other hand, QW carrier escape is strongly enhanced by the temperature elevation [98]. Above certain temperature, thermally activated QW carrier escape and a leakage current out of the active region prevails over enhanced QW carrier capture. This terminal temperature can be estimated as about

70℃ for both: MQW LD as well as SQW LD.

The apparent difference in the behavior of the L-I slope efficiency below this temperature between MQW LD and SQW LD can be attributed to differences in the QW width. Optical phonon scattering rates are reduced in QWs of lower dimensionality. Especially, if the intersubband transition energy is not in resonance with phonon energies. Because energy and momentum conservation requirements need to be satisfied, carrier thermalization rate deteriorates in QWs of lower dimensionality. A twofold increase of the QW thickness from 5 nm to 10 nm was reported to reduce the QW carrier relaxation time from 22 ps down to 17 ps for GaAs-based QWs [103]. Total time needed by an injected carrier to reach the lowest lying QW subband can be longer than the stimulated emission time. The occupation of ground energy levels of the QW is reduced leading to a hot carrier distribution. Additionally, even as injected carriers lose energy in the active region, there is an increase in QW carrier temperature, which forces carriers out of lasing states into higher energies in the well. This heating effect saturates the differential gain as it smears out the carrier population instead of raising Fermi level and is more pronounced for narrow QWs.

In the context of this argumentation we could conclude that below 70℃ QW carrier capture can be enhanced by the reduction of the mean free path of electrons. Due to improved carrier confinement and the accelerated carrier thermalization rate, this effect results in a gradual improvement of L-I slope efficiency, especially in case of SQW LD and is not as critically important in for narrow QWs of MQW LD. Thermally activated hole redistribution among neighboring QWs, which was reported to reduce differences in their excitation level as reported by Ryu et.al.[104] does not seem to be as critically important to influence the slope and threshold current in our LDs. Above 70℃ thermally activated carrier escape out of QWs followed by the leakage out of the entire active region reduces the slope efficiency significantly for both samples.

5.3.3 Dimensionality of the active region core versus temperature stability

Energy and momentum conservation requirements imply that the transition between bulk-like states in SCH region are more probable than transitions between discrete electronic levels in QWs. Therefore, the relaxation of carriers from extended into QW-confined states is inhibited [105].

If one assumes that in lasers with relatively narrow SCH region carrier capture processes dominate over the transport across confinement layers, total capture time is identical with the intrinsic carrier capture connected with the net current I_{net} flowing into the well and introduced in Equation5.3.1. In such a situation, the dynamic carrier capture and escape times can be calculated as derived from the standard carrier and photon rate equations that can be found in the literature [43]:

$$\frac{qV_{SCH}}{\tau_{cap}} = \frac{\partial I_{net}}{\partial N_u} \tag{5.3.2}$$

$$\frac{qV_{QW}}{\tau_{esc}} = \frac{\partial I_{net}}{\partial N_c} \tag{5.3.3}$$

N_u and N_c stand for the volume carrier concentrations occupying the unbound and confined states, respectively. For both processes the carrier lifetimes scale with the volume of either the confinement region or the quantum well.

Equation 5.3.2 relates the carrier concentration induced change of the net capture/escape current I_{net} with the volume of QWs (V_{QW}) and the confining region (V_{SCH}). Any increase of V_{QW} enhances the QW capture probability as expected intuitively. In order to consider the influence of V_{SCH} on a laser performance, one has to treat the injected carriers as a sum of the carrier population bound by the QWs and quasi-extended population of carriers occupying higher-lying energetic states in the core of the active region (see Figure 5.8(a)). The wavefunctions of the unbound carriers extend throughout QWs, QBs, $In_{0.02}Ga_{0.98}N$ underlying layer and the GaN cap layer. Without any external excitation these two carrier populations remain in thermal equilibrium. There is no net current flowing into or out of the QWs. Once the forward voltage is applied, Fermi level of extended carriers is shifted away from Fermi level of the QW-confined population. Any increase in V_{SCH} reduces the concentration of extended carriers lowering the position of Fermi level. Consequently I_{net} decreases as a result of the enhanced QW carrier escape. On the other hand the effective barrier height for the thermal escape of quasi-unbound carriers over EBL increases. The leakage current is reduced as it depends on the exponential factor: $exp\,[\frac{E_{Fc}-E_B}{kT}]$. Additionally, an operating device can benefit from the reduced separation among extended energetic states, that approach continuum and facilitate carrier thermalization. As depicted in Figure 5.8(b), we obtained a considerable improvement of LDs' thermal stability by increasing

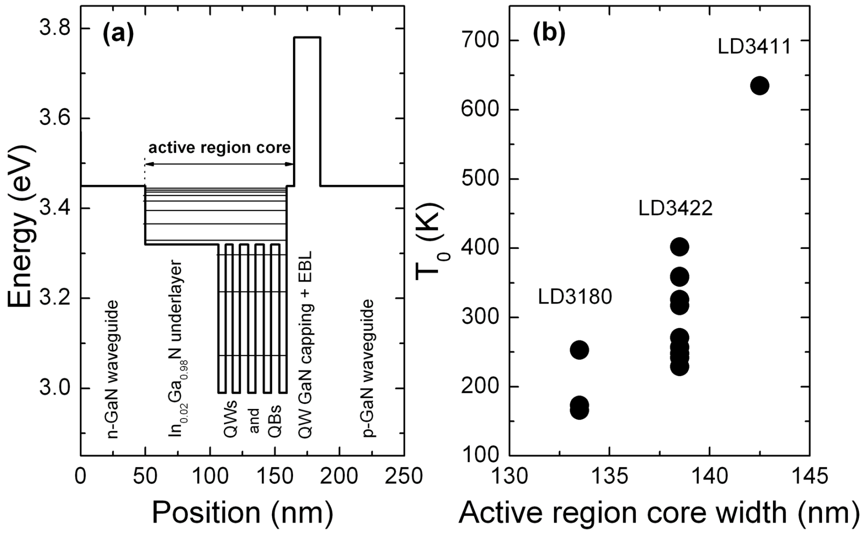

Figure 5.8: Dependance of the characteristic temperature on the total thickness of the active region core (i.e. including QWs, QBs, GaN cap and InGaN underlying layer) for structures consisting of a sequence of five 4.5-nm-thick QWs.

Sample Name	QW width (nm)	QB width (nm)	Total core width (nm)	I_{th} (mA)
LD3180	4.5	5.5	133	210
LD3422	4.5	10.0	138	475
LD3411	4.5	10.0	143	486

Table 5.1: Major details concerning dimensions of the active region core layers and best threshold current values obtained for LDs belonging to the corresponding datasets.

the thickness of the core region. The data consisted of a three sets of samples. In each case the analyzed LDs had a sequence of five 4.5 nm thick $In_{0.1}Ga_{0.9}N$ QWs. Constant QW geometry assured roughly unchanged carrier confinement. In contrast, the thickness of $In_{0.02}Ga_{0.98}N$ QBs was changed from 5.5 nm to 10 nm and then the GaN cap layer from 6 nm to 10 nm. The underlying layer consisting of 50 nm of $In_{0.02}Ga_{0.98}N$ was kept unchanged. Major parameters of the analyzed samples are presented in Table 5.1.

It seems that it is possible to develop a LD design characterized by a limited temperature sensitivity of a given device, which can be achieved by utilization of thick barriers. The approach eliminates the negative impact of the internal piezoelectric fields that appear in QWs with the extended width and increased In content. However, the procedure suffers from over two-fold increase of the threshold current (see Table 5.1). Although the active volume remains roughly unchanged in such configuration, it would be reasonable to expect the excess nonradiative recombination losses due to a larger volume of the confining material. Providing that the quality of barrier and QW capping material is good enough and the nonradiative processes take place mainly at the heterointerfaces, it would be possible to keep the nonradiative recombination rate at a roughly unchanged level. Consequently, the threshold condition would be determined by changes in optical confinement, that can be tuned by optimization of the entire waveguide. Thus the proper design and fabrication of the active region core can possibly lead to the improved temperature stability, which would be reached without the expense of the increased threshold.

5.4 Effects induced by the electron blocking layer

The quality of EBL is of a crucial importance and can hardly be overestimated. This thin layer of a wider band gap material than the material used in the active region is necessary to achieve the possibly highest internal quantum efficiency. As it was mentioned previously in Chapter 3, hole mobility through III-nitride-based epitaxial layers of the p-type conductivity is strongly diminished by the heavy doping (up to 10^{20} cm^{-3}) with Mg acceptors and an large hole effective mass. For example the effective mass of holes in a heavy hole valence subband reaches 1.595 m_0. As a consequence of a heavy doping, excess scattering mechanisms impede the hole mobility, reducing it down to 2 cm^{2}V^{-1}s^{-1} at room temperature [106]. The corresponding values determined for conduction band electrons in GaN concerning the mobility and the effective mass can be estimated as 200 cm^{2}V^{-1}s^{-1} and 0.2 m_0, respectively [107]. Such a huge difference in electron and hole mobilities is responsible for the electrons' tendency to overflow the active region, which has a devastating influence on the device's performance and its temperature stability.

Figure5.9(a) presents electroluminescence spectra collected for two structures: LD3460 analyzed at the beginning of the chapter and a similar structure without the EBL. The sample with the EBL incorporated directly above the active region is characterized by a strong luminescence from QWs. Despite a strong QW-related emission band centered at 3 eV observed for the sample without the EBL, there is also a blue luminescence band from p-type GaN around 2.8 eV. This effect evidences a strong electron overflow into the p-type layers of the laser stack. Figure 5.9(b) depicts the L-I curves measured for both structures.

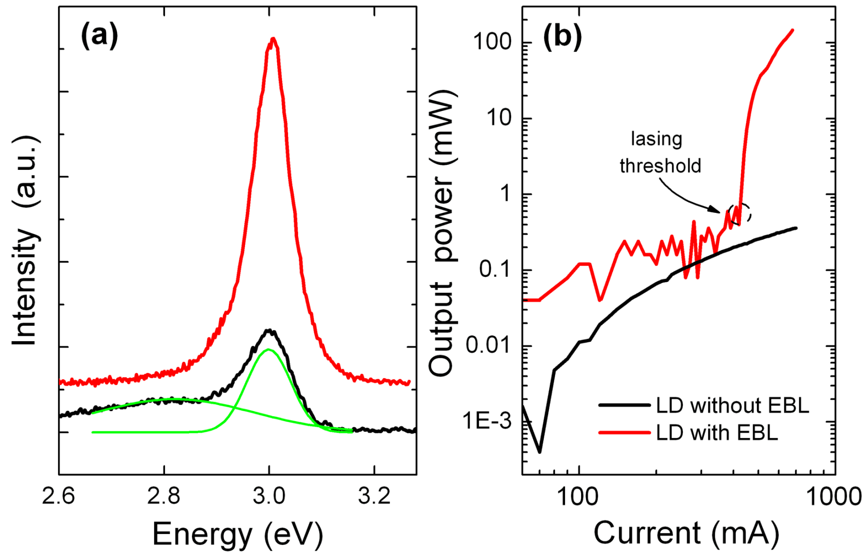

Figure 5.9: Electroluminescence spectra collected for two five-QW-based LDs: with (LD3460) and without the EBL (a) and a corresponding L-I curves (b).

The lack of the EBL reduces the internal quantum efficiency so much, that the lasing threshold cannot be reached. Consequently, the difference in the optical power emitted by both structures under a similar electrical excitation varies by three orders of magnitude in favor of the EBL-consisting sample. Additionally, the analysis of the operating voltage reveals the lack of significant differences. Thus it can be concluded that the EBL does not yield a major contribution to the overall amount of the device's series resistance as assumed previously.

Despite a beneficial influence that the EBL imposes on a high temperature device operation, our observations suggest that it can also inhibit the LD's performance in a low temperature range [108]. As commonly observed for the electroluminescence from InGaN QWs, the optical intensity increases with the lowering ambient temperature [109]. Carriers become less mobile and much better confined by the In clustering effect inducing band profile fluctuations. Consequently they can no longer reach nonradiative recombination centers. Large band offsets between III-nitrides [66] form however significant potential barriers that can hardly be overcome by injected holes. Especially the insertion of a 20-nm-thick $Al_{0.2}Ga_{0.8}N$-based EBL between p-type GaN and the active region inhibits severely an efficient hole injection. By solving self-consistently the Schrödinger and Poisson equations

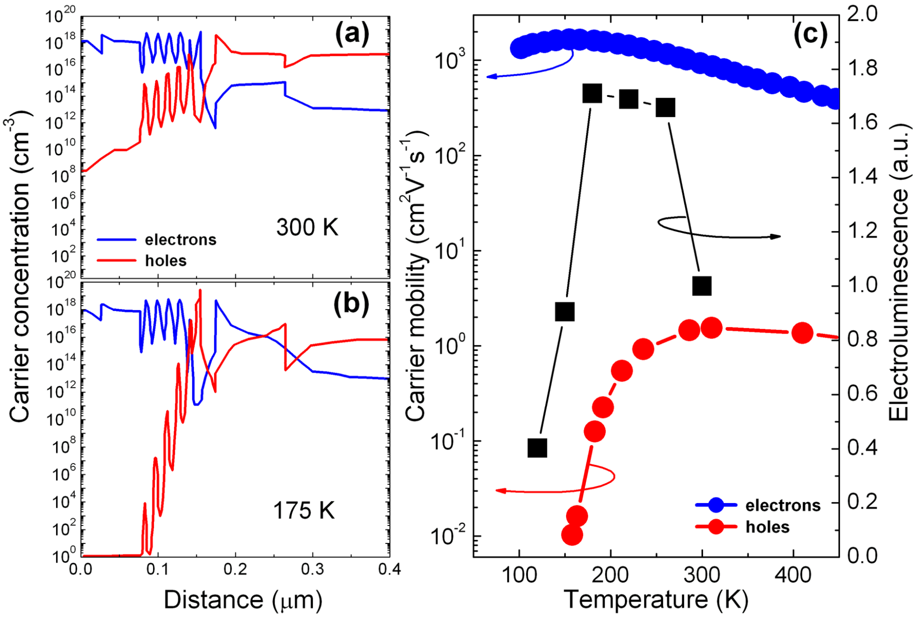

Figure 5.10: Carrier distribution across a five-QW-based active region at 300 K (a) and 175 K (b) calculated in cooperation with P. Mensz together with a temperature dependance of carrier mobilities taken from Ref.[66] and the electroluminescence collapse collected for a real five-QW-based LD driven by 1 mA of CW current (c).

together with the current continuity equation, we were able to trace the carrier distribution in a positively biased laser structure by means of the LASTIP simulation package [110]. Figure5.10(a,b) depicts the inhomogeneous hole distribution for the LD's active region consisting of five 4.5-nm-thick $In_{0.1}Ga_{0.9}N$ QWs. This effect can be greatly enhanced by the temperature drop from 300 K to 175 K as a result of the deionization of Mg acceptors together with the considerable reduction in the hole mobility .

Consequently, the unexcited QWs can remain below the transparency level reducing severely internal efficiency and increasing internal losses [111, 112]. Positive charge accumulated on the p-side of the EBL invokes additional contribution to the electric field that enhances the electron leakage over the EBL into p-type waveguide were electrons finally recombine without any contribution to the lasing mode. The inhibited hole injection, enhanced absorption by the unexcited QWs and the carrier leakage followed by nonradiative recombination events lead to the final electroluminescence collapse taking place below 200 K as presented in Figure 5.10(c). The effect corresponds well to the rapid reduction of the hole mobility in p-type GaN doped with Mg up to 8.6×10^{19} cm^{-3} as taken from Ref.[66]. The photoluminescence data achieved by a resonant optical excitation of a similar laser stack does not reveal such result [108]. Thus it is reasonable to attribute the observed effect solely to the electrical carrier transport mechanisms. The corresponding distribution of the optical gain across the active region consisting of different QW number will be a subject of a closer analysis carried out in Chapter 9.

5.5 Major recombination mechanisms

Chapter 2 considered mainly radiative transitions contributing to a useful optical gain. Since the mechanism of the quantum well carrier capture is not completely efficient and the active region is never of a perfect quality, carrier loss always occurs. Nonradiative and leakage current components contribute to the total amount of terminal current that needs to be supplied. The analysis of these non-ideal contributions takes into account many different mechanisms. Nonradiative transitions occur via deep-level states in the bandgap induced by point defects, threading dislocations and interface recombination at heterobarriers. On the other hand, carrier leakage consists of threading dislocation mediated current shunts [113], vertical carrier overflow over QW-based active region, lateral current spreading and thermal escape of high energy carriers excited into the bulk-like states beyond the edges of QWs.

According to the approach represented by Equation 2.3.2, the total driving current applied to device's terminals consist of the following components: nonradiative (I_{nr}, spontaneous (I_{sp}), stimulated (I_{st}) and leakage current (I_l).

$$I = I_{nr} + I_{sp} + I_{st} + I_l. \tag{5.5.1}$$

It is worth noticing here that, due to a low probability in wide bandgap materials, the mechanism of Auger recombination, which is of profound importance for arsenide- and phosphide-based LDs, is usually neglected in the analysis of III-nitrides. However, observations emphasizing the significance of this mechanism have been reported and stressed recently [114].

Now we will try to focus in the major recombination mechanisms at threshold. The reader needs to take into account the following arguments. First of all, stimulated recombination can be neglected. As a result the optical power coupled out of a given device is

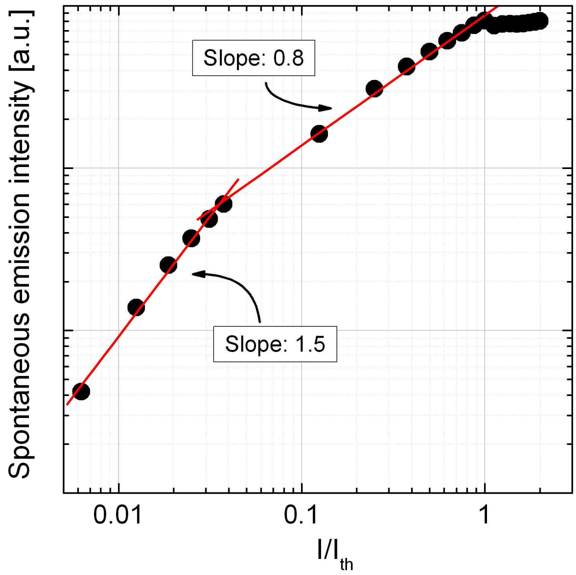

Figure 5.11: Integral of spontaneous emission spectra of a typical laser diode with an active region consisting of five quantum wells.

proportional solely to spontaneous recombination, which is a bimolecular type of radiative transition, meaning that $I \propto n^2$ and also $P \propto n^2$. Alternatively nonradiative and leakage processes are monomolecular, which means that $I \propto n$. Hence, depending on the dominant recombination mechanism occurring inside a resonant cavity, a typical log-log plot of the spectrally integrated spontaneous emission versus drive current increases linearly with the slope of about 1 or 2, indicating that either radiative or nonradiative recombination prevails, respectively.

Following the approach presented above, Figure 5.11 identifies roughly the major recombination mechanisms of our typical nitride-based laser diode with an active region consisting of five 4.5-nm-wide quantum wells embedded between 7-nm-thick quantum barriers. The true spontaneous emission signal was collected by an optical fiber through an opening in a top contact electrode. The linear dependance with a slope of 1.5 indicates that in a low current range nonradiative recombination is a dominant recombination mechanism. By further increasing the drive current, the slope of the dependance changes to about 0.8 suggesting that just below threshold nonradiative recombination centers saturate and also the current spreading effect takes place outside the area of the opening in a top contact electrode. As a result, spontaneous recombination prevails and one can finally deal with a uniformly excited region characterized by a constant material gain distribution clamping above threshold, which can be evidently observed in Figure 5.11.

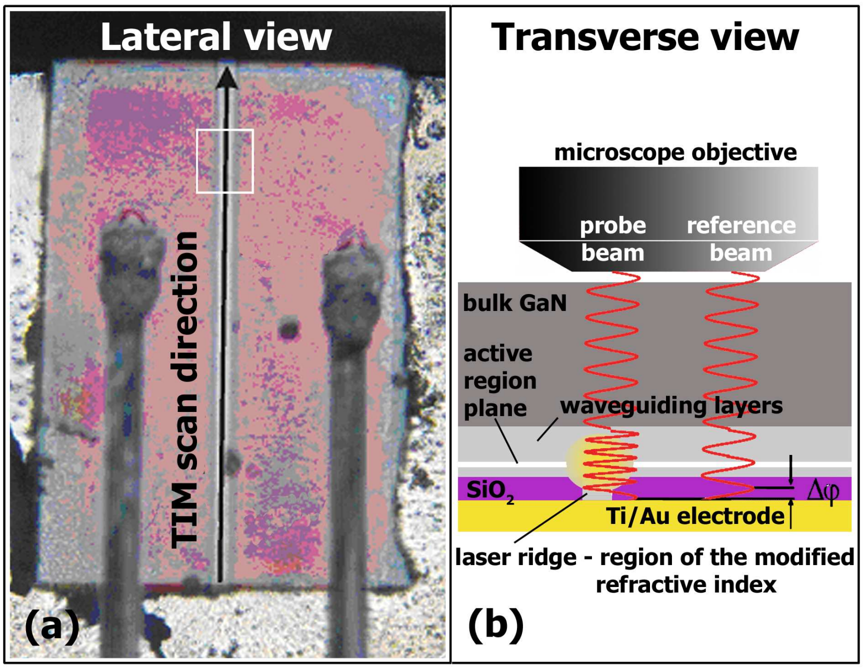

Figure 5.12: The view on a flip-chip mounted LD through the polished bulk GaN substrate with the designation of the TIM scan direction (a) and the schematic picture of the measurement idea (b).

In order to investigate the uniformity of the carrier injection, we performed the technique of transient interferometric mapping (TIM) [115]. The analysis was carried out at Vienna University of Technology in cooperation with S. Bychikhin and D. Pogany. For the purpose of this measurement, the n-type Ni/Au contact electrode was removed from the GaN substrate by polishing and the bonding wires were attached directly to the crystal offering a direct insight into the electroluminescence signal along the resonant cavity as depicted in Figure 5.12(a). Figure 5.12(b) presents the basics of this technique. The infrared probe leaser beam travels through the transparent GaN substrate and the epitaxial layers in the transverse direction, is reflected by the p-type Ti/Au metallization deposited on the mesa stripe and returns the same way back. The probe beam is interferometrically combined with the reference beam The observed phase shift $\Delta\varphi$ induced by changes in temperature and carrier concentration yielded information on the spatial distribution of the current flow with the resolution of 2 μm.

Figure 5.13(a) presents the phase shift we derived from the TIM scan carried out along the resonator axis. Significant changes in the phase distribution indicated nonuniformities in the current flow path. They correspond well to passive regions revealed by means of the optical microscopy. The magnified image of the resonant cavity under the low electrical excitation depicted in Figure 5.13(b) shows the existence of a dark region. These regions

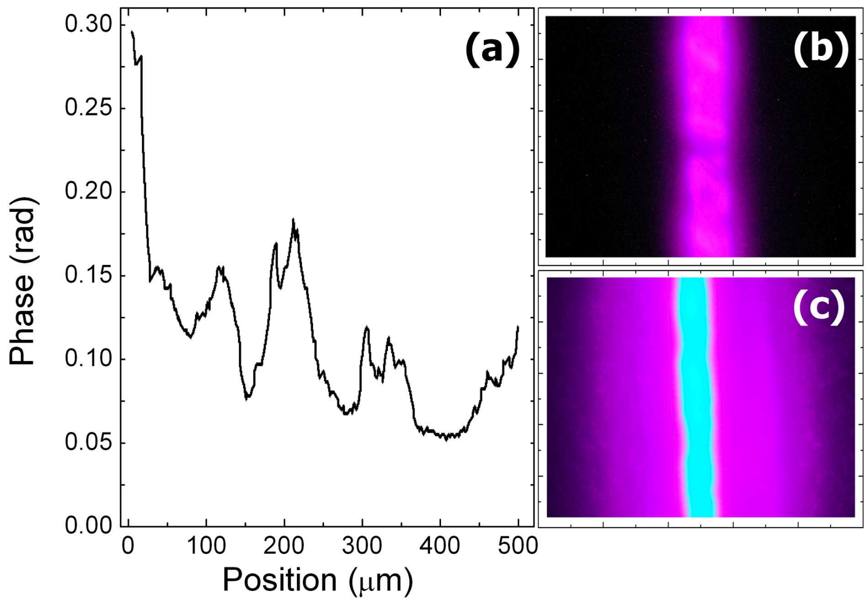

Figure 5.13: Phase shift as a function of the position along the mesa stripe determined by the TIM scan (a) and magnification of a resonant cavity under a low (b) and high (c) electrical excitation revealing the existence of a passive region that disappears with increasing driving current.

appear due to spacial inhomogeneities in electrical properties of some LDs. The origin of these fluctuations can be traced back to the epitaxial growth modes induced by the local degree of the substrate misorientation.

Once the electrical excitation is increased above a critical level, the passive regions disappear as presented in Figure 5.13(c). The tendency corresponds to to the behavior presented in Figure 5.11. This effect can be explained by either a critical voltage that needs to be supplied in order to induce the effective electrical transport or the self-pumping by the cavity mode. Both effect are disadvantageous as they lead to the increased operating voltage or excess internal propagation losses responsible for a significant reduction of the L-I slope.

Chapter 6

Optical gain

The basic goal of this chapter is to investigate the optical features of the laser structures grown by two alternative techniques, i.e. MOCVD as well as PAMBE, which are presently under development at Institute of High Pressure Physics. The structures considered in the analysis emitted light within a broad spectral range starting from 390 nm up to 460 nm. The major part of the research involved utilization of a variable stripe length excitation method. By means of this technique it was possible to asses the optical properties of the investigated structures including amplification of the guided mode and propagation losses. The conclusions could then be used as suggestions of possible device optimization steps.

6.1 Variable stripe length method

For the purpose of this dissertation, the majority of gain measurements have been carried out by means of the optical excitation as the main characterization technique. The construction of the experimental setup was one of the major requirements that had to be satisfied before the completion of the following dissertation. The contactless approach employed by this measurement technique eliminates problems with electrical injection. The method is capable of supplying information necessary to compare the optical properties of the active region and waveguiding layers of different laser structures without a need for the usage of high resolution spectral analyzers. A much more precise spectral instrumentation is needed in case of the commonly used technique based on the analysis of a longitudinal mode modulation depth [116].

6.1.1 Basic physical concept

The Variable Stripe Length (VSL) excitation technique employs, in the first approximation, a simple idea of a one-dimensional amplifier rod of a length L and a cross-sectional area A. At high excitation conditions induced by high pump power, photons emitted spontaneously at some point within a length element dz are subject to optical amplification as they are guided along the excited active medium. The change in a number of photons in a given mode is reflected by a relevant intensity increase. Formally, the light intensity I entering an infinitesimal length element dz is subject to an increase caused mainly by the material gain g_{mat} according to the following formula [117]:

$$\frac{dI}{dz} = (\Gamma\ g_{mat} - \alpha_i)I + R_{sp}N_{ex}h\nu\frac{\Omega(z)}{4\pi} \tag{6.1.1}$$

The first summand on the right hand side of the equation represents stimulated emission depending on optical confinement Γ and internal propagation loss α_i. From now on, the entire term in brackets will be referred to as a net modal gain g_{mod}. The second summand, through the spontaneous recombination rate R_{sp} and the excited carrier population N_{ex}, accounts for the intensity increase due to a fraction of spontaneous emission entering a solid angle along waveguiding layers.

Although the main concept is relatively simple, a set of strict experimental constrains needs to be followed in order to yield reliable results. Additionally, when applied to systems employing planar waveguides with no lateral waveguiding, such as in the case of this study, samples with high gain coefficients and significantly large excitation length need to be secured in order to validate the assumption that a major part of stimulated emission arises from regions deep into the sample. A flux of photons emitted by the length elements dz close to L experiences the largest single pass gain. As a result, a solid angle Ω(z) subtending the exit amplifier face can be regarded as constant and equal to $\Omega(z)\ \cong \Omega = A/L^2$, where A stands for the cross sectional area of the amplifying region. Under this assumption Equation 6.1.1 can be integrated over the entire length of the amplifier giving total intensity emerging from the sample edge:

$$I_{ASE} = \frac{J_{sp}(\Omega)}{g_{mod}}(e^{g_{mod}L} - 1); \tag{6.1.2}$$

where

$$J_{sp}(\Omega) = R_{sp}N_{ex}h\nu\frac{\Omega}{4\pi} \tag{6.1.3}$$

defines spontaneous emission per unit length emitted along waveguiding layers.

As depicted in a schematic picture of the experimental setup (Figure 6.1(a)), each sample emitting from near-UV to green spectral range is in practice optically excited by a frequency tripled (355 nm) or quadrupled (266 nm) Nd:YAG pulse laser with a pulse duration of 10 ns and a repetition rate of 20 Hz. The pumping beam passes through a computer-controlled dual-prism attenuator stabilizing the excitation power at the desired level. After crossing through a beam splitter, part of the beam is directed towards the power meter. The remainder of the optical power is focused by a cylindrical lens into a stripe of a width of about 30 μm to form the excitation area on the sample surface. The length of the stripe is varied by a stepper-motor-controlled blade (Figure 6.1(b)).

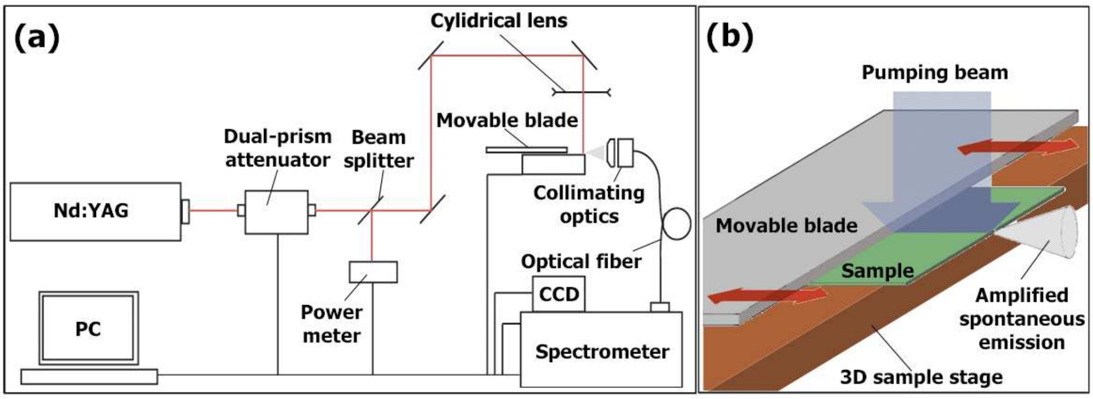

Figure 6.1: Schematic picture of a practical realization of a variable stripe length excitation.

Partially coherent electro-magnetic field, traveling along the epitaxial layers, grows exponentially with an increase of the excitation length. Amplified spontaneous emission (ASE) intensity signal emerges out of a sample edge (Figure 6.1(b)) and is collected by external collimating optics and then coupled into the optical fiber having a 200 μm thick quartz core and a numerical aperture of 0.39. Finally, the optical signal is collected and analyzed by the spectrometer equipped with a thermoelectrically cooled CCD camera.

Room temperature excited carrier lifetimes measured for InGaN-based LDs remain at the order of 600 ps [118]. They are considerably shorter than the length of 10 ns-long pulses of the exciting laser applie with the repetition rate of 20 kHz. Thus an assumption that the system can be considered as remaining in instantaneous equilibrium at all times seems to be reasonable within some accuracy limit defined mainly by the pump power stability. Because of the fact that the detected signal is an integral over many pulse durations, it depends on the temporal pulse shape. In case of the frequency-tripled Nd:YAG laser used in our experiments the power stability of the output laser beam generated by a third harmonic crystal is estimated to be $\pm 5\,\%$. The laser output power was additionally corrected for temporal variations by a computer-controlled feedback loop adjusting the settings of the coupled-prism attenuator in order to achieve possibly the best temporarily stable optical excitation.

The optical pumping geometry used in VSLM experiment creates excitation conditions similar to the situation found in semiconductor LDs, where the inverted region is laterally limited to a narrow stripe by a spatial confinement of injected carriers. Thus conclusions derived from optical excitation experiments should be easily applicable to real devices driven by electrical current.

Raw data consisting of a set of ASE spectra collected from the sample edge for different lengths of excitation stripe is depicted in Figure 6.2(a). ASE exhibits a weak threshold behavior due to the onset of stimulated emission as pump power is being increased [119]. Consequently, its bandwidth is considerably narrower and spectrally shifted compared to a pure spontaneous emission due to a spectral shift in positions of spontaneous emission and gain maxima. By fitting intensity changes versus excitation length detected for a particular wavelength, a net modal gain at this frequency can be deduced. However, before proceeding with a fitting routine, further experimental constrains and assumptions need to be satisfied.

6.1.2 Experimental constrains

First of all, a *constant collection efficiency* which is independent of the pumping length should be secured. Collection efficiency can be strongly influenced by the spatial dependance of $\Omega(z)$ which is negligible in case of two-dimensional waveguides but cannot be ignored in case of planar ones, which do not secure photon waveguiding in lateral direction. For this reason the signal detected for longer excitation stripes, for which the collection efficiency was assumed as constant, is primarily taken into account in a process of a data fitting. Additionally, we used a gradient-index lens with high numerical aperture designed in such a way than it transforms a point-like light source placed at the entrance optical plane of the lens into the corresponding image at the exit plane where the signal is directly coupled into an optical fiber with a large core diameter of 200 μm. The lack of traditional microscope objective improves significantly collection efficiency and rules out an optical depth-of-field effect which can be a source of experimental artefact occurring when a focusing spot is placed well inside the sample and leading to apparent gain values even though a photon flux is subject to absorption [120].

Secondly, a *uniform pump power* along the excitation stripe has to be also essentially secured. In order to avoid the Fresnel diffraction deteriorating homogeneity of the excitation stripe, the sample should be placed as close as possible to the movable edge of the slit. Practically, it means that the blade of the slit almost wipes the surface of the epitaxial layers. The sample is additionally placed in the middle of the pump profile with a cross-sectional diameter of about 5 mm. The changes of the excitation stripe cover a maximum length of 500 μm, thus a constant pumping rate is additionally secured.

6.1.3 Gain saturation

Finally, the sample should be characterized by a constant gain along the amplifier axis. This is regarded to be true only for a limited range of excitation stripe length values. In case of our samples it is commonly observed that for the excitation stripes longer than roughly 200 μm, ASE intensity can build up so much as it travels through the active media that it considerably depletes the excited carrier population. Consequently a small signal gain g_0, which is independent of signal intensity, needs to be modified in order to take into account the reduction of the inverted carrier population and hence *gain saturation.*

A two-band InGaN-based semiconductor gain medium is an inhomogeneously broadened four-level system involving In-clustering-related localized states with rapid relaxation due to carrier-carrier scattering [29]. For inhomogeneously broadened amplifiers, excited carrier population and consequently small signal gain g_0 should be modified by signal intensity I_{sat} that saturates the active medium according to the following relation [117]:

$$g_{mod}(z) = \frac{g_0}{\sqrt{1 + \frac{I(z)}{I_{sat}}}}, \tag{6.1.4}$$

resulting in spatially changing net modal gain $g_{mod}(z)$.

Frequency-dependent gain saturation originates in the overall inversion decrease caused by great rates of stimulated emission or absorption which is often related to as a *spectral* *hole burning*. Reduction in separation of quasi-Fermi levels for electrons and holes occurs because of the filling of spectral holes by intraband collisions. Thus saturation occurs for the highest energies at first, following condition required for positive gain 2.4.2.

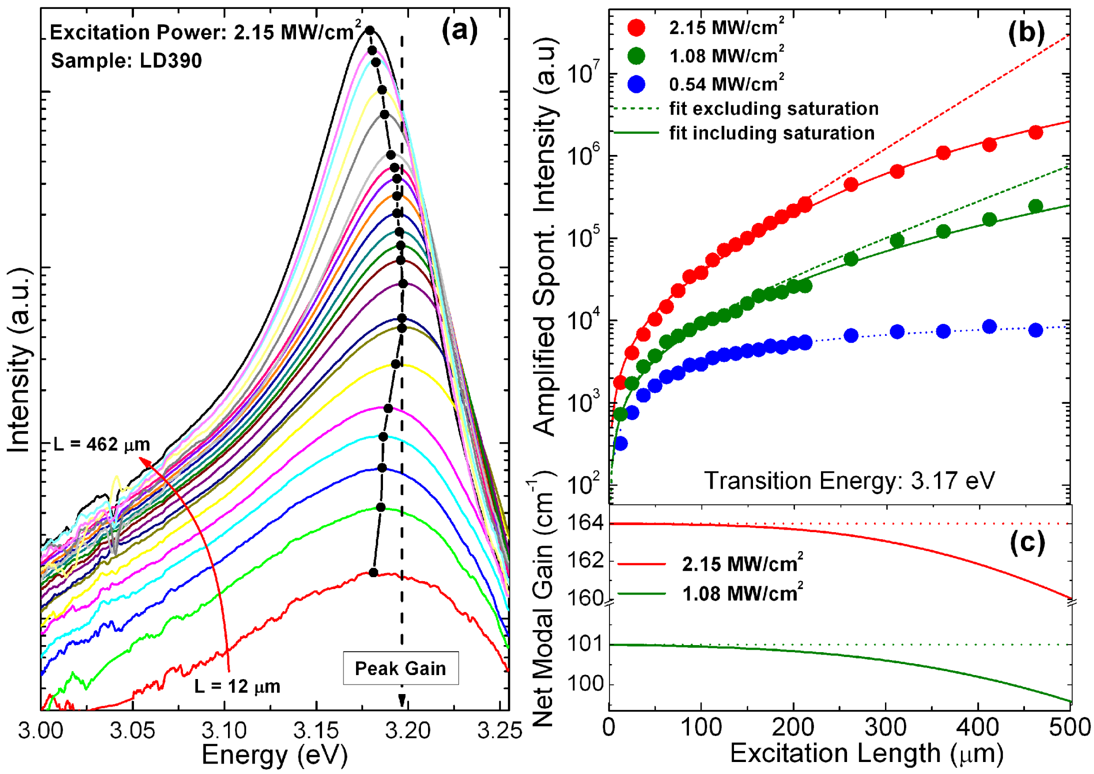

Figure 6.2: (a) ASE spectra of sample MOVPE390nm collected for different excitation stripe lengths ranging from 12 μm to 462 μm at maximum pump power of 2.15 MW/cm^2; (b) Intensity change as a function of excitation length at transition energy of 3.17 eV fitted with equations 6.1.2 employing constant gain (dotted curve) and gain saturating according to equation 6.1.4 (solid curve); (c) changes of modal gain induced by increasing ASE intensity (solid curve) derived from saturation behavior observed in section (b) compared to its small signal value (dotted line).

Figure 6.2(b) depicts ASE intensity versus excitation stripe length taken at 3.17 eV for three different pumping rates as recorded for the sample LD390 (see Appendix A for structural details). Unsaturated net modal gain values derived from the experiment are 164 cm^{-1}, 101 cm^{-1}, -38 cm^{-1} for excitation power of 2.15 MW/cm^2, 1.08 MW/cm^2 and 0.54 MW/cm^2, respectively. The curves used to fit the data either exclude (dashed ones) or include (solid ones) gain saturation effects taken into account by Equation 6.1.4. The data shows clearly that in case of positive gain values ASE intensity recorded for excitation stripes longer that 200 μm deviates significantly from theoretical model which does not include saturation. On the other hand, when absorption instead of gain occurs, saturation effect is missing and does not have to be included in the analysis.

Raw data presented in Figure 6.2(a) presents a characteristic behavior observed typically at high pumping rates for which large excited carrier population is generated. With initial increase of the excitation stripe length, spectra recorded from the sample edge blueshift towards 3.19 eV where the corresponding gain curve (presented in Figure 6.5 as the one with the highest gain for the sample LD390) reaches its maximum. It can be concluded that the unamplified spontaneous emission occurs at low transition energies corresponding to recombination from localized states. The stimulated emission, as indicated by the position of the gain curve, takes place for higher energies related to transitions from unbound states. As the distance covered by the photon flux traveling along the waveguide gets longer, stimulated recombination events amplify the high energy spectra and blueshift the spectral position of the luminescence peak. Once the transitions occur, the empty states are filled by new carriers which thermalize from higher energy states within a few femtoseconds [119]. Finally, when the excitation stripe length exceeds 200 μm, as depicted in Figure 6.2(b), saturation at the highest energies occurs. The apparent gain value decreases, leading to the collapse of the high energy tails. As the light amplification gets more efficient for lower transition energies, which have not been subject to the significant depletion in carrier population, a consecutive redshift of the peak energy position becomes clear.

In Figure 6.2(c) one can simultaneously find changes of the net modal gain for the pump power values of 2.15 MW/cm^2, 1.08 MW/cm^2 versus the excitation length derived by means of Equation 6.1.4. The initially unsaturated small signal gain starts to decrease significantly as the rising excitation length induces an increase of intensity. Larger photon flux reduces the population of excited carriers, which initially has little effect on gain, because of negligible reduction of quasi-Fermi level separation.

Figure 6.3 presents the same dependance as the one depicted in Figure 6.2(c), but the relation described by Equation 6.1.4 is extended to larger excitation lengths and corresponding intensities deduced from the experiment. It can be clearly seen that the modal gain starts to be reduced significantly once the critical excitation length of about 1 mm is

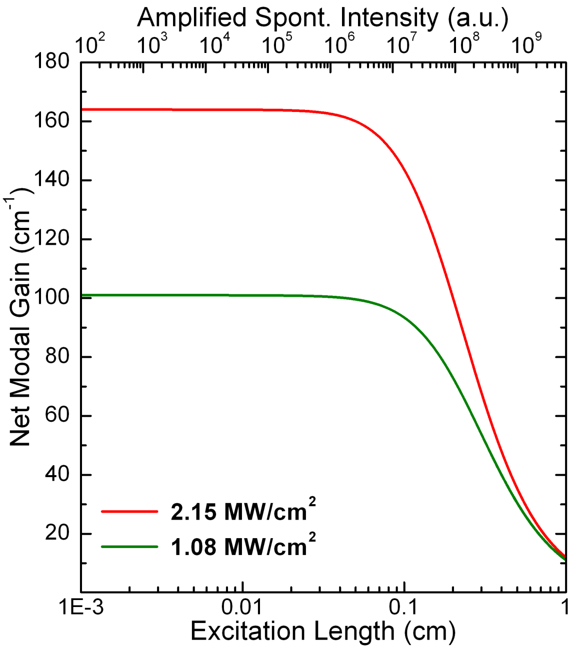

Figure 6.3: Extrapolation of the unsaturated small signal gain evolution presented in figure 6.2(c) deduced from VSL excitation experiment plotted as a function of ASE intensity and a corresponding excitation length as derived from the experiment.

exceeded. Rapid increase (a few orders of magnitude) of the ASE intensity depletes severely the excited carrier population. Under extremely large photon flux, intensified competition between stimulated absorption and emission rates forces the system to approach transparency for a given transition energy never leading to conversion from gain to absorption as can be seen in Figure 6.3.

The estimation shows that for ASE intensities being two orders of magnitude larger than the observed in our experiments, gain would start to collapse immediately towards transparency. A simple approach suggests that in such a case the total number of photons in a given mode exceeds the number of possible carrier transitions explaining the fact that, in the limit, apparent transparency can appear simultaneously for different photon energies.

For the sake of completeness it also should be noted here that every photo-excited infinitesimal length element dz is a source of a photon flux propagating both in forward and backward lateral direction along amplifier axis. Thus a complete symmetry and a uniform intrinsic excitation along the amplifier would be satisfied, if it were not for the fact that the reflectivity of the uncoated facet formed by a cleaved sample/air interface is about 0.16. Thus some part of the ASE is directed back to the waveguiding layers and does not emerge out of the sample. Additional photon flux subject to the internal reflection at the facet disturbs the symmetry of the system, enhances the excited carrier recombination and depletes the carrier population available to the electromagnetic wave, which propagates towards the collecting optics. As a result, apparent differential gain can be underestimated and simultaneously saturation effects can be subject to some overestimation. These effects, however, have been neglected in the analysis of the experimental data.

Saturation behavior of optical amplifiers can be a useful indication of a crystal quality of the material as it depends on spontaneous (τ_{sp}) and nonradiative (τ_{nr}) recombination lifetimes. From steady-state excitation condition requiring detailed balance between upward and downward transition rates, the following relation between saturation intensity and recombination lifetimes can be derived [121]:

$$I_{sat} \sim \frac{\tau_{sp}}{\tau_{nr}} \tag{6.1.5}$$

Equation 6.1.5 indicates that increasing nonradiative recombination lifetime leads inevitably to reduction of light intensity saturating a considered amplifier system. Thus improved crystal quality reduces internal losses and thus threshold current for laser emission at the expense of reduction of the unsaturated material gain.

Gain saturation caused by spectral hole burning plays an important role in both a multi-mode operation and a high-speed modulation of laser diodes. In order to avoid this effect, the maximum gain-length product can be assessed by the VSL excitation. The results can suggest the optimum laser resonator length in terms of reduced threshold current density and a best quality of thermal management.

6.1.4 Transient pumping and hot carrier effects

All laser structures studied by VSLM were optically excited up to the power densities of a few MW/cm^2. Information concerning the heating of the system and its instantaneous relaxation is necessary for a proper assessment of the optical gain derived from our experiment. We will try to consider shortly carrier heating effects and their impact on the results presented in the next subsection.

The laser structures, which were subject to a VSL excitation were optically pumped through waveguiding layers by either third (3.49 eV) or fourth (4.66 eV) harmonic of Nd:YAG laser. The pumping beam was not absorbed resonantly by a thin active layer consisting of a sequence of QWs but rather by a 100 nm-thick upper waveguide, which was formed either by GaN or AlGaN depending on the sample and its emission energy. In case of a 100 nm-thick GaN waveguide, the absorption coefficient of GaN is as high as 1.5×10^5 cm^{-1}, which corresponds to the absorption length of 67 nm [122]. As a result, it can be indeed assumed that the majority of the pumping photons is absorbed by this layer. Excited carriers created by the incident beam diffuse, thermalize and are subsequently captured by QWs where they need to relax down to lowest quantized energetic levels.

For large injected carrier concentrations ranging from 10^{18} cm^{-3} up to 10^{20} cm^{-3} there are mainly two major relaxation mechanisms depending on carrier-carrier scattering [123]: interaction with lattice through LO phonon emission and direct collision with the electron gas. Although the former relaxation path is believed to be the dominant one, the latter cannot be neglected as it leads to the formation of hot plasma. As a consequence, carriers can be rejected out of lasing states into higher electronic levels in the well. This effect saturates the differential gain considerably [42].

It is possible to estimate the impact of carrier heating on the gain measurements by analysis of the high-energy tail of the photoluminescence spectra. Setting a requirement that the density of states varies much slower than highly energetic carrier distribution the following relation for the spontaneous emission can be defined [122]:

$$I_{spont} \propto e^{-\frac{h\nu - E_{fn}}{kT_e}} \tag{6.1.6}$$

Equation 6.1.6 makes use of the fact that spontaneous emission rate for band-to-band recombination is proportional to the product of electron and hole distribution functions with additional assumption that the carrier temperature T_e is equal for electrons and holes [124] and differences in carrier effective mass is not decisive. E_{fn} was assumed to roughly equal about 3.02 eV, as determined in Chapter 9 for a real device at threshold. Figure 6.4 shows photoluminescence spectra collected for the three highest pumping rates (2.17 MW/cm^2, 1.90 MW/cm^2, 1.34 MW/cm^2) which were used for the optical excitation in VSL measurement.

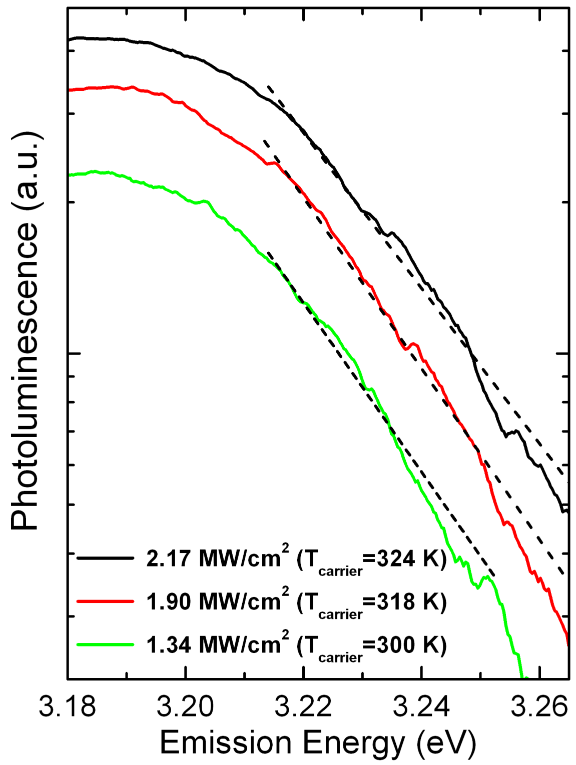

Figure 6.4: High energy tail of spontaneous emission spectra taken for three pumping rates: 2.17 MW/cm^2, 1.90 MW/cm^2, 1.34 MW/cm^2 fitted by means of equation 6.1.6 (dashed lines) with derived carrier temperatures of 324 K, 318 K, 300 K, respectively

Rough estimations indicate that the temperature of injected carriers is not significantly higher than the temperature of the crystal lattice. Determined temperature does not exceed 324 K for the highest pumping rate used in this study. The initial carrier temperature can be even larger, but the effective carrier relaxation time of 9 fs [122] is enough to cool carriers down to room temperature as derived from the time-integrated spectra presented in Figure 6.4. A simple analysis of the Fermi distribution function revealed that the population of states lying above Fermi level increases by about 8 % when the temperature is changed from 297 K to 324 K. Thus we tend to assume that the carrier heating effects did not introduce a significant distortion to the gain curves presented below.

6.2 Experimental data obtained by optical excitation

Because of the fact that there are two alternative epitaxial techniques being developed by research groups involved in the growth of III-nitrides, the data presented in this section will be divided into two major parts. First of all, the analysis of MOVPE-grown samples LD370, LD390, LD410 and LD430 emitting in the spectral ranges around 370 nm, 390 nm, 410 nm, 430 nm, as designated by the sample names, will be presented. Then the properties of the sample LD410 will be compared to the similar structure LD405 grown in PAMBE reactor in order to investigate the differences the alternative growth techniques induce on optical properties. Advantages and drawbacks of both of them will be directly related to the optical features of the analyzed samples. The major details concerning the parameters of the active region design of the analyzed samples are presented in Table 6.1:

Sample Name	QW Design	QB Design	Optical Confinement
LD370	5 x 5 nm of GaN	10 nm of $Al_{0.04}Ga_{0.96}N$	0.12
LD390	5 x 5.5 nm of $In_{0.08}Ga_{0.92}N$	6 nm of GaN	0.038
LD410	5 x 4.5 nm of $In_{0.10}Ga_{0.90}N$	7 nm of $In_{0.02}Ga_{0.98}N$	0.069
LD430	5 x 5.5 nm of $In_{0.14}Ga_{0.86}N$	6 nm of GaN	0.038
LD405	5 x 3.0 nm of $In_{0.10}Ga_{0.90}N$	7 nm of $In_{0.02}Ga_{0.98}N$	0.051

Table 6.1: Major parameters of the active region influencing the optical properties of the analyzed samples. The waveguiding layers are roughly unchanged.

Closer details of the investigated laser structures are presented in Appendix A for the reader's reference.

6.2.1 Optical properties of MOCVD-grown laser structures with different In content

Efficient semiconductor light sources emitting in the wide spectral range from UV to blue-green open perspectives for many practical applications. For this reason, the detailed information on the optical gain characterizing such structures is of the highest importance.

Experimental data concerning the amplification of light derived from optical excitation by means of VSLM is depicted in Figure 6.5. Peak modal gain values correspond roughly to the values expected in a resonant cavity at threshold, which usually do not exceed 100 cm^{-1}.

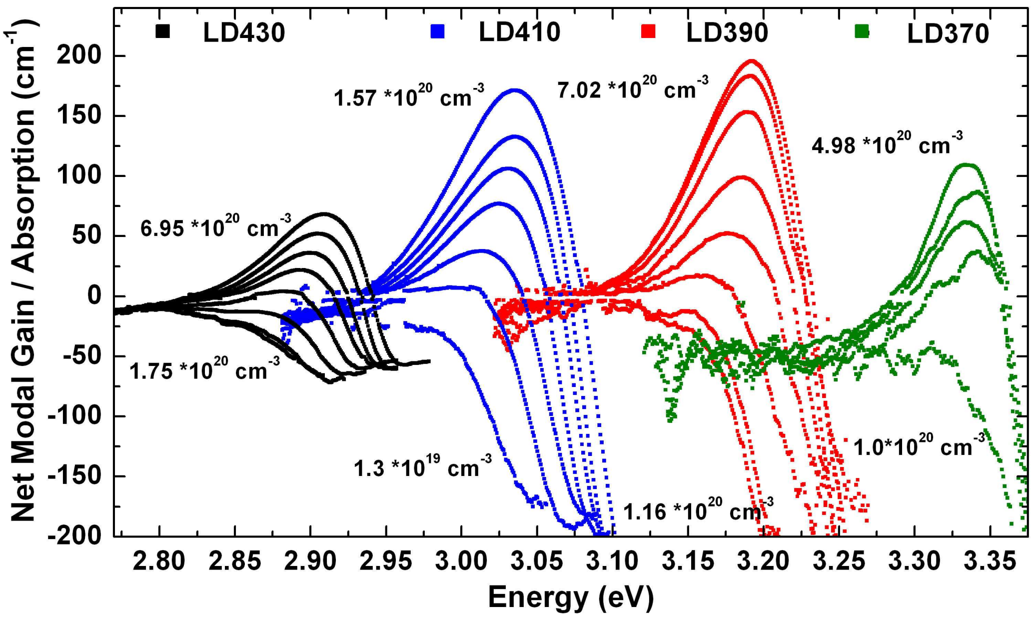

Figure 6.5: Modal gain curves determined experimentally for samples: LD370, LD390, LD410 and LD430. Minimum and maximum carrier concentrations estimated for two extreme pumping rates were calculated for each sample separately.

Although the peak modal gain values presented in Figure 6.5 are similar, they were obtained for significantly different pump powers. The lowest excitation was achieved for the sample LD410, which required optical pumping from 0.03 MW/cm^2 to 0.4 MW/cm^2. In contrast, the samples LD370, LD390 and LD430 required an order of magnitude higher pumping rates, i.e. between 0.4 MW/cm^2 and 2.2 MW/cm^2.

It is necessary to draw the reader's attention to the low energy tails of each gain curve. They are usually assumed to yield a rough estimation of a below-bandgap internal propagation losses. The values of internal losses determined this way vary from 60 cm^{-1} (LD370) through 25 cm^{-1} (LD390, LD410) down to 12 cm^{-1} (LD430). Considerably large internal losses determined for LD370 originate probably from the fact, that for such a short emission wavelength waveguiding and cladding layers consist of AlGaN, which is strongly lattice mismatched to GaN substrate. Formation of cracks can explain the origin of excess propagation losses sensible to the mode guided by the structure. The differences between the corresponding values determined for other samples need to be considered as similar due to significant experimental error and cannot be undoubtedly related to a degree of In content.

The peak modal gain dependance on carrier concentration agrees well with a logarithmic expression for gain including the differential gain parameter g_0 and the transparency carrier concentration N_{tr}:

$$g = g_0 \, ln \frac{N + N_s}{N_{tr} + N_s} \tag{6.2.1}$$

N_s is a fitting parameter allowing for the linearization of the logarithmic dependance. The fitting curves together with experimental data are depicted in Figure 6.6(a).

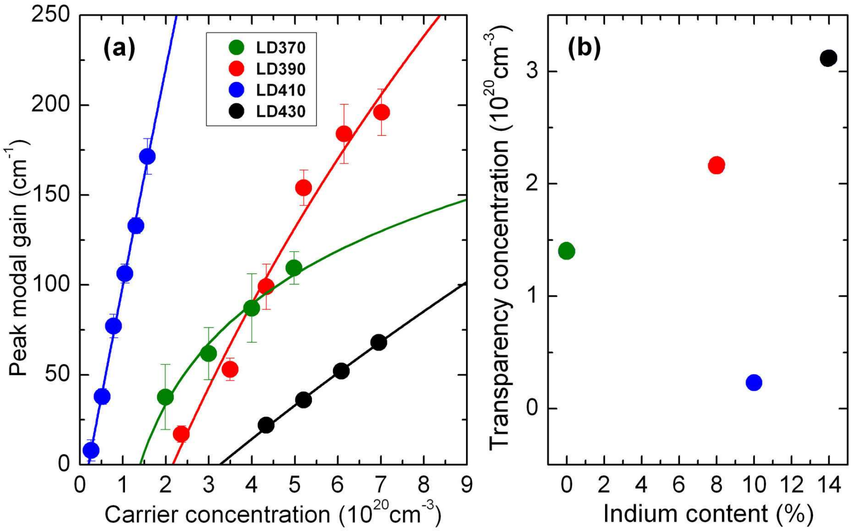

Figure 6.6: Peak modal gain versus carrier concentration determined for samples LD370, LD390, LD410, LD430 (a); Dependance of transparency level on indium composition in the active region.

Figure 6.6(b) consist of the data concerning transparency levels. One could assume that the transparency level increases with a rising In content reflecting the deterioration of a structural quality characteristic for a ternary alloy, if it were not for the fact that LD410 is subject to an order of magnitude decrease in transparency. Such a huge reduction can be attributed: primarily to an optimum carrier localization effect responsible for the increased radiative recombination rate, secondary to the qualitative leap in a growth technology allowing for the improved In incorporation at a given temperature and growth rate.

It is also worth noticing that the peak gain dependance on the carrier concentration presented in Figure 6.6(a) takes a more linearized form as the indium content in QWs increases. The more linear dependance, the larger linearization parameter N_s, which increases

Sample Name	QW In content (%)	α_i (cm^{-1})	N_{tr} ($10^{20}cm^{-3}$)	N_s ($10^{20}cm^{-3}$)
LD370	0	60	1.4	-0.51
LD390	8	20	2.16	6.11
LD410	10	20	0.23	6.75
LD430	14	12	3.13	232.51

Table 6.2: Rough estimation of internal propagation losses and the values of the fitting parameters used in Equation 6.2.1.

rapidly by two orders of magnitude for sample LD430.

Ref. [43] suggests that this relation is influenced by the degree of quantization, which is more linear for bulk than QW-based systems. However, the data was collected for GaAs-based materials, which lack the influence of strong spontaneous and piezoelectric fields. In our case the tendency is somehow opposite and scales not only with the localization effects induced by the raising degree of indium fluctuations as expected for samples with pronounced indium content, but also with the increased amount of the internal piezoelectric fields responsible for the gradual reduction of electron and hole wavefunction overlap (as presented in Figure 3.1). The rapid increase of N_s is a result of the conversion from a logarithm-like to linear dependance as observed for sample LD430 and can be attributed to the abrupt onset of a strong localization induced by zero-dimensional nanoobjects formed in the plane of QWs of LD430. This effect is however questionable and needs a further insight.

The values of all fitting parameters and internal propagation losses determined from the above-mentioned experiment are summed up in Table 6.2.

Let us now proceed with the analysis of the differential gain evaluated for each sample. The modal gain values determined from direct measurement were recalculated into material gain using optical confinement from Table 6.1. Differential gain was evaluated taking into account a correction for different QW width L_z by factor $L_z/45$ Å as presented in Ref. [43].

For the samples LD390 and LD410 the differential gain is the largest and varies between $1.8-1.4\times10^{-17}$ cm^2. Bandprofile fluctuations induced by indium clustering localize carriers keeping them away from non-radiative recombination sites. The excited carrier population can be established relatively easy leading to a rapid increase of the peak optical gain.

On the other hand, values of the differential gain estimated for samples LD370 and

LD430 are reduced considerably down to about 0.6×10^{-17} cm^2. For LD430 the QW indium content increases up to 14%. The deeper bandtail states and hence the increased density of the available transition state pairs counteract the effect of the material excitation. More severe separation of electrons and holes can additionally deteriorate the radiative recombination rate. The similar effect of reduction of quasi-Fermi level separation can be supposed for LD370, where the active region consist of a sequence of pure GaN QWs. The lack of localization effects results in an increase of the probability of nonradiative recombination followed by the reduction of the excited carrier population, which cannot usefully contribute to the optical gain.

As suggested by our analysis, lasing action can be most easily achieved for LD390 and LD410. Due to severely low differential gain, threshold condition for LD370 and LD430 could be met at the excited carrier concentration exceeding any reasonable value (even by an order of magnitude according to our estimations) achievable in a real device. Consequently, additional research needs to be carried out in order to optimize the growth conditions and to improve the quality of the active region of the structures similar to LD370 and LD430 emitting in the corresponding spectral range.

6.2.2 Investigation of optical gain in MBE-grown laser structures

In order to find out, whether PAMBE is a viable growth technique in nitride optoelectronics, we decided to compare the optical properties of the laser structures deposited on a Ga-polarity side of (0001) oriented GaN substrate by two alternative techniques. The fundamental differences characterizing both techniques result in some dissimilarities between the investigated laser structures. In order to take advantage of the low temperature growth in PAMBE reactor, the epitaxial process needs to take place in the presence of additional group-III-metal-rich conditions. In our case a species of choice is indium, which forms a thin, precisely controlled, dynamic layer on the substrate surface. Under such conditions a barrier height for nitrogen diffusion is significantly lowered and step-flow growth mode is achievable at temperatures as low as 600℃ . However, as In atoms are incorporated into namely every epitaxial layer during a growth process, the optimum composition of the entire laser stack differs in case of the PAMBE from the one achieved in MOCVD reactor.

As a consequence, the comparative experimental study concerning the details of the optical gain was carried out on two laser structures with slightly different active regions and waveguiding layers reflecting the presence of In surfactant. In order to perform a comparison, the properties of the previously analyzed LD410MOCVD will be related to PAMBE-grown LD405MBE with a peak emission designated by the sample name. The close details of each sample are given in Appendix A. We will focus only on the design of the active region. To recall the information included in Table6.1, we mention here that the sample LD410MOCVD consisted of a sequence of five 4.5 nm thick $In_{0.1}Ga_{0.9}N$ QWs and 7-nm-thick $In_{0.02}Ga_0.98N$:Si barriers followed by 20 nm of $Al_{0.24}Ga_{0.76}N$ EBL. On the other hand, LD405MBE's active region was formed by a sequence of five 3-nm-thick $In_{0.1}Ga_{0.9}N$ QWs and 7 nm thick $In_0.02Ga_{0.98}N$:Si QBs capped with 14 nm of $In_{0.02}Al_{0.16}Ga_{0.82}N$:Mg EBL.

Each growth technique boasts its advantages and fabrication of two identical laser stacks remains extremely difficult. That is why we decided to compare the optical properties of the two optimized laser designs characterized by the best operating parameters achieved so far by these alternative techniques. Although the net modal gain derived in our photoexcitation experiment depends on the amount of the propagation losses, it is mainly influenced by the properties of the active region. In addition, internal propagation losses can be roughly deduced from the low energy tail of a gain curve, allowing for an easy estimation. Other important parameters derived from the experimental data, such as differential gain, saturation length and activation energies for nonradiative recombination, remain solely active-material-dependent and do not rely on details of a waveguide. Hence, we tend to assume that the conclusions we come to are valid enough to make a rough estimation of major differences in optical properties of the analyzed samples grown alternatively by MOCVD and PAMBE.

The experimentally determined modal gain curves are depicted in Figure 6.7. Both samples emitted an optical signal of a comparable intensity. They were excited by optical power ranging from 0.03 MW/cm^2 up to 0.4 MW/cm^2. The room temperature carrier lifetime of 0.6 ns [118] and the internal quantum efficiency of 60% [125] were used to estimate the excited carrier population.

Peak modal gain plotted in Figure 6.8 was fitted with expression 6.2.1. The fitting procedure revealed that the transparency levels determined for the sheet carrier density were slightly higher for the MOCVD-grown structure, i.e. 5.4×10^{13} cm^{-2} versus 4.3×10^{13} cm^{-2}

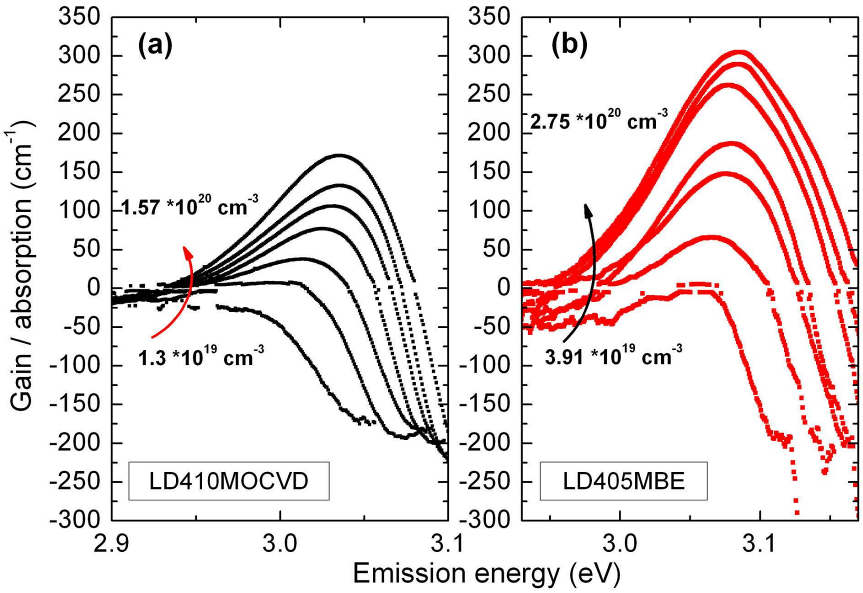

Figure 6.7: Modal gain curves determined for LD410MOCVD (a) and LD405MBE (b). Lower and upper limits for estimated carrier concentration are also presented.

for LD410MOCVD and LD405MBE, respectively.

One might expect from Figure 6.8 that the differential gain is considerably larger for the MBE-grown structure. However, when the data is corrected for the differences in QW width by factor $L_z/45$ Å, the differential gain is roughly the same for both samples (see Figure 6.8). It is necessary to be aware that the method gives only an approximate estimation. The comparison of inhomogeneous broadening of the gain curves indicates a favorable features of LD405MBE. Full width at half maximum (FWHM) for a given peak gain is larger for MOCVD- than MBE-grown sample (see Figure 6.9(b). Encouraged by this observation, we performed a temperature dependent photoluminescence experiment. Activation energy E_{act} determined from a theoretical fit to the experimental data expressed by [126]:

$$I = I_0[1 + \frac{\rho_{nr}}{\rho_r} exp\,(-\frac{E_a}{k_B T})]^{-1} \tag{6.2.2}$$

yielded value of 41 meV and 22 meV for MOCVD- and MBE-grown structure, respectively. Also the ratio of nonradiative to radiative recombination probability $\frac{\rho_{nr}}{\rho_r}$ is five times larger for MOCVD-grown sample, posing a question concerning its structural quality. The data is presented in Figure 6.9.

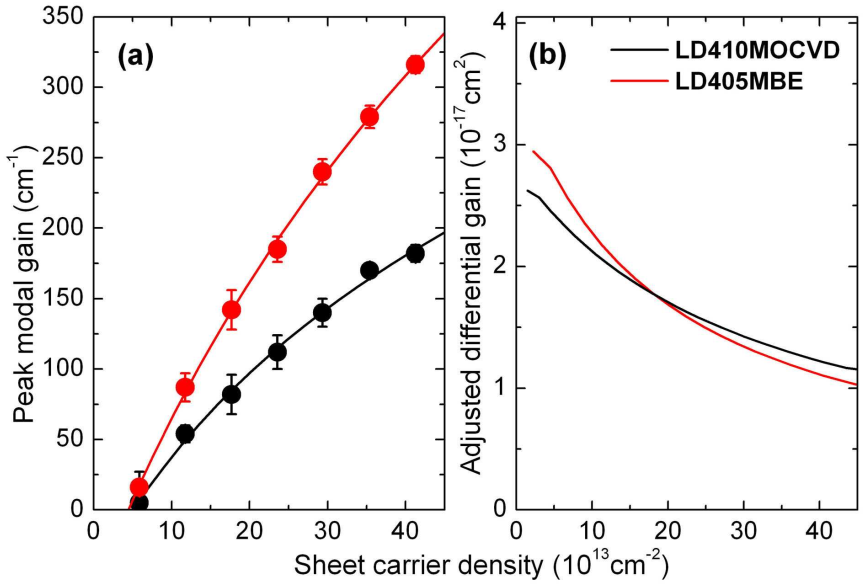

Figure 6.8: Peak modal gain dependance on excited carrier density (a) and the differential gain estimated for samples LD410MOCVD and LD405MBE.

Despite the same QW In content the research reveals higher In segregation. Larger localization does not suppress efficiently nonradiative recombination suggesting a lower structural quality of LD410MOCVD. Influence of point defects and threading dislocations can be significant in this case. In addition, for the narrower bandtail state distribution revealed for LD405MBE (as reflected by smaller inhomogeneous broadening of the gain curves) the population inversion can be reached at smaller excitation levels leading to reduced threshold current values expected for real laser devices.

Let us finally focus on the saturation behavior of the analyzed structures. Gain saturation needs to be taken into account at high photon densities as a result of a spatial carrier distribution along the resonant cavity. We focus on the saturation phenomena close to the gain maximum, which is the optimum working range for a real laser device. It is generally assumed that the saturation starts to play a significant role when the stimulated recombination rate becomes comparable with the rates of nonradiative and spontaneous recombination [21]. Following this approach we can try to asses the impact that the nonradiative recombination induces on the device's performance.

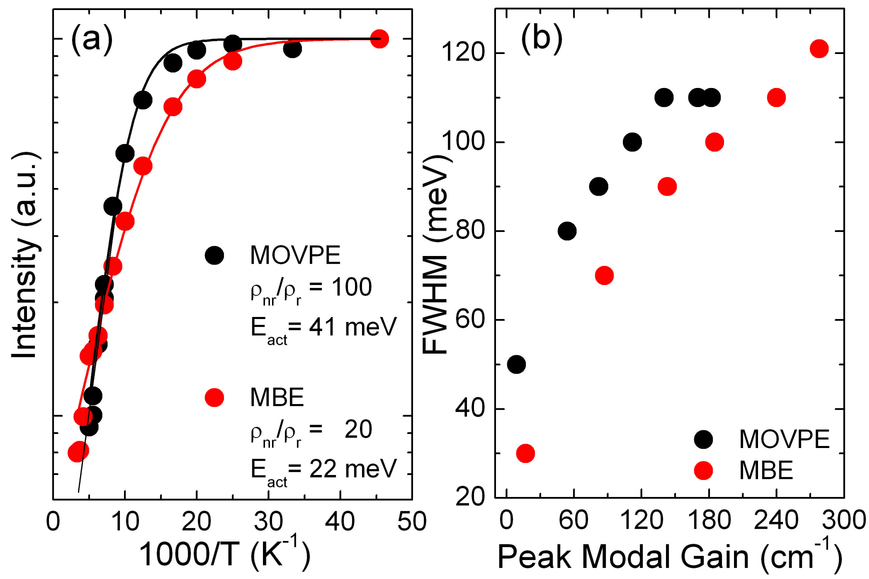

Figure 6.9: Arrhenius plot of temperature dependance of PL (a) and FWHM of the gain curves (b) estimated for samples LD410MOCVD and LD405MBE.

Figure 6.10(a) contains information on the saturation length dependance on the excited carrier concentration. For the lowest excitation level L_{sat} of 350 μm determined for LD410MOCVD is considerably longer than the corresponding value of 250 μm evaluated for LD405MBE. The superior crystal quality resulting in reduced nonradiative recombination becomes evident. Increased excitation accelerates the depletion of the electron-hole plasma by stimulated photons. Shorter L_{sat} determined for LD405MBE cannot be the result of the enhanced spectral hole burning, because of the lower optical confinement as calculated by LASTIP (see Table 6.1). L_{sat} decreases considerably approaching 180 μm at the highest excitation. This value tends to be common for both samples and can be attributed to a complete saturation of nonradiative recombination sites.

The argumentation derived from the analysis of L_{sat} leads to conclusions consisted with the data presented in Figure 6.8, where the transparency levels differ slightly in favor of MBE-grown structure. Since transparency does not depend on the geometry of the active region and is solely material dependent, it would be reasonable to additionally support the assumption of the improved structural quality of LD405MBE.

From the practical point of view, the most suitable quantity for describing an optical

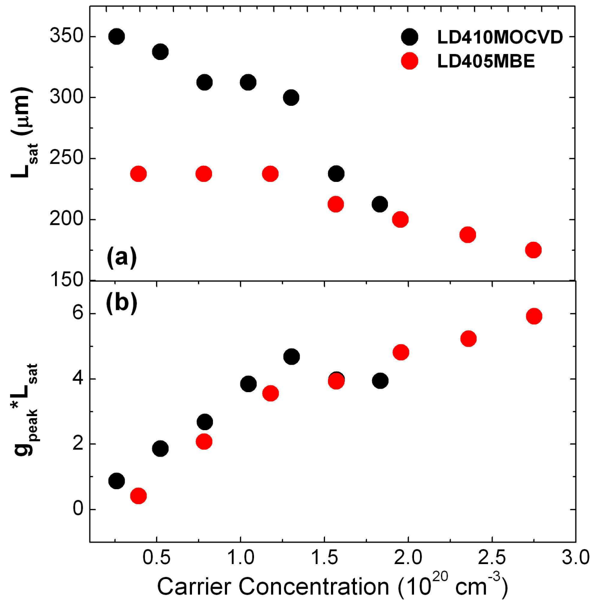

Figure 6.10: Dependence of the saturation length (a) and the product of the peak gain versus saturation length (b) on the injected carrier concentration determined for samples LD410MOCVD and LD405MBE.

amplifier is the product of the unsaturated modal gain and L_{sat}, which is almost the same for both structures increasing from 1 to 6 with the rising excitation power (see Figure 6.10(b)). Excess nonradiative recombination as well as too short saturation length, being a result of the spectral hole burning, can have an equally negative impact on the device's performance. Thus it is necessary to compromise reasonably between these two parameters. However, what can be concluded unambiguously, is that the narrower spectral width of the gain curves determined for LD405MBE leaves much space for the potential improvement of the differential gain leading to the reduced threshold and the faster frequency response. As suggested by this research, there are future prospects for applicability of PAMBE in the field of nitride-oriented technology.

Chapter 7

Heat generation and thermal management

GaN-based LDs suffer from the excess heat generation occurring because of a large amount of electrical power that needs to be supplied in order to reach lasing. Despite the robustness of III-nitrides, a critical consequences that a surplus Joule heat imposes on stability and durability of the device's active region cannot be ignored. It not only shifts the operating current towards higher values, as described by phenomenological characteristic parameter T_0 introduced in Chapter 5, but also reduces considerably the device's lifetime due to a thermally assisted defect formation [87].

The reasons for such a behavior can be manyfold. On one hand they originate in strictly material-dependent features such as a large density of available states which results in elevated injection levels needed to achieve a population inversion. Additionally high activation energy of Mg acceptors and large hole effective mass induced by a significant valence band curvature in E-k space inhibits charge transport through p-type layers. On the other hand the negative impact of these unfavorable material properties is additionally magnified by technological obstacles linked with limited solubility of Mg acceptors and problems with obtaining good quality metal contacts to p-type GaN [127]. As a result, most of the heat generated within a device comes from p-type epitaxial layers and the p-type Ti/Au contact electrode having inferior conductivity when compared to their n-type counterparts.

The slope efficiencies range from 0.4 W/A to 1 W/A. Due to a thermally induced enhancement of the leakage current, they are apparently larger for pulsed than CW-operated devices. Thus there is a reason to believe that a large thermal resistance of the entire laser package could be the one but not the only cause responsible for deterioration of the slope efficiency in case of high-power LDs. Some peculiar features of the active region itself such as a poor quality of the EBL or inhomogeneous carrier injection resulting in enhanced QW absorption can also possibly shift a laser threshold and impede the device's performance.

As the major role of this chapter one can identify an attempt to define the critical regions with the largest thermal resistivity (either within a laser chip, diamond or copper submount) and to optimize thermal properties of the laser stack and mounting.

7.0.3 Infrared thermography

The most commonly used experimental methods oriented on determination of the temperature of the active region are: comparison of the current-voltage curves for pulsed and CW operation or observation a thermally induced spectral shift of optical transition energy. They have however the number of weaknesses. The former is limited to small current values due to difficulties in maintaining a step-like shape of nanosecond long current pulses and a possible self-heating induced by high electrical power stored within a single pulse even under a low duty cycle working regime. On the other hand, the latter is subject to a thermally induced mode hopping. Both approaches give only the information about the temperature of the junction.

Practical requirements set by LD's working regime define the most interesting excitation range as lying above laser threshold, which in case of the analyzed devices demanded working with relatively current values ranging between 100 mA and 500 mA. Thus the most convenient way of detection the spacial temperature gradient across subsequent elements of different laser packages was the usage of a thermal infrared (IR) imaging system. The experimental analysis was carried out in cooperation with M. Bednarek and prof. J. Rybinski from the Main School of Fire Service in Warsaw.

The experimental procedure employed high-speed, high-resolution imaging camera equipped with a cooled InSb photodetector and Ge-based microscopic lens transmitting between 3-5 μm. Temporal evolution of every temperature map was recorded with 50 Hz frequency. The operational stability of devices working in CW regime was assessed during 20 s current pulses. Thermal maps were collected for two alternative packaging systems described below.

Because a resolution of the imaging system was limited to about 7 μm, the IR thermal maps were unable to distinguish the details of the epitaxial layers. It is however reasonable to assume, because of a close vicinity, that all the regions which generate heat, i.e. quantum wells, p-type epitaxial layers and p-type contact electrode, have roughly the same temperature which would be unresolvable within the dynamic sensitivity offered by the IR imaging system. Since the analyzed devices were chosen in such a way that they did not reach CW lasing in the range of the electrical power applied by us, additional effects of the excess mirror heating induced by the absorption of high photon density were neglected.

7.1 Thermal properties of different packaging schemes

At the current stage of the device development achieved at Institute of High Pressure Physics, the amount of electrical power that needs to be applied to LD's terminals and then dissipated varies between 2.5-8 W, depending on internal structure of the device and its stripe geometry. For this reason two alternative mounting systems are utilized: a commonly used laser package with a diameter of 5.6 mm and a package based on a concept in which a laser device is sandwiched between two copper blocks. The former is mainly used for the pulse excitation, whilst the latter plays the major role in case of CW-operated devices. Schematic pictures of both mounting schemes are presented in Figure 7.1.

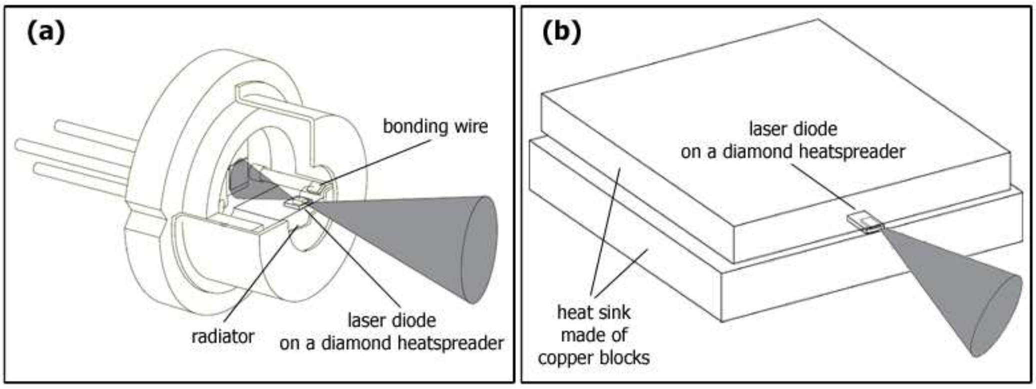

Figure 7.1: Commercially available can-like laser package with a diameter of 5.6 mm (a) and the original packaging concept developed at Institute of High Pressure Physics based on two copper blocks serving as a heat sink (b).

In order to improve the thermal conductance, the standard packaging employs a diamond heatspreader as a laser submount, which is then attached to a copper heatsink by a thin film of AuSn eutectic alloy. The temperature of the package is stabilized by a thermoelectric cooler at 22℃ during CW working regime. However, when input electrical power density exceeds 80 kW/cm^2, the thermal roll-off of the L-I curve appears. It turns out that even when a Peltier cooler is used, heat dissipation seems to be somehow insufficient. As a result, the maximum optical power out of both facets achievable for CW-operated LDs having the ridge width of 20 μm is 270 mW [128]. At the same time the optical power density at laser facets reaches only a few MW/cm^2, a value that remains well below the critical optical power density of about 50 MW/cm^2 that causes a so called *catastrophic optical mirror damage* (COMD).

Thus temperature effects impose serious limitations on a potential device performance. However one can reasonably expect that if the electrical resistance of p-type layers is reduced and the thermal management improved considerably, the output optical power achievable for CW lasers will be successfully increased.

As revealed by the measurements, at the highest driving current of 420 mA, the temperature of the active region and all heat-generating p-type layers of the device mounted in a p-down configuration using a standard 5.6 mm laser package reached almost 85℃ . Figure 7.2(a) depicts the entire thermal map taken from the direction defined by the laser's output facet. The picture shows clearly that the diamond heatspreader efficiently dissipates heat generated at the bottom side of a laser chip assuring almost a vertical-like heat flow. As confirmed by Figure 7.2(b), which contains a temperature distribution along AD line from Figure 7.2(a), a diamond heatsink is responsible for about 20℃ temperature drop on a distance of about 10 μm. However, Figures 7.2(a) and 7.2(b) clearly reveal that there is a slight heat generating effect at the interface between the diamond heatspreader and the copper submount. These two elements are sealed together by $Au_{0.8}Sn_{0.2}$ eutectic solder, which is also a current conducting medium. The effect of the current flow is responsible for a local 5℃ temperature increase.

In order to emphasize the radial heat distribution within the laser device towards the bulk GaN substrate, the area of the facet is presented in a different temperature scale in Figure 7.2(c). The temperature gradient towards air is not as steep as in the opposite direction. Consequently, a considerable fraction of it needs to be transported back through the

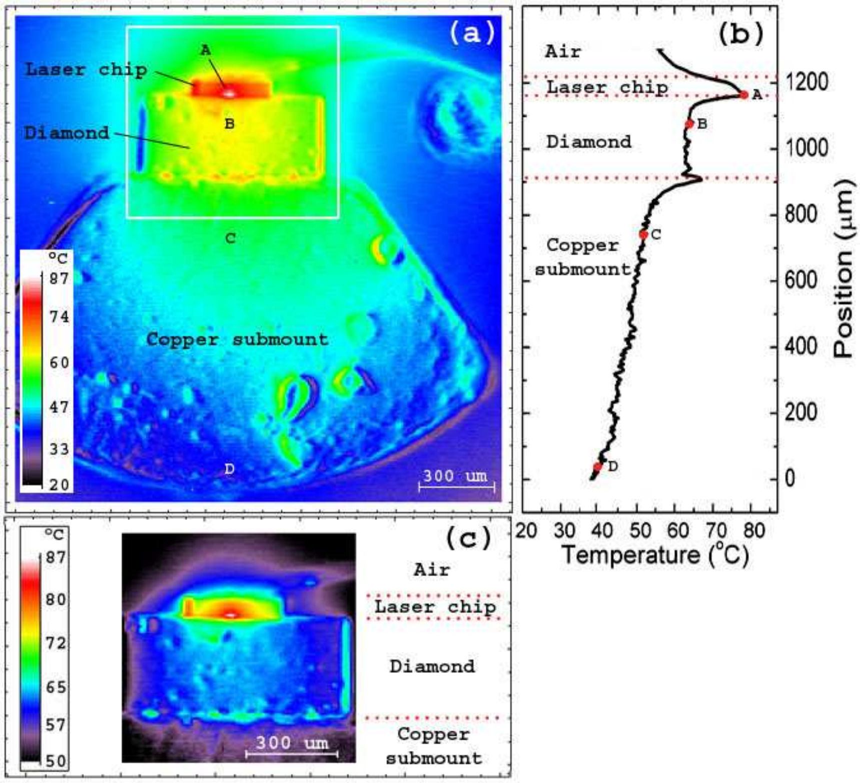

Figure 7.2: Temperature distribution on a laser mounting system using a standard 5.6 mm package (a); temperature evolution along AD line (b); magnified view of the thermal map emphasizing radial heat distribution on a laser facet (c).

entire active region towards the diamond heatspreader increasing the overall temperature within the QWs.

The chosen way of eliminating this effect was the usage of two copper blocks that attached on both sides to the laser and its diamond submount (Figure 7.1(b)) assure much better thermal management and allow for successful CW operation. IR thermography was chosen to unveil the temperature distribution in this alternative mounting system. Figure 7.3(a-c), contain the relevant data presented in a similar form as previously. The temperature map collected at the same driving current of 420 mA as for 5.6 mm package is presented in the same temperature scale in Figure 7.3(a). What is the most important, the temperature of the active region was successfully reduced from initial 85℃ down to as low as 45℃. It was passible because of the excellent heat conductivity of the upper copper block

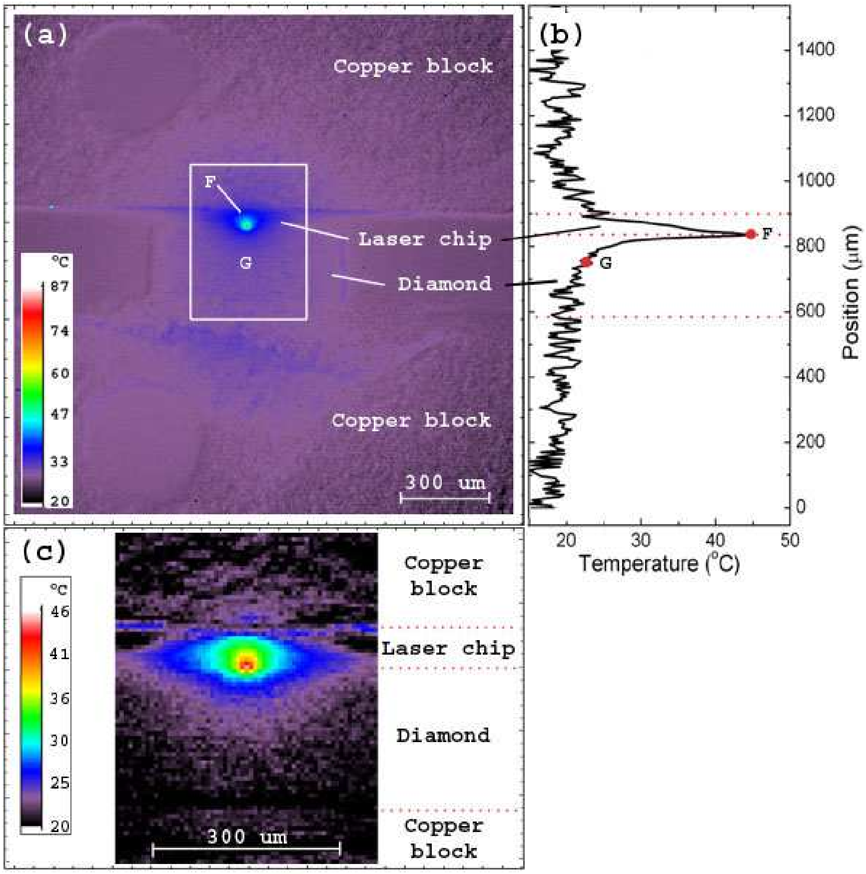

Figure 7.3: Temperature distribution on a Cu-sandwiched laser package (a); temperature evolution along FG line (b); magnified view of the thermal map on the laser facet using different temperature scale (c)

attached to the bulk GaN substrate from above using $Au_{0.8}Sn_{0.2}$ eutectic alloy. In the case of the current laser mounting system, the diamond heatspreader assures even greater (about 25℃) temperature drop, since it is supported by additional copper block from the opposite side. The temperature drop away from the active region in the opposite directions along FG line (see Figure 7.3(b)) is almost the same and rapidly approaches the temperature of the thermoelectric cooler. The heat accumulation at the diamond-copper interface is also eliminated as a consequence of the overall reduction of thermal resistance.

The feature that also nicely summarizes a better thermal management achieved by the Cu-block-based laser mount is the temporal evolution of the active region temperature during a 20-s-long driving pulse. As evidenced in Figure 7.4, temperature measured close

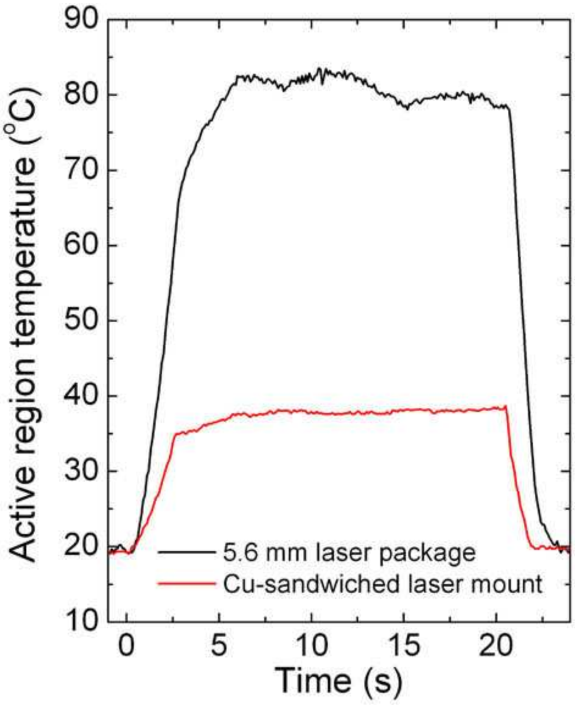

Figure 7.4: Temporal evolution of the junction temperature during 20 s long driving current pulses.

to the active region (at the points A and F in Figures 7.2 and 7.3, respectively) increases considerably slower in case of the Cu-sandwiched LD, remains more stable during a driving pulse and drops rapidly after the end of the excitation period.

7.1.1 Thermal resistance

Prior to collection of the temperature distribution maps performed by IR imaging, it was necessary to perform a calibration taking into account differences in thermal emissivity of each material. Since the obtained data depend on this procedure, a comparison with an alternative method was necessary in order to confirm the results. The analysis of the low-current-versus-voltage characteristics collected during a pulse and CW operation was chosen as a tool to estimate the validity of the IR thermography.

Practical realization of the measurement revealed that the method offers reasonable sensitivity. The analysis was carried out for LDs mounted in three different ways:

- p-up without a diamond heatspreader in a 5.6 mm package

- p-down on a diamond heatspreader using a 5.6 mm package
- p-down on a diamond heatspreader sandwiched between two Cu blocks

Pulsed I-V curves were collected at low duty cycle of 0.03% to satisfy a trade-off between the lack of self-heating and a step-like pulse shape. Thus it was assumed that a junction temperature was defined solely by the temperature of the external heater. Changes of temperature with a step of 2-3℃ consequently accounted for a well resolved differences, which were then compared with I-V curves recorded for a CW-operated devices stabilized at 18℃ (see Figure 7.5). Intersections between curves recorded for pulse and CW operation modes were used to estimate the junction temperature for a given current in the CW working regime. As depicted in Figure 7.6(a), the values of the active region temperature

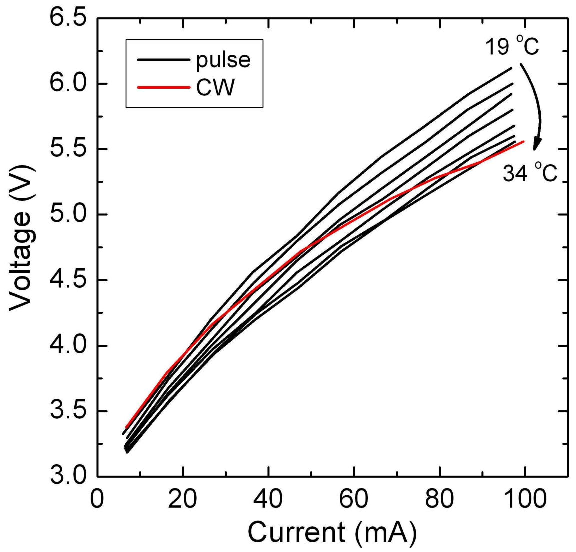

Figure 7.5: I-V curves collected for a device mounted p-down on a diamond heatspreader using 5.6 mm laser package in a CW (red line) and pulse (black line) working regime at temperatures ranging from 19℃ to 34℃.

determined using electrical analysis in the low-current range match the values obtained from IR thermography for the above-threshold injection. Based on this data derived for three different mounting schemes, it was possible to asses the amount of their thermal resistance. Figure 7.6(b) reveals that the initial thermal resistance of 80 K/W can be efficiently reduced when the original p-up mounting scheme without a diamond heatspreader is replaced by p-down laser mount using diamond. However, the reduced value of 32 K/W is not enough

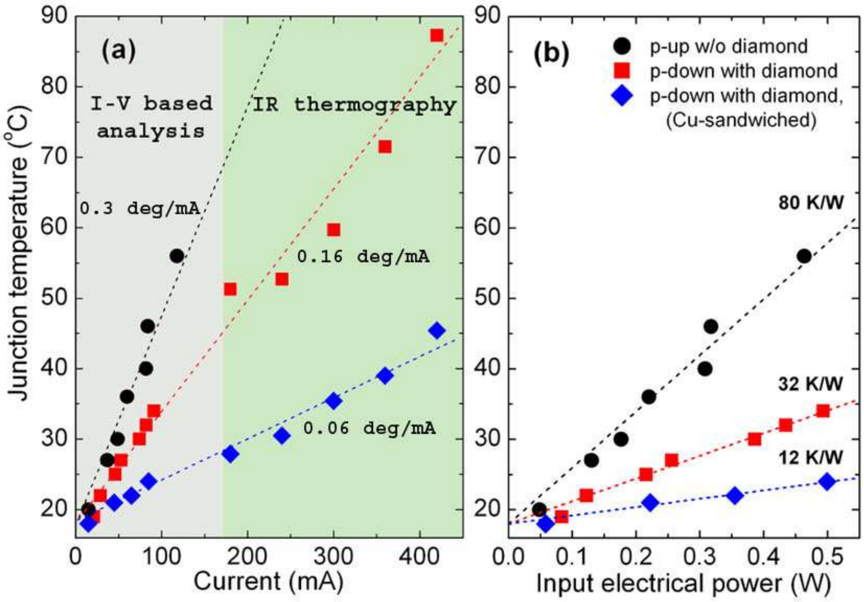

Figure 7.6: (a) Junction temperature as a function different operating currents determined by comparison of I-V characteristics collected in CW and pulsed working regime (grey background) and by IR thermography for above-threshold injection (green background); (b) Junction temperature versus input electrical power used to determine thermal resistance for three different mounting schemes.

to achieve CW lasing for a reasonable value of the injection current even when the laser mount is stabilized at 18℃. Finally, when a laser mount employs two copper blocks, the thermal resistance is reduced down to 12 K/W and CW operation characterized by a limited degradation rate can be achieved. The latter value is significantly lower when compared to the values reported in literature for alternative laser packaging schemes [129, 87].

Since practical applications set requirements that need to be met not only in terms of the minimum thermal resistance but also the optimum convenience, superior thermal properties of the double Cu block based mounting scheme cannot be treated of as a decisive applicability criterion. The device optimization should rather follow the path of lowering the LD's threshold and improving its thermal stability expressed by the increased of T_0. Reduction of the thermally induced electron leakage by a more sophisticated design of the EBL (see Refs [130, 131]) would also yield a significant contribution.

7.1.2 Availability of lasing in CW working regime

It is possible to estimate roughly the expected availability of CW lasing for a given device by means of a set of fundamental parameters introduced so far. These quantites are used to describe the physical properties of the device itself, i.e. the characteristic temperature T_0 and series resistance R_s as well as the features of a mounting scheme expressed by its thermal resistance R_{th}.

The maximum output power coupled into the lasing mode depend implicitly on a junction temperature T_j for a given excitation current I and can be assessed by the following relation [66]:

$$T_j = T_a + R_{th}(IV_j + I^2 R_s), \tag{7.1.1}$$

where T_a stands for the ambient temperature and V_j for the junction voltage. The junction temperature defines subsequently the value of the threshold current [66]:

$$I_{th}(T_j) = I_{th0}(T_a) exp\,[\frac{T_j - T_a}{T_0}] \tag{7.1.2}$$

In this relation I_{th0} marks the LDs threshold at ambient temperature without the heating effect induced by the input electrical power. Thus we can finally recognize the fact that the amount of the optical power at laser output achieved for a given excitation current I depends on the position of the lasing threshold I_{th}, which in turn depends strongly on the junction temperature T_j [66]:

$$P = F\eta_d V_j(I - I_{th}(T_j)) \tag{7.1.3}$$

Here F is the fraction of light coupled out of a given facet and η_d defines the external differential quantum efficiency.

Based on the relations introduced above and using a typical set of the device parameters such as: series resistance $R_s = 10\,\Omega$, thermal resistance of the package $R_{th} = 32\,\mathrm{K/W}$ as determined for a device mounted in a flipped-chip configuration in a 5.6 mm standard laser package, it was possible to trace the behavior of the L-I characteristics. The assumed slope efficiency was 0.3 W/A. The only parameter that changed was the characteristic temperature T_0. The resulting L-I curves are presented in Figure 7.7

As shown in Figure 7.7, thermal stability of the device represented by T_0 parameter is of a critical significance for an efficient CW lasing. Any reduction in T_0 not only shifts the

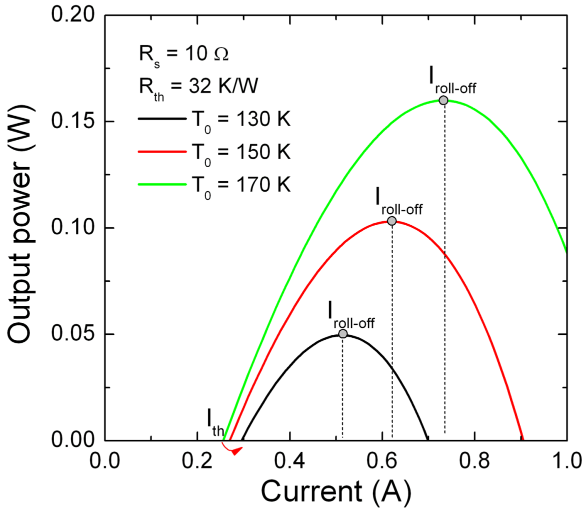

Figure 7.7: Expected changes of L-I curves determined for three different values of the parameter T_0.

threshold current towards higher values, but also reduces the excitation level, for which a thermal roll-off (designated as $I_{roll-off}$) appears. Once I_{th} and $I_{roll-off}$ meat at the same point, the lasing action cannot be reached at all as a result of a severe dependance of I_{th} on temperature and insufficient heat dissipation.

In order to estimate the practical limits, which allow for the stable CW lasing, it is useful to define a ratio of the roll-off current to the threshold current ($I_{roll-off}/I_{th}$). This quantity depends not only on T_0 of a given laser, but also on its series resistance R_s and thermal resistance R_{th} of a packaging scheme of choice. The results of our rough estimations are presented in Figure 7.8(a-c). The ratio $I_{roll-off}/I_{th}$ was divided into the following regions:

- $I_{roll-off}/I_{th} < 1$ – lasing action is unavailable or at the edge of stability - prospects for practical applications ruled out (black region)
- $1 < I_{roll-off}/I_{th} < 2$ – thermal roll-off appears relatively close to the threshold - possibility of practical usage is questionable (grey region)
- $I_{roll-off}/I_{th} > 2$ – thermal roll-off significantly above threshold - practical constrains satisfied (white region)

The data was calculated for three packaging schemes discussed above and characterized

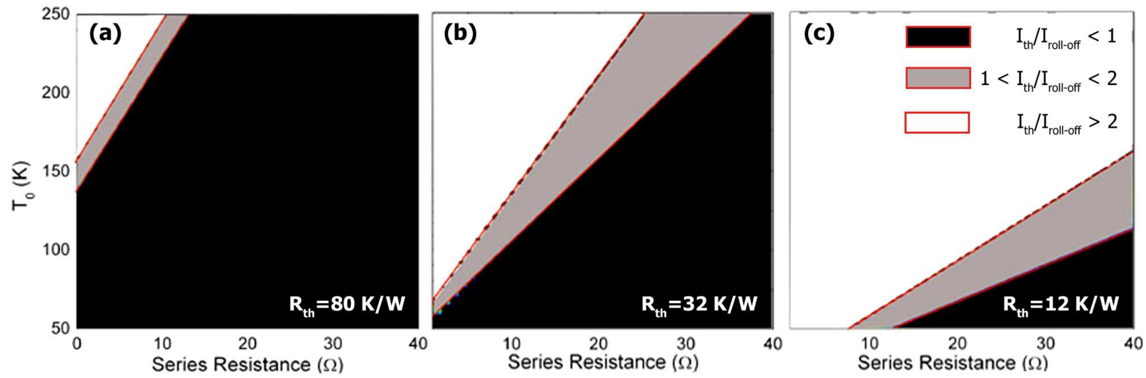

Figure 7.8: Availability of the lasing action in CW regime presented in the form of $I_{roll-off}/I_{th}$ ratio estimated for three different packaging schemes characterized by their characteristic thermal resistance R_{th}.

by different values of thermal resistance, i.e.:

- 80 K/W (p-up without a diamond heatspreader mounted in the 5.6 mm package)
- 32 K/W (p-down on a diamond heatspreader mounted in the 5.6 mm package – Figure 7.1(a))
- 12 K/W (p-down on a diamond heatspreader sandwiched between two copper blocks – Figure 7.1(b))

The analysis suggests that any laser packaging characterized by the excess thermal resistance R_{th} (Figure 7.8(a)) imposes considerable limitations on device's parameters. Weak heat dissipation needs to be compensated by the reduction of the series resistance R_s and improved thermal stability reflected by T_0 of about 200 K and higher. Any reduction of R_{th} for a given laser packaging expands the range of acceptable device parameters. In the lowest limit achieved by us, R_{th} was reduced down to 12 K/W (Figure 7.8(c)) allowing for the efficient CW lasing even in case of devices with T_0 only slightly above 100 K. The assumption is valid, providing that the series resistance R_s remains close to 10 Ω, as assumed for our devices.

However, for practical reasons it is much more convenient to use the standard 5.6 mm laser package in combination with a diamond heatspreader. In case of this mounting scheme, besides its portability, a proper device handling is not as critical and a given LD is not subject to an easy mechanical damage done accidentally by an unexperienced user. For this mounting approach the achievement of CW lasing requires the thermal stability characterized by T_0 values exceeding 150 K, as depicted in Figure 7.8(b). Even higher values have been achieved so far. Unfortunately, a considerable fraction of such devices were accompanied by the accelerated degradation rate, which needs to be reduced prior to looking for possible applications.

Chapter 8

Properties of the optical waveguide

Optimization of the waveguiding properties and a structural quality of a dielectric waveguide helps to reduce the input electrical power necessary to reach a desired optical output. Consequently, a prolonged device's lifetime can be reached, opening the chances for commercial applications [132]. However, optical data storage systems such as digital versatile discs and optical hard drives as well as high resolution printers impose many requirements on the device performance. On one hand, there are important design issues dealing with problems of uniform and time-independent injected carrier distribution, possibly high recombination efficiency and effective carrier confinement in the active region. They transform directly to high optical output power, low relative intensity noise and temperature insensitivity of laser threshold. On the other hand, the easiest way to achieve a tight and reproducible focus spot is to deal only with the fundamental optical mode of the resonant cavity modified in a way, that assures an increased spatial and temporal stability. For the above-mentioned reasons, careful design of the optical properties of waveguiding layers is so important.

8.1 Optical propagation loss

Considering any given semiconductor laser, one can distinguish between two possible optical loss mechanisms: mirror loss and internal propagation loss. Both of them influence operational parameters of each laser diode. They have considerable impact on a lasing threshold as well as a slope efficiency. Although the former term can be usefully optimized by deposition of facet coatings in order to meet a desired working regime, the latter one definitely needs to be eliminated, as it introduces excess optical mode propagation loss - a solely negative phenomena. Formally, the internal propagation loss term can be given by the following formula:

$$\alpha_i = \Gamma\, \alpha_{f-c} + \alpha_{sc} + \alpha_{sub}, \qquad (8.1.1)$$

and interpreted as a sum of the free-carrier absorption encountered throughout all layers of the laser stack α_{f-c}, scattering loss due to the roughness of heterointerfaces α_{sc} and a mode leakage beyond the cladding layers (mainly into the substrate) α_{sub}. The total amount of the internal optical propagation loss can be reduced considerably by a design of transverse and lateral electromagnetic field profile. The analysis is usually carried out with regard to a better optical confinement [133, 134, 135], reduced leakage out of the waveguide [136, 137] and the cavity mode shift away from the most absorbing regions, i.e. highly Mg-doped p-type layers, where relatively deep Mg acceptor levels are responsible for considerable absorption below a bandgap of the undoped GaN [138]. These goals can be achieved by improved design of a refractive index profile and by an appropriate etch depth of the mesa stripe.

Although highly absorptive Mg-doped p-type layers are believed to be the major source of the optical cavity loss [139], the mode leakage imposes serious limitations on a laser performance as well. If the difference between real parts of refractive indices is small and the cladding layers are not thick enough, the discrete optical modes coupled to the waveguide have an evanescent field components that spread outside the core region. As a result, the amount of energy stored in the evanescent tail can be significant.

Laser diodes based on nitrides consist of AlGaN-containing cladding regions, which are considerably lattice-mismatched to the bulk GaN substrate. Hence a growth of sufficiently thick AlGaN layers can be severely impeded by cracking. Unless the growth is not optimized in order to allow for the growth of thick AlGaN films, devices suffer from considerable mode leakage out of the waveguide. The presence of regions with refractive indices comparable with that of the waveguide, such as a bulk GaN substrate, additionally promotes the leakage of the cavity mode. The evanescent field from the core region can interact mutually with these adjacent layers. Parasitic waveguides are formed. They can sustain an electromagnetic wave, which couples to the evanescent tail of a lasing mode. Since the wave penetrating the substrate can be subject to total internal reflection from the bottom Au-based electrode (especially under low angle of incidence), the entire laser stack, including the bulk GaN substrate, forms an over 60-μm-long cavity in transverse direction.

Each guided mode has a discrete value of a propagation constant. Because of a large thickness of the parasitic waveguide, many modes with different propagation constants can satisfy a condition of a standing wave in the transverse direction. As a consequence of a large number of propagation constants for modes in the active and the parasitic waveguide, they can match easily. Hence strong coupling between both sets of modes occurs, causing high losses of the laser mode that penetrates into the substrate.

The possible sources of of the substrate's considerable absorption can be twofold. On one hand, the material quality of bulk GaN crystals grown by high pressure method is limited mainly by significant amount of gallium vacancies. On the other hand, due to high unintentional residual oxygen doping, there exist a large population of free electrons, reaching concentration of the order of $5 \times 10^{19}\text{cm}^{-2}$ [140]. Classical Drude free-electron model predicts that free-carrier absorption α_{f-c} is proportional to the concentration n of free carriers and also increases as a square of the incident wavelength λ [141]:

$$\alpha_{f-c} \propto n\lambda^2 \tag{8.1.2}$$

Although the phenomenon is mostly pronounced for transition energies below 1 eV, for which the free-carrier absorption of GaN can be as high as 300 cm^{-1} [142], under the conditions described above, the free-carrier absorption tail becomes significant even for photon energies close to that of the lasing mode. Thus the joined contribution to the overall absorption induced by metallic contact, GaN-vacancy-related and free-carrier-based transitions account for the substrate loss in the range of 9 cm^{-1} [136], which is a significant part of the total internal propagation losses α_i presented in Table 6.2.

8.2 Scanning near-field optical microscopy

The dynamics of the waveguide modes on a laser facet were carried out by a home-made SNOM, which was developed by the group of dr U. T. Schwarz from the University of Regensburg. The measurements were performed on electrically driven laser diodes. For this reason there was no need for the optical excitation. The electroluminescent signal emerging from every given device was collected at the facet by a specially prepared single mode optical fiber. Each fiber was prepared by the tube etching technique [143, 144] in 40%

of HF at temperature of 30°C. Once the polymer mantel was removed by 98% of sulfuric acid at 116°C, the tapered fiber tip formed an almost perfect cone with an apex of less than 100 nm in diameter [145]. Thus a sub-100 nm resolution was achieved, which varied depending on an individual fiber tip.

Commercially available optical fibers covered by either Cr- or Al-based metallic coating can impose some experimental difficulties. P-type contact electrode is located very close to waveguiding layers. Its edge is rough and often overhangs the uncoated facet. Thus a short-circuiting of n- and p-type layers by the potential of the tip is possible. Also unstable behavior disturbing a consistency of the measurement can appear, when a fiber tip with a metallic coating approaches the facet. Hence the proper choice of the collecting fiber is so critical.

In order to control the gap between the waveguide tip and the sample edge a non-contact method, called sheer force feedback [146, 147], is usually used. The fiber is attached to a quartz tuning fork, which is excited to oscillate close to its resonance frequency of about 32 kHz. As a result, the fiber itself oscillates parallel to the surface with the amplitude of a few nanometers. After the initial coarse approach, the final stage of tip positioning begins at distances less than 20 nm from the sample surface. Sheer forces, i.e. intermittent contact and electrostatic forces [148], detune the resonance frequency so that the oscillations are damped. A sheer force sensor delivers a feedback signal to a piezoactuator, which finally stabilizes the tip just a few nanometers away from the sample surface (See Figure 8.1).

Results of the measurement were transferred from a fast photomultiplier to an oscilloscope and were collected in the form of a data cube containing two spacial coordinates corresponding to the fiber tip position and a temporal coordinate reflecting the evolution of the optical signal in time. The data yielded a complete information on spatial and temporal mode dynamics during the driving pulse. A more detailed description of the entire setup and a fiber tip preparation technique can be found elsewhere [145].

8.3 Near-field pattern

As it has already been stated, most of practical applications require enhanced spatial and temporal stability of the output beam. High power InGaN lasers with a buried amorphous AlN layers used as a current and optical confinement were reported to have a kink-free

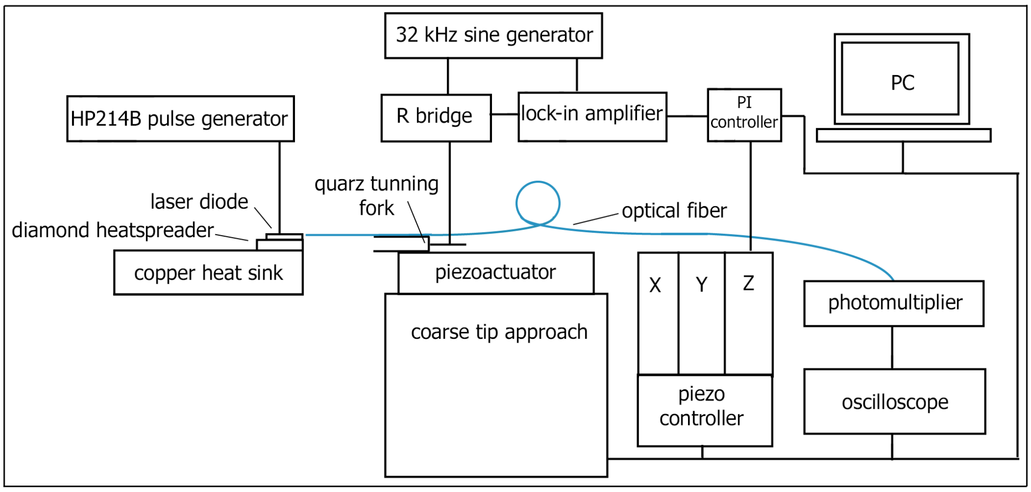

Figure 8.1: Schematic picture of the home-made time-resolved SNOM setup.

output up to 400 mW of output power [149]. If one wants to increase the output power even further, e.g. up to a few watts, a broad-area devices need to be utilized in order to stay below the critical optical power density, that damage the laser facets. The limit for this catastrophic optical mirror damage (COMD) is considerably higher for III-nitride based LDs (ca. 50 MW/cm^2) than for the arsenide-based ones (ca. 4-5 MW/cm^2). Despite larger COMD limit, there are considerable restrictions imposed on maximum optical output power of 2 μm-wide blue-violet LDs capable of maintaining a single mode operation [128]. Thus a broad-area laser geometry would be a reasonable alternative chosen to push the output power towards higher range. However, when this device geometry is employed, a lot of care must be taken in order to control the spatial distribution of the light field on the laser facets and its evolution with time. This was the motivation of the analysis regarding waveguide mode dynamics carried out on a nitride-based laser diodes with a 20 μm-wide mesa stripe with a typical cavity length of 500 μm being subject to development in order to achieve a few watts of output power.

Time-resolved SNOM is a very powerful experimental approach , when employed to analysis of waveguide mode dynamics. There is a number of studies concerning the investigation of a ridge width dependent lateral mode stability as well as near- and far-field dynamics of (Al,In)GaN laser diodes grown on SiC substrates employing this technique [150, 138, 151]. None of them, however, refers to nitride-based devices grown homoepitaxially on the native bulk GaN substrate.

Our measurements were performed on a set of devices with the active region formed by a sequence of 10 QWs, each of them consisting of 5-nm-thick layer of $In_{0.1}Ga_{0.9}N$ separated by 7.5-nm-thick QBs based on $In_{0.01}Ga_{0.99}N$. The mesa of the analyzed device was processed in a form of a 20-μm-wide stripe. From now on, we will denote this sample as LD2341. The complete structural data is available in Appendix A for the reader's reference.

8.4 Antiguiding and filamentation

For the purpose of the analysis, LD2341 was mounted p-type up on a copper block that assured a sufficient heat dissipation. The sample was operated in a pulse regime with a duty cycle of $10^{-3} - 10^{-5}$ and a pulse length up to 500 ns. Pulsed operation was necessary to suppress temperature-induced effects. Carrier-photon interactions could be revealed more easily this way.

Changes of total emission intensity collected from the laser facet during a single current pulse depend strongly on the applied current value. Surface-averaged emission intensity stays always constant in time below the lasing threshold. However, when the driving current is increased above its threshold value, total averaged intensity starts to fluctuate. A typical temporal dependance of the emitted light intensity is depicted in 8.2. The initial intensity spike can be attributed to a non-ideal impedance matching of the analyzed LD to a 50 Ω coaxial transmission line. The previous chapter dealt with the aspects of significant active region heating after a current flow is turned on. The considerable temperature increase initiated at the leading edge of a driving pulse takes place up to a microsecond range [152] and is accompanied by a subsequent resistance drop. Thus it is difficult to suppress transient fluctuations of the current flow, which seem to yield the significant contribution to the initial intensity drop.

Relaxation oscillations of carrier and photon density together with thermally-induced reduction of internal efficiency and increasing threshold current can also add up to the overall effect of the optical intensity drop. This behavior is then counteracted by a better mode guiding as a result of the temperature increase underneath a laser ridge.The higher temperature, the larger difference between refractive indices of GaN waveguide and AlGaN-based cladding [153]. Towards the end of each driving pulse, due to insufficient thermal

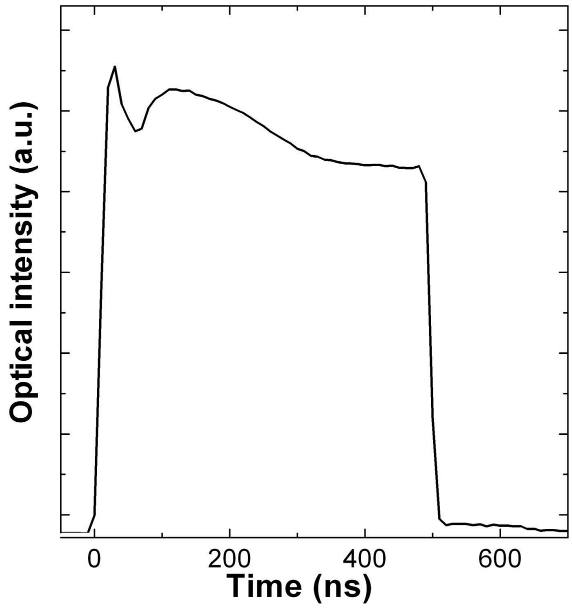

Figure 8.2: Temporal evolution of total optical intensity integrated over the entire laser facet during a 500-ns-long driving current pulse

conductivity of the GaN substrate resulting in a local temperature increase, the internal quantum efficiency deteriorates and the whole signal weakens [152].

The recorded near-field intensity distribution for three different currents (0.9 I_{th}, 1.1 I_{th} and 1.4 I_{th}) are depicted in Figure 8.3(a-c), respectively. Under carrier injection close to the lasing threshold, i.e. slightly below and above it, spatial electromagnetic field distribution on a laser facet stays roughly uniform (Figure 8.3(a)). This kind of behavior can be attributed to diffraction effects and the divergence of the wavefront caused by non-uniform distribution of injected carriers across the laser ridge as predicted by theoretical calculations concerning formation of optical wavefront under such conditions [154].

Because of the low laser beam intensity and the lack of gain saturation, the current flow path is followed by the excited carrier distribution. It is worth noticing that carrier- and temperature-induced refractive index changes counterbalance. The larger the carrier concentration, the smaller refractive index. The influence of temperature on refractive index is opposite. As a result, defocusing of the laser beam caused by the increased carrier concentration underneath the central part of the upper p-type electrode is counteracted by a better waveguiding in lateral as well as transverse direction induced by temperature

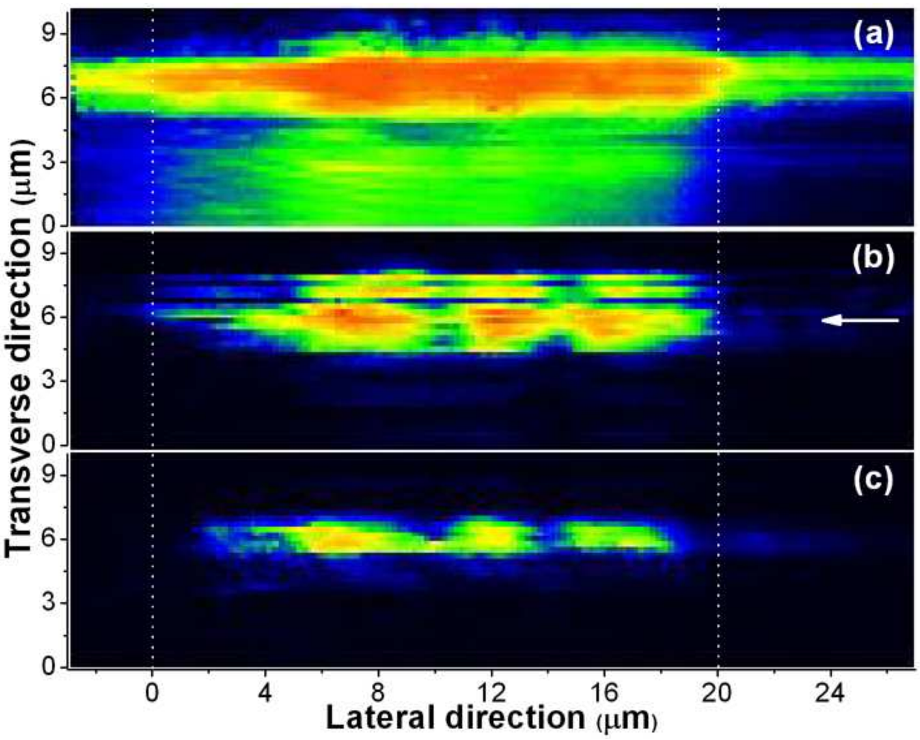

Figure 8.3: Near-field intensity distribution collected for LD2341 having 20-μm-wide mesa stripe driven by three different excitation currents: (a) 0.9 I_{th}, (b)1.1 I_{th}, (c) 1.4 I_{th} at $\tau = 100$ ns after the beginning of the driving pulse. The area at the bottom part of each scan corresponds to the substrate. Dotted lines mark the estimated position and width of the mesa stripe.

effects. The antiguiding of the gain medium and diffraction effects finally give rise to a diverging wavefront.

Antiguiding of a gain medium originates from carrier concentration noise within the LD's active region. This effect induces defocusing and detuning from a maximum gain frequency. The phenomenon can be estimated by the antiguiding (or linewidth enhancement) factor r_{ant}, described by a relation between the medium refractive index n, its carrier density induced change δn and the differential gain $\partial g/\partial N$ experienced by photons of a given wave vector $\mathbf{k}$.

$$r_{ant} = -\frac{k}{n}\frac{\frac{\partial(\delta n)}{\partial N}}{\frac{\partial g}{\partial N}} \tag{8.4.1}$$

Its quantity represents the magnitude of the amplitude-phase coupling originating from the strong refractive index dependance on the carrier density. Consequently, the emission linewidth is determined not only by the spontaneous recombination noise but also by the amplitude and phase fluctuation induced by chaotic changes in carrier concentration.

Values of the antiguiding factor of III-nitride system based laser structures, which were predicted theoretically [155] as well as confirmed experimentally [156] change from about 15 to 4 depending on a carrier injection level and quantum well thickness. They are comparable with the results reported for their arsenide- and phosphide-based counterparts [157, 158].

The larger value of the antiguiding factor, the greater tendency for the filament formation, which can be easily observed in Figure 8.3(b-c) as the driving current is increased significantly above threshold followed by a rapid and intense build-up of a photon field. At sufficiently high excitation the intensity distribution of a cavity mode burns a spatial hole along the resonator. Consequently, carrier density is reduced and gain saturation starts to occur. As a result, a local increase of refractive index along the resonant cavity leads to the enhanced focusing of the lasing mode (Figure 8.3(b)), which burns a deeper hole in spatial carrier distribution and even stronger focusing (Figure 8.3(c)). The observed phenomenon is commonly referred-to as a filamentation [42].

Formation of filaments leads to a wavelength shift and considerable spectral broadening as a response to changes in excited carrier density [43]. This in turn results finally in a multimode operation, which is not acceptable in many applications. The likelihood of filament formation raises with increasing ridge width and seems to be indispensable in high power working regime. Thus without strict constrains and a sophisticated structure engineering, inferior properties of the laser beam are expected in terms of the spatial and temporal stability.

Large values of the antiguiding factor are a characteristic feature of nitride-based materials. They result from the high joint density of states, because of higher electron and hole effective masses in nitrides as compared to other laser-related compounds. However, theoretical results derived from microscopic theory as well as experimental studies have shown [155, 156], that by increasing the quantum well width and consequently the carrier injection level needed to achieve a desired material gain, one can try to counteract the tendency for filament formation.

Increase of the dipole matrix element, caused by the gradual screening of internal piezoelectric and spontaneous fields, has the opposite influence on the refractive index change than the impact induced by increment in carrier concentration. High values of the antiguiding factor can be reduced even three times for the wide range of peak material gain values, when quantum wells thicker than 4 nm are used [155]. Because the current study concerns devices, which were driven significantly above the lasing threshold, we regard spontaneous and piezoelectric fields as screened by carrier injection and ionization of shallow Si donors implemented into the barriers [60]. In addition, relatively wide (5 nm) quantum wells are expected to efficiently reduce the antiguiding factor and improve the stability of electromagnetic field, moving the onset of filamentation towards higher currents above threshold [154].

Filamentation is finally balanced by the diffraction limit, carrier diffusion length and dispersion of refractive index. The experimental analysis indicates, that for a current value around 1.4 I_{th} formation of three or four filaments is observed, depending on a given LD. The width of each filament varies around 3 μm, which is the value predicted theoretically for wide stripe lasers [155].

The localization of filaments can be greatly affected by inhomogeneities of the crystalline structure of the resonant cavity, in particular dislocations. Excited carriers, which are not depleted by the fundamental mode, account for the multimode operation. Spatial coherence of the laser beam deteriorates and striped patterns in the far-field appear, becoming more pronounced with the rising ridge width [159]. Although filamentation seems to be indispensable in broad area lasers, the tendency for filament formation can be limited by a careful design of the active region, proper choice of the stripe width and mirror reflectivity coefficients. All these factors considered together assure a flat phase distribution on the laser facets. Utilization of unstable resonators [154] can also be a valuable alternative solution suppressing the formation of filaments.

Another information that can be derived from Figure 8.3(a-c) is the confirmation of a weak waveguiding and a strong leakage of the guided mode into the bulk GaN substrate. Such a leakage is expected for every device below the lasing threshold, since spontaneous photons are emitted into the entire solid angle. Only a small fraction of them is coupled into the optical waveguide. Thus no lasing mode can be sustained. It appears that the total intensity of spontaneous radiation penetrating the substrate equals 40% of that emerging out of the waveguiding layers. This value is reduced down to 10%, when the laser diode is operated significantly above threshold. The onset of guided modes of the resonant cavity improves the ratio. Also a possible temperature-induced improvement in waveguiding properties of GaN/AlGaN layers through increased difference of refractive indices cannot be neglected. From practical point of view this result is still not satisfactory as it introduces significant propagation loss. To some extend the fact of a weak waveguiding explains high threshold current densities and the low slope efficiency (rarely exceeding 1 W/A) indicating the need of a better structural design of the entire laser stack.

As it was stated previously, the evanescent tail of a weakly guided cavity mode, which penetrates regions beyond the outer cladding, easily couples into parasitic modes of the lossy bulk GaN substrate. After reflection from the bottom metallic Au-based electrode, additional resonator can be formed in transverse direction, across the entire laser stack. The typical longitudinal mode spacing $\Delta\lambda$ derived on grounds of a Fabry-Perot interference can be described by the formula [160]:

$$\Delta\lambda = -\frac{\lambda^2}{2Ln}(1 - \frac{\lambda}{n}\frac{dn}{d\lambda}) \tag{8.4.2}$$

The modal spacing of GaN-based LD with a 500-μm-long resonator emitting around 400 nm should be close to $\delta\lambda = 0.055\ nm$. The spectra presented in Figure 8.4 was collected through the courtesy of dr T. Ochalski and his co-workers from Tyndall National Institute at University College Cork. The data collected for a similar device confirms the calculation. However, dense longitudinal mode spacing is superimposed on slower varying oscillations with a period of about 0.35 nm. This effect can be explained on grounds of a mode leakage, which forms a standing wavefront in the substrate. Assuming refractive index for GaN of 2.51 and its dispersion of $-1.3 \times 10^{-3}\,\mathrm{nm}^{-1}$ [160] as approximately constant within the analyzed spectral range, one obtains a thickness of a transverse resonator of 76 μm, which is roughly the thickness of the bulk GaN substrate.

Thus the presence of substrate modes is revealed not only in near-field imaging, but it also strongly influences the laser spectra. An extensive analysis of the nature of substrate modes has been lately carried out in detail as well [136]. Suppression of excess propagation loss introduced by the highly absorbing GaN substrate, p-type cladding and subcontact layers are of crucial importance and are extensively studied in literature [161, 162, 133, 137].

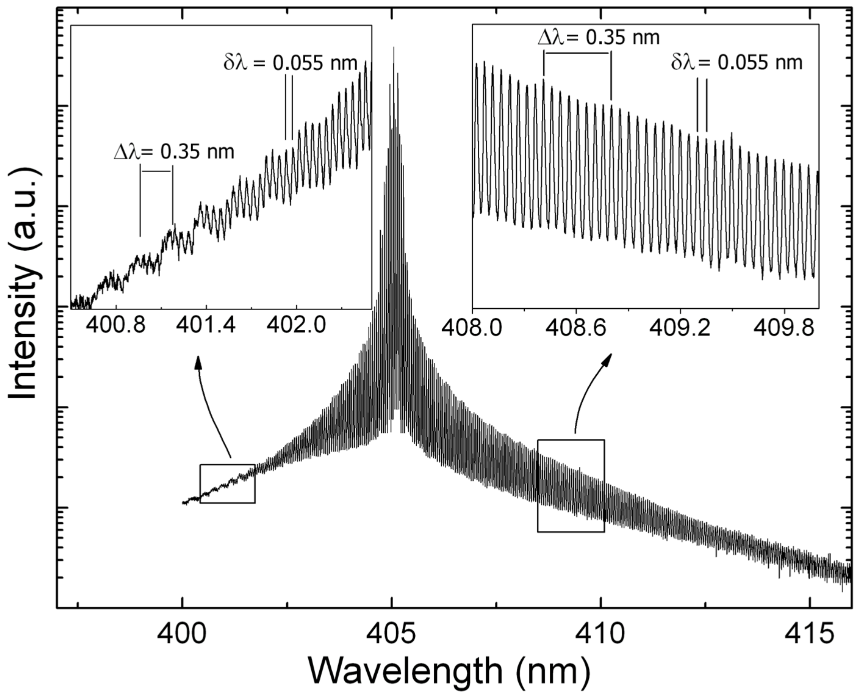

Figure 8.4: Laser spectra taken slightly above a lasing threshold. The spacing $\delta\lambda = 0.055\ nm$ is superimposed with a beating pattern of a period $\Delta\lambda = 0.35\ nm$.

8.5 Dynamics of the cavity mode

Chaotic fluctuations of injected carrier concentration and temperature changes under the broad ridge lead to the lack of stationary conditions inside a resonant cavity. SNOM-based research reveals that the intensity distribution of cavity modes on a laser facet is subject to complicated spatial and temporal dynamic behavior.

To emphasize this fact, the cross section through the recorded data cube was made in the lateral direction along the axis defined by a maximum light intensity, i.e. roughly in a plane of the active region (see the arrow in Figure 8.3(b)). The temporal evolution of the light field intensity along this line during a 500-ns-long driving pulse can be easily observed. The dependance is again depicted in Figure 8.5(a-c) for different excitation conditions: 0.9 I_{th}, 1.1 I_{th}, 1.4 I_{th}, respectively. The steady spatial and temporal behavior observed below the laser threshold (Figure 8.5(a)) turn into complicated and chaotic interplay among filaments for larger currents (Figure 8.5(b,c)), which exists until the end of the driving pulse. No

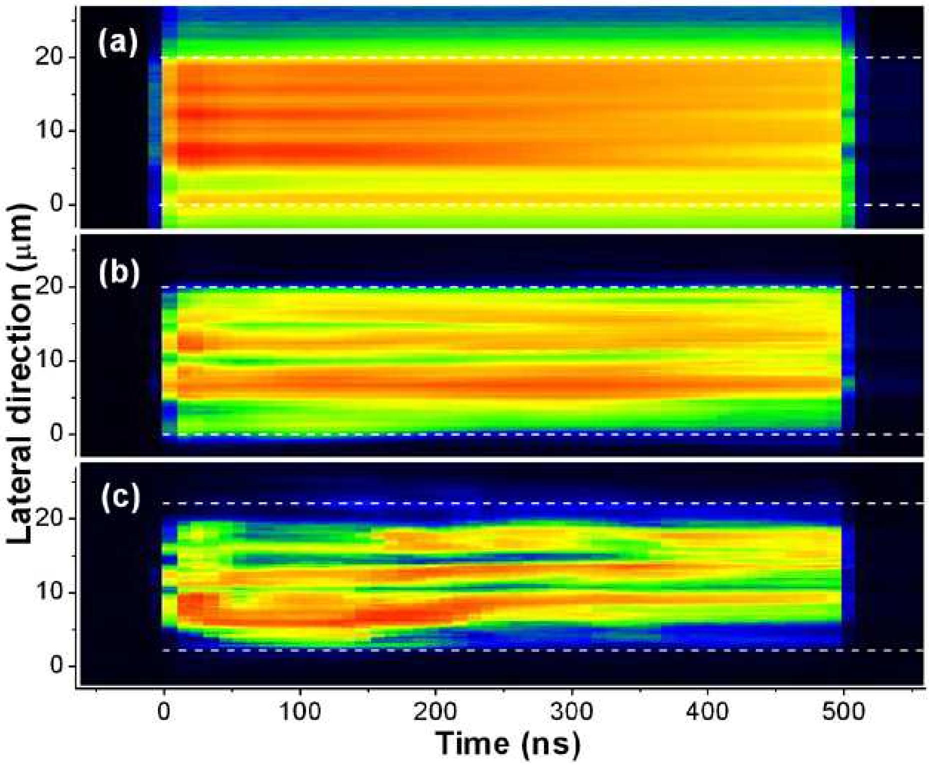

Figure 8.5: Temporal evolution of the near-field pattern along the axis defined by the arrow in Figure 8.3(b) collected for LD2341 under different excitation levels: (a) 0.9 I_{th}, (b) 1.1 I_{th}, (c) 1.4 I_{th} during a driving pulse of 500 ns. Dotted lines correspond to the mesa stripe width.

equilibrium state is reached during a current pulse of 500 ns.

Filaments, which are coupled to the apparent self-created waveguides, tend to merge, as if they were coherently coupled to one another. One can also easily observe, that the filaments tend to migrate in lateral plane. It could be interpreted as an indication of the spatial hole burning, which reduces the optical gain in the region of high intensity. Consequently, the gain in the neighboring regions is higher. Diffraction effects induce coupling to these adjacent regions and the filament migrates laterally. This behavior was confirmed by theoretical predictions, indicating that for certain laser configuration schemes, which differ by resonator type, ridge width and mirror reflectivity, steady-state solutions may exist only for the lowest excitation range [154].

8.6 Near-field-to-far-field evolution

Precise control of the distance between the fiber tip and the laser facet starting from 0 up to 30 μm enables the detection of a near field and its evolution into a far-field range. Figure 8.6 presents the near-field-to-far-field evolution in the transverse plane. This cut

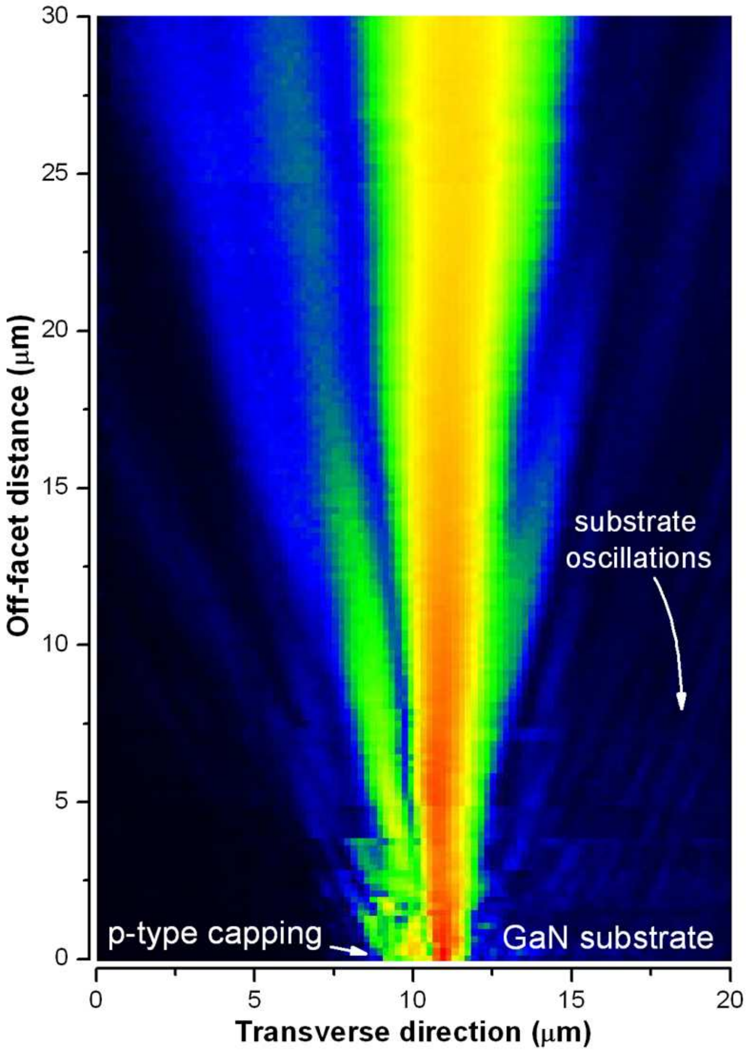

Figure 8.6: Transverse view of the near-field-to-far-field evolution of a laser beam.

through the far field distribution gives additional proof of a weak waveguiding we deal with in our laser diodes. The distinct fringes are observed on the bulk GaN side as a signature of the significant leakage of the guided mode into the substrate. What is difficult to interpret, is the high intensity emerging out of a region, which is thought to be the p-type GaN subcontact layer. The negative influence of the over 200-nm-thick GaN capping layer is strongly emphasized in literature [161, 162, 133]. In our case the thickness of this GaN-based subcontact layer was intentionally set to be close to 50 nm, in order to suppress the negative influence of its waveguiding properties. Thus it can be tentatively assumed, that this kind of behavior is rather due to diffraction effects introduced by pieces of metallization hanging over a laser facet than due to a real light field propagation through the p-type subcontact layer.

Figures 8.7(a-d) give information on the near-field-to-far-field evolution collected in the lateral plane at 40 ns, 150 ns, 300 ns and 500 ns after the beginning of a driving pulse, respectively. The chaotic behavior and competition between the adjacent filaments are

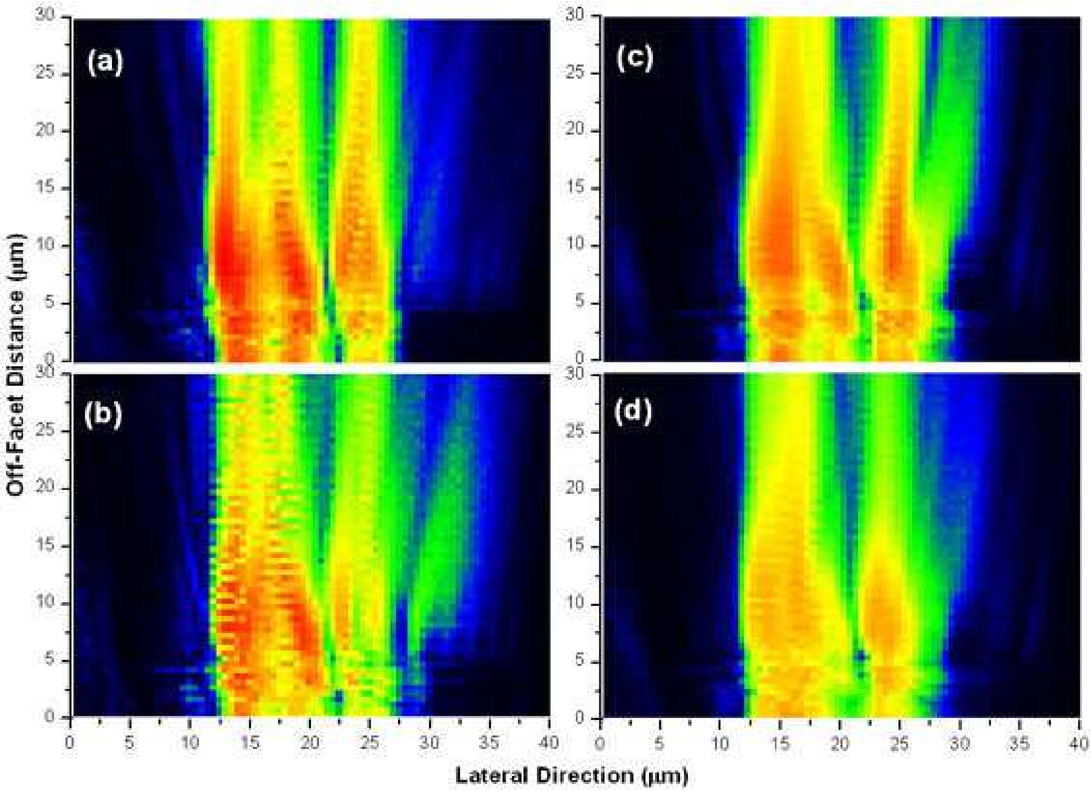

Figure 8.7: Lateral view of the near-field-to-far-field evolution of the laser beam at: (a) 40 ns, (b) 150 ns, (c) 300 ns, (d) 500 ns after the leading edge of the driving pulse.

clearly visible. Laser beams emerging out of individual filaments tilt in lateral plane in either side. Filaments tend to merge and the three of them observed initially only two remain at the end of a 500-ns-long driving pulse.

Intensity changes of individual filaments indicate a strong competition and coupling of light into one filament at the expense of another. The tilt of the emitted laser beam with respect to the resonator axis have already been explained by means of the changing phase distribution of the light field on the laser facet. This phenomenon was traced back to be caused by a complex thermal effects and chaotic carrier density fluctuations [150, 155] emerging from a spatial hole burning together with a current crowding and diffusion.

As presented in Ref. [151], Monte Carlo simulations of the wave front phase distribution on the laser facet based on the Fresnel model of light propagation yield an excellent reproduction of the measured near-field-to-far-field mode evolution including a beam steering effect at a fixed time. The calculations were carried out for a narrow 2.5 μm ridge laser, but the physics responsible for this behavior remain the same and only the degree of a filament interplay gets more complicated as revealed by the current research.

The presented analysis revealed that individual filaments tend to merge giving rise to high intracavity intensities, which increase the possibility of a material damage. The analysis of the evolution of a LD's near-field into far-field carried out in both transverse as well as lateral direction reveals strong inhomogeneity of the generated laser beam. Strong filamentation effects appear and influence the emission, including a strong beam steering as a result of a phase tilt and competition of the adjacent modes.

Prolongation of carrier diffusion length, reduction of internal propagation losses and careful choice of mirror reflectivity coefficients would help to reduce gain saturation effect which remains the main cause of self-focusing and filamentation. Potential improvement in intensity distribution on the laser facet is expected to be influenced by unstable resonator (plain-concave or plain-convex) introduced in the device design [154]. Diverging wavefronts generated this way would limit to high extent the focusing effect of the gain medium. Fundamental mode operation of broad area laser diodes should be thus achievable well above threshold. Experimental investigation of the far-field distribution of such devices would be of crucial importance from a practical point of view.

Chapter 9

Optimization of a laser cavity design

Properties of the optical amplification determined for different laser structures and presented in Chapter 6 yielded a useful information on the dependance between material gain and the excited carrier concentration. This relation defines many fundamental quantities governing the behavior of a laser diode and can be used as a starting point of a device optimization procedure. This analysis cannot be avoided when one wants to meet a desired reliability and specific application requirements.

9.1 Determination and significance of the unamplified spontaneous emission spectra

Experimental data presented in Chapter 6 relied on measurements of the optical gain derived by means of the optical excitation. The method gave us desired information regarding the optical feature of unprocessed laser structures prior to the complicated procedure finalizing the device fabrication process. However, this approach is subject to a considerable experimental uncertainty and gives a rough picture of the mechanisms taking place within the active medium and optical waveguide. There are also some significant discrepancies observed for InGaN-based light-emitting structures driven by means of either electrical or optical excitation [108]. For these reasons experimental methods based on the analysis of the electroluminescence spectra are in some cases more appropriate.

There are two major methods used to determine optical gain spectra of a processed laser chip. One of them, introduced by Hakki *et al.* [116] relies on the analysis of the modulation depth of longitudinal modes of a resonant cavity. The other was developed by Henry *et al.* [163] and focuses on the detection of the unamplified spontaneous emission spectra emitted by QWs. As it was shown in Chapter 8, GaN-based devices are characterized by a very dense longitudinal mode spacing. In order to spectrally resolve the modes, one needs to utilize a high resolution spectral analyzer. Trying to avoid this constraint, we decided to focus on the latter method. We will now try to briefly introduce the major assumptions of this approach, which in detail is presented in Refs [163, 164].

A detailed combination of thermodynamic and statistical arguments leads to the point, where the optical gain at a given transition energy $g(h\nu, \Delta E_f)$ for a corresponding quasi-Fermi level separation ΔE_f can be directly related to the equilibrium absorption α of the unexcited material [163]:

$$g(h\nu, \Delta E_f) = \alpha(h\nu)[exp\,(\frac{\Delta E_f - h\nu}{kT}) - 1] \qquad (9.1.1)$$

Additionally, it is possible to match the entire gain curve with the rate of spontaneous emission per unit volume R_{sp} for a certain excitation described by ΔE_f [163]:

$$R_{sp}(h\nu, \Delta E_f) = \frac{n^2(h\nu)^2}{\pi^2\hbar^3c^2}\alpha(h\nu)exp\frac{\Delta E_f - h\nu}{kT}. \qquad (9.1.2)$$

Both equations 9.1.1 and 9.1.2 mixed together can unambiguously reproduce the actual shape of a gain curve for the entire spectral range:

$$g(h\nu, \Delta E_f) = \frac{\pi^2\hbar^3c^2}{n^2}\,\frac{1}{(h\nu)^2}\,[1 - exp\,(\frac{h\nu - \Delta E_f}{kT})]\,R_{sp}(h\nu, \Delta E_f) \qquad (9.1.3)$$

In order to obtain the spontaneous emission rate $R_{sp}(h\nu, \Delta E_f)$, the observed spontaneous emission spectra $L(h\nu, \Delta E_f)$ expressed in arbitrary units needs to be corrected for the system response and collection efficiency by some constant C [163]:

$$L(h\nu, \Delta E_f) = C\,R_{sp}(h\nu, \Delta E_f). \qquad (9.1.4)$$

Special attention needs to be paid in order to collect true spontaneous emission spectra $L(h\nu, \Delta E_f)$ for each injection current. They should be subject to as little distortion as possible. The changes in spectral shape of spontaneous emission appear mainly due to photon reabsorption or amplification. Thus the emission spectra below and above threshold

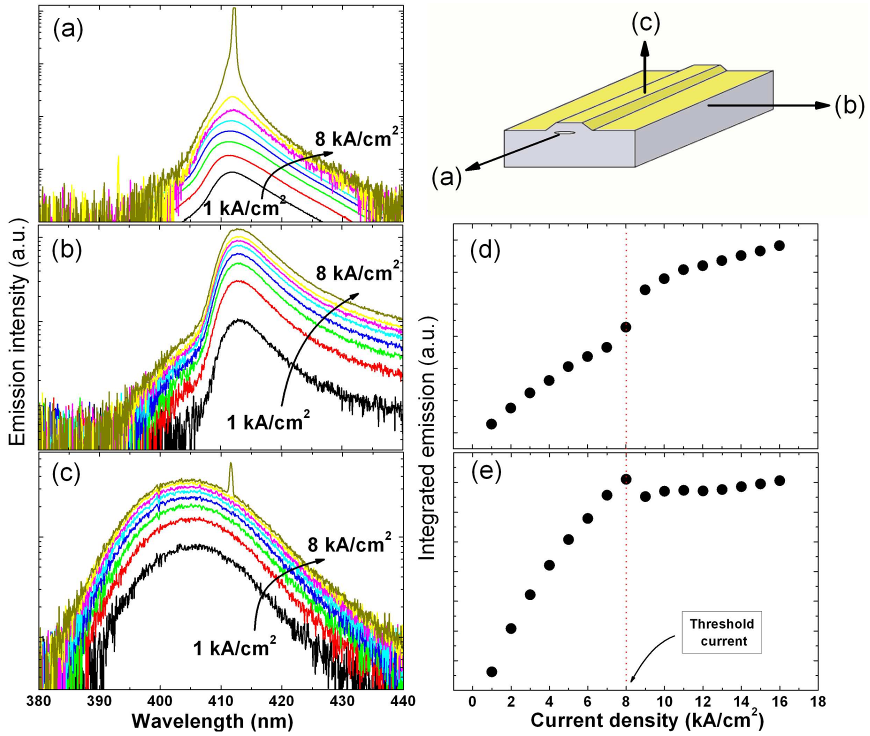

Figure 9.1: Spontaneous intensity collected from: (a) laser facet, (b) laser side, (c) through a top contact electrode for current densities covering the range of $1 - 8kA/cm^2$; (d) and (e) depict spectrally integrated spontaneous emission spectra taken from the laser side and through a top contact up to a $2\,J_{th}$, respectively. The schematic picture of a laser chip relates the light collection geometry to the corresponding designations

were collected in three different geometries, i.e. from the laser facet, laser side and through an opening in a top contact electrode as depicted in Figure 9.1(a),(b),(c), respectively.

Spontaneous emission at the laser facet (Figure 9.1(a))is peaked at the laser line, indicating a strong influence of optical amplification above transparency for the positive gain values. Figure 9.1(b) depicts spontaneous emission spectra collected from the laser side which are slightly redshifted due to a photon reabsorption by the unpumped InGaN quantum wells. Finally, optical signal collected through a transparent opening in a top contact electrode (Figure 9.1(c)) is strongly blueshifted due to negligible effects of photon reabsorption and amplification, which are observed from other directions. If one compares changes of spectrally integrated intensities, it can be seen that up to the current densities of twice the threshold value ($2\,J_{th}$) the optical signal collected from the laser side does not saturate, whilst the corresponding signal detected perpendicularly to the epitaxial layers clamps at threshold as appears from Figure 9.1(d) and (e), respectively. This fact can be regarded as a strong evidence supporting the assumption of a true spontaneous emission spectra emerging transversely with respect to the epitaxial layers. Another interesting feature that can be observed at threshold is that the abrupt increase of the optical signal detected from the lateral direction is accompanied by the corresponding drop of intensity in the transverse direction. Such a behavior can be related to the onset of lasing, which couples to the cavity mode a portion of photons that alternatively would be available to the spontaneous emission (Figure 9.1(e)). On the other hand, as seen in Figure 9.1(d), lateral current spreading effect resulting in an inhomogeneous gain profile in the direction perpendicular to the cavity axis is responsible for the above-threshold intensity increase. The step-like intensity increase observed in the vicinity of the laser threshold can be attributed to the scattering of the lasing mode induced by waveguide imperfections.

Thus once calibration constant C and the separation of Fermi levels for each injection current ΔE_f are known, it is possible to determine a corresponding gain curve $g(h\nu, \Delta E_f)$.

The separation of Fermi levels can be derived from the assumption that for a certain range of photon energies, which are sufficiently high to neglect the influence of band filling and many-body effects on modification of the absorption spectra $\alpha(h\nu)$, the value of absorption remains constant regardless of the injection level [163]. Thus the ratio between high energy tails of spontaneous emission spectra taken below and at threshold are solely proportional to separation of Fermi levels [163].

$$\frac{L(h\nu, \Delta E_f)}{L(h\nu, \Delta E_f^L)} = exp(\frac{\Delta E_f - \Delta E_f^L}{kT}) \tag{9.1.5}$$

For the purpose of this particular analysis, the energy of 3.2 eV was chosen as a high enough to secure the above-mentioned requirement.

Because lasing occurs roughly at peak gain energy, comparing a derivative of Equation 9.1.3 to zero at lasing line (e.g. 3.05 eV in case of the analyzed device) yields separation of Fermi levels at threshold. Consequently the separation of Fermi levels for the remaining injection currents can be derived from Equation 9.1.5. As it is depicted in Figure 9.2, for a device lasing at 3.01 eV the separation of quasi-Fermi levels reaches 3.05 eV at threshold and sets in following a local carrier concentration in QWs.

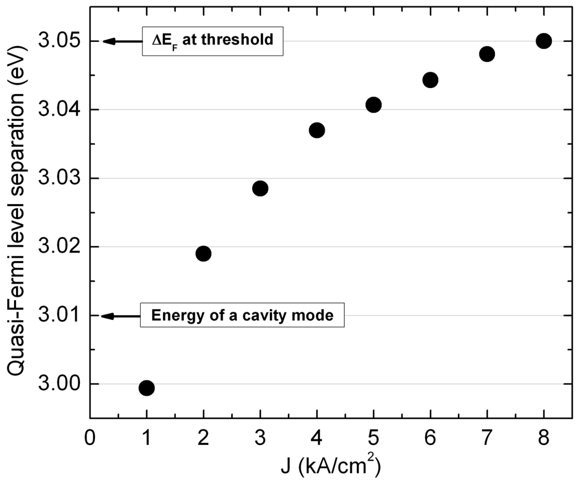

Figure 9.2: Separation of quasi-Fermi levels derived from the ratio between high-energy tails of spontaneous emission spectra for different injection levels.

Providing that all the gain curves derived from Equation 9.1.3 have a real shape (i.e. a true spontaneous emission spectra were collected) and also neglecting free carrier scattering within quantum wells, the results can be calibrated to yield absolute values of material gain in the active region. The experimental analysis carried out for $In_{0.1}Ga_{0.9}N$-quantum- well-based active region revealed that photons having energy of 3.2 eV are subject to equilibrium absorption of 7.3×10^4 cm^{-1} [58]. As a result one arrives at a point where the derived gain curves can be expressed in real units as depicted in Figure 9.3.

Thus a threshold material gain determined from the experiment reaches about 1500 cm^{-1}. A blueshift of about 40 meV is observed because of a combination of bandfilling and screening of internal piezoelectric fields as the injection current is being increased up to the threshold value. Because the absorption coefficient used for the calibration of the experiment was determined from transmission measurements in transverse direction, the derived gain curves should be interpreted rather as an average material gain throughout the entire active region. Nonuniform QW carrier injection, mentioned in Chapter 5, results in the inhomogeneous gain distribution among QWs additionally complicating our interpretation of the experimental results. In the final section of this chapter we will propose the interpretation based on theoretical calculations performed by LASTIP solver together with the suggestion concerning the optimum number of QWs.

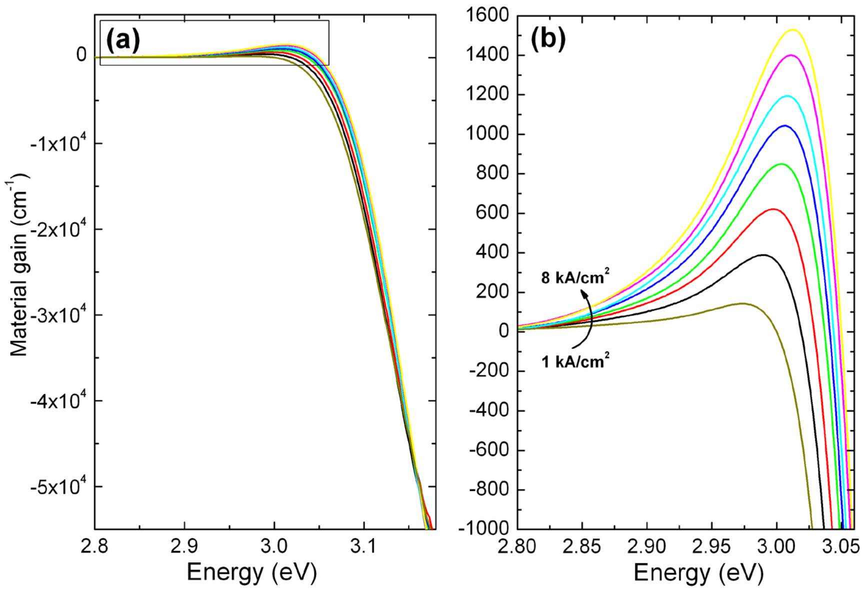

Figure 9.3: Active region material gain (a) and its magnification (b) derived for current densities ranging from $1kA/cm^2$ to $8kA/cm^2$.

The analysis of the peak gain dependance on injected carrier density fitted with Equation 6.2.1 (see Figure 9.4) reveals that the transparency was reached at 0.51 kA/cm^2.

The dependance of peak gain versus injected current presented in Figure 9.4 is probably the most important information that can be derived from this kind of analysis. The approach can be further enhanced by employing an optimization procedure in order to find the cavity parameters for which devices with a given structure can reach possibly the best working conditions.

9.2 Optimization of a resonant cavity length

In order to relate the laser driving current to basic cavity parameters it is useful to define the following equation [43]:

$$I = J_v A L_a + I_P(1 + \frac{\alpha_i L}{ln(1/R)}), \tag{9.2.1}$$

where the first summand corresponds to laser threshold defined by current density per unit volume J_v multiplied by the cross-sectional area of the active region A and the cavity length L. The second summand accounts for a current above threshold I_P necessary to reach

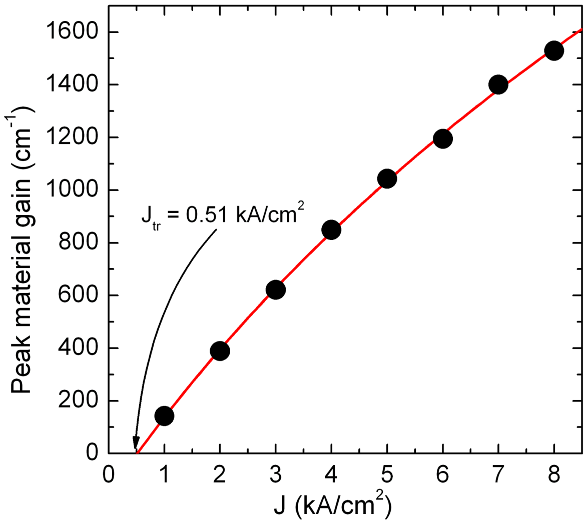

Figure 9.4: Peak material gain as a function of the applied current density fitted with Equation 6.2.1. Transparency level derived this way equals 0.51 kA/cm^2.

a desired output power P_{out}. This term can be expressed by means of a ratio F of light coupled out of a desired mirror facet to the total optical power and the above-threshold internal quantum efficiency η_i, which estimates a fraction of current above threshold resulting in stimulated emission [43]:

$$I_P = \frac{q}{h\nu}\frac{P_{out}}{\eta_i F} \tag{9.2.2}$$

Combined Equations 9.2.1 and 9.2.2 relate the output power P_{out} and the injected current above threshold I_P by parameters corresponding to: internal propagation losses α_i, cavity length L, mean mirror reflectivity R and internal quantum efficiency η_i. They define the LD's external quantum efficiency η_d. If one additionally applies the Equation 2.7.1 estimating a threshold for lasing action, it is possible to finally end up with the following formula:

$$I = [\frac{Jv + \frac{I_P \alpha_i}{A ln(1/R)}}{g - \frac{\alpha_i}{\Gamma_{xy}}}]\frac{A}{\Gamma_{xy}}\, ln\frac{1}{R} + I_P, \tag{9.2.3}$$

Where g stands for the optical gain and Γ_{xy} corresponds to the cross-sectional optical confinement. This relation can be used to find the operating point on a gain-versus-current curve at which the current-to-gain conversion ratio is the largest. Consequently, the term in square brackets reaches its minimum, giving the possibly lowest operating current that can be achieved.

Before getting into the details of an optimization procedure, it is necessary to define values of all parameters plugged into the presented equations. Because the threshold current density depends on a cavity length, it is possible to extract values of internal efficiency η_i and internal propagation loss α_i by fitting experimental data acquired from a set of lasers with different resonator length with a theoretical equation [165]:

$$J_{th} = \frac{J_{tr}d}{\eta_i} + \frac{d}{\eta_i g' \Gamma_{xy}}\alpha_i + \frac{d}{\eta_i g' \Gamma_{xy}}\frac{1}{L}ln\frac{1}{R} \tag{9.2.4}$$

The first term defines transparency through transparency current density per unit volume J_{tr} and an active region thickness d. The second and the third term define internal propagation and mirror loss, respectively. The results of the measurement together with a linear fit are plotted in Figure 9.5. The value of differential gain g' were deduced from the dependance describing relation between the optical gain and the injected current density, as presented in Figure 9.4.

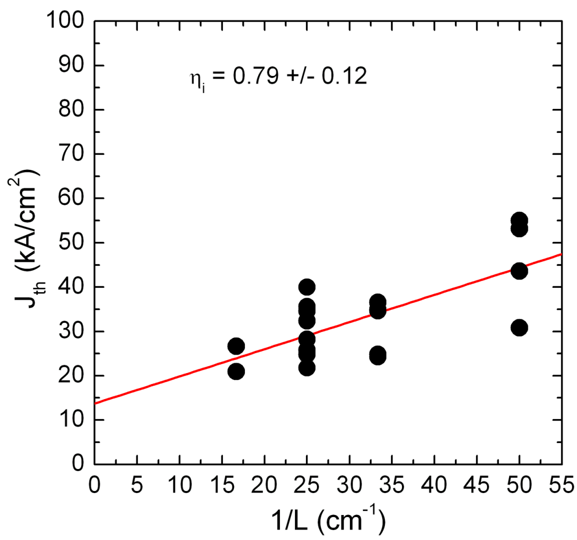

Figure 9.5: Threshold current density as a function of reciprocal cavity length. According to equation 9.2.4 internal efficiency can be assumed to be close to 80%.

The value of internal efficiency η_i of about 0.8 seems to be reasonable. The amount of total internal propagation loss of this particular set of laser devices reaches however $\alpha_i = 77$ cm^{-1}. It is obvious that this value is dangerously large and should be definitely minimized. The lack of mirror coatings and considerable internal propagation loss explain large threshold current densities compared to the device analyzed in previous chapter. For the sake of finding the best cavity parameters and to validate the simulation, the value of $\alpha_i = 5$ cm^{-1} derived from a similar measurement published elsewhere [140] was alternatively chosen. These two values indicate however the necessity of reducing the electron overflow over the EBL and optimizing properties of the waveguide.

Because of the fact that the gain versus current relation was derived for a laser diode with coated mirrors having the threshold current density of 8 kA/cm^2, it is necessary to take into account additional constrains. The proportion between optical power coupled out of each laser facet was 6:1. Using the following equation [43]:

$$F = \frac{1 - r_1^2}{(1 - r_1^2) + \frac{r_1}{r_2}(1 - r_2^2)}, \tag{9.2.5}$$

relating both mirror reflectivity coefficients r_1 and r_2 to the ratio F between the optical power on a given laser facets to the total optical power emerging out of the resonant cavity, it was possible to find mirror reflectivity coefficients that once put into Equation 9.2.3 assure the same threshold current and output optical power ratio as the ones measured for a real laser diode under investigation. The values of all parameters used in the subsequent simulation are summarized in Table 9.1.

Figure 9.6 consists of the most important data emerging out of the simple simulation procedure. The analysis has been carried out for two different device working conditions. The first one was the analysis of the threshold current (black solid curve in Figure 9.6(a)), which was thought to validate the choice of parameter values by matching the material gain value of about 1500 cm^-1 measured at threshold with the device's threshold current of 800 mA and the detected output power ratio F at both facets by means of Equations 9.2.2, 9.2.3 and 9.2.5. The next step was to consider a practical situation demanding the presence of 200 mW output power (red solid curve).

Figure 9.6(a) suggests that according to the results of the analysis, the real LD worked at the operation point, which was only slightly detuned from the optimum. The threshold current of 800 mA and the operating current at 200 mW optical output of about 900 mA could be reduced down to about 770 mA and 880 mA, respectively, if the device was brought closer to the vicinity of its working optimum. This means that the point on the gain-versus-current curve for which the device reaches its threshold condition as described

Parameter Name	Symbolic Designation	Value	Unit
Emission energy	$h\nu$	3.01	eV
Total propagation loss	α_i	5	cm^{-1}
Free-carrier absorption per well	α_1	130	cm^{-1}
RT carrier lifetime	τ	650	ps
Differential gain	g'	4.41×10^{-4}	cm^2/kA
Empirical gain parameter	g_0	2375	cm^{-1}
Transparency current density	J_{tr}	0.51	kA/cm^2
Shifting current density	J_s	7.72	kA/cm^2
Reflectivity coefficient	r_1	12.6	%
Reflectivity coefficient	r_2	54.2	%
Optical confinement	Γ_{xy}	3.84	%
Optical confinement per well	Γ_1	0.77	%
Internal quantum efficiency	η_i	80	%
Active region thickness	d	22.5×10^{-3}	μm
Stripe width	w	20	μm
Cavity length	L	500	μm

Table 9.1: Parameter values characterizing laser diode operation chosen for subsequent cavity design optimization

by Equation 2.7.1 should be shifted from 1500 $cm^{-}1$ to 1100 $cm^{-}1$ to minimize threshold or to 1150 $cm^{-}1$ to minimize the operating current at 200 mW optical output.

Equation 2.7.1 suggest the possible ways of shifting the laser threshold. For practical reasons it is clear that the internal propagation loss α_i should be kept at the possibly lowest value. Because it is impossible to completely rule out the propagation loss, the optimum design leads to the cavity length L→0 and mean mirror reflectivity R→1 as this kind of design assures the lowest cavity loss and mode volume. Thus it is useless to optimize all possible cavity parameters at the same time.

However, practical applications demand that the optical power coupled out of the resonant cavity should be maximized. Because of this fact, a laser facets are coated with antireflection and highly reflecting films depending whether it is a front or a rear end of a device. On the other hand it is difficult to precisely control mirror reflectivity coefficients to meat their optimum values.

As a result it seems that the simplest way to shift the threshold is to change the cavity length L. By doing so, it was found that in order to approach the optimum, the cavity length should be increased. The minimum threshold current would be achieved by extending the

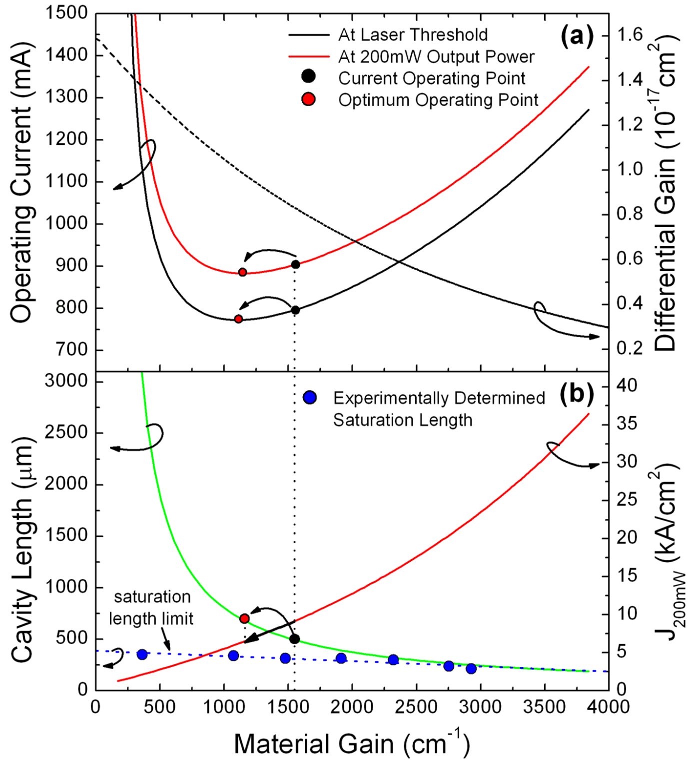

Figure 9.6: (a) Expected operating current versus material gain at threshold (black solid curve) and at 200 mW output power (red solid curve) together with differential gain estimated from data in figure 9.4. (b) Cavity length changes necessary to shift a threshold condition to a corresponding material gain value together with related operating current density at 200 mW output calculated using relevant curve from (a). Circles filled with blue depict results concerning saturation length derived from optical excitation for sample LD410 presented in Chapter 6.

resonator length from 500 μm to 720 μm. On the other hand, in order to achieve the minimum operating current at 200 mW output, the cavity length should be increased to 690 μm. The operating points at which the device would reach its optimum are denoted in Figure 9.6 by means of the circles filled with red.

Although the range of material gain values for which operating currents do not vary from the optimum value by more than 10% is rather broad and extends from 560 cm^{-1} to 2300 cm^{-1}, it is beneficial to shift the operating point as close to transparency as possible. Figure 9.6(a) consist of information on the differential gain derived from the data depicted in Figure 9.4. By moving from one end of the above-mentioned material gain range towards the other, i.e. from 2300 cm^{-1} to 560 cm^{-1}, the value of differential gain increases by almost 50%. Since the differential gain defines the relaxation resonance frequency [43], this aspect of the device optimization is of a crucial importance in high-speed laser modulation.

Following the path of changing the cavity length in such a way that the varying mirror loss term in Equation 2.7.1 can establish a threshold condition for any material gain value between transparency and 4000 cm^{-1} leads to corresponding resonator length values depicted in Figure 9.6(b). A clear tendency can be seen indicating that the closer towards transparency one wants to move, the longer the cavity length should be utilized. Increasing the cavity length consequently limits the operating current density at which the considered device would have to be driven at 200 mW optical output as it also can be seen in Figure 9.6(b). As a result, by increasing the cavity length in order to move from the current operating point to the optimum operating point at 200 mW output power, it is possible to reduce the threshold current density from 8 kA/cm^2 at current laser threshold to 6.4 kA/cm^2 at 200 mW optical output power.

Thus one can bring up a question concerning the limit to which the cavity length can be extended. It clearly depends on the goal that needs to be achieved. Increased cavity length reduces the operating current density and thus prolongs the device's lifetime. It also shifts the threshold condition expressed by Equation 2.7.1 towards transparency, where the dependance of the optical gain on the carrier density is more steep (Figure 9.4). Consequently, the enhanced differential gain can be expected making a given LD more suitable for high-speed applications. Both targets can be achieved simultaneously within a reasonable range at the expense of doubling the operating current. Unfortunately, the formulas presented above do not include saturation effects. As revealed by gain measurements carried out for the sample LD410 by means of the optical excitation presented in Chapter 6, saturation occurs for each gain value as depicted by blue circles in Figure 9.6(b). Although the saturation length increases with shifting the operating point towards transparency, it stays well below the cavity length required to establish lasing for the desired material gain value. Rough estimations indicate that even in the present situation of the device having 500 μm-long cavity characterized by the average threshold gain value of about 1500 cm^-1, the expected saturation length of about 300 μm is considerably shorter than the length of the resonator.

Although the optical gain is expected to drop gradually for the cavity length exceeding

300 μm, the simulation presented in Figure 6.2(c) suggests that the dependance is not critical and the optical gain sensible to the electromagnetic wave covering the distance approaching 500 μm decreases by not more than 2%. The reduction of the optical gain, when compared to its nonsaturated value, becomes significant for cavity lengths exceeding 1 mm, as depicted in Figure 6.3. Consequently, we could assume that advantage of reducing the lasing threshold with increased cavity length (as expressed by Equation 2.7.1) is not prevailed by the disadvantageous gradual onset of the gain saturation.

However, it seems that without an additional analysis concerning the impact of saturation length on the performance of devices with different cavity lengths, it will be difficult to indicate undoubtedly the optimum dimensions of the resonator.

In order to calculate all of the data presented in Figure 9.6, constant cross-sectional optical confinement factor Γ_{xy} of 0.038 was used. Calculations were carried out by LASTIP laser simulation package. Equation 2.7.1 indicates however that laser threshold can be tuned by optimizing the waveguiding layers and consequently changing the optical confinement this way. As a result, in order to meet the optimum operation point at 200 mW output power, the present optical confinement should be increased to 0.051. Such a solution utilized in high-power application would increase the probability of encountering a problem of a mirror damage induced by increased optical density on both laser facets.

9.3 Optimum quantum well number

As it was mentioned before, the threshold optical gain value of 1500 cm^{-1} can be treated solely as a rough estimation of an average gain throughout the entire active region. Due to characteristic material properties of III-nitrides, a vertical carrier distribution in the active region consisting of five QWs is never uniform due to a poor hole mobility. Large valence band offsets between InGaN-based active region and AlGaN-based EBL create of a significant barrier for hole injection [108]. Additionally, the low mobility and thermal velocity of holes deteriorate a uniform hole distribution among wells in a transverse direction [111, 112]. The larger the distance from the p-type layers, the smaller hole population within consecutive QWs (see Figure 5.10(a)).

In order to estimate material gain in each QW, theoretical calculations using LASTIP solver were performed in cooperation with P. Mensz to interpret the obtained experimental results. Figure 9.7(a-d) presents the material gain distribution among different number of QWs. The actual data derived from the simulation was scaled in order to match the average value of 1500 cm^{-1} determined experimentally for a real LD with the active region consisting of a sequence of five QWs.

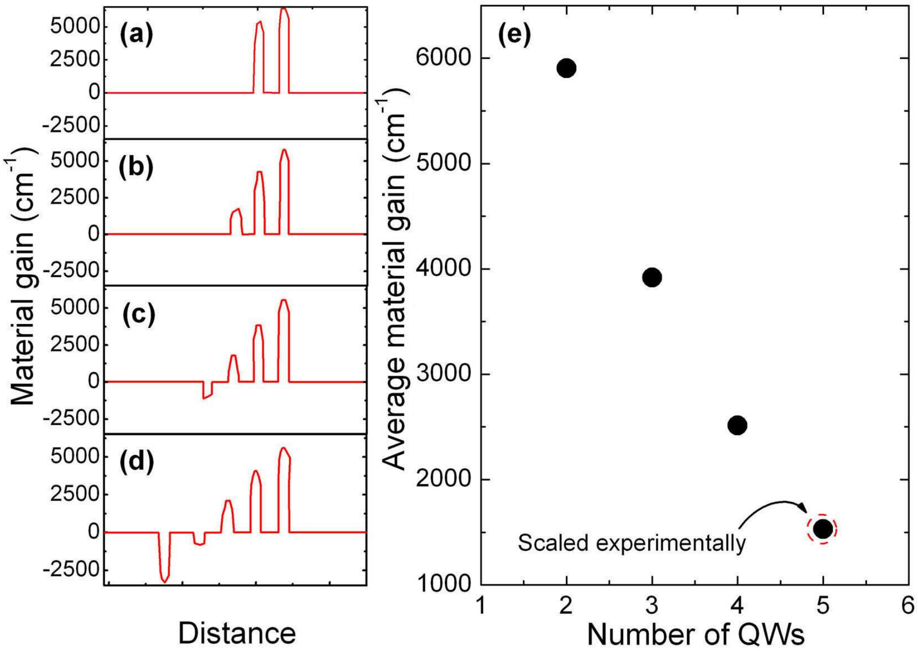

Figure 9.7: Distribution of material gain in active region consisting of different QW number (a-d) and the average material gain dependance on QW number scaled to the value obtained experimentally.

The calculations reveal that the last two QWs lying the furthest distance away from the EBL introduce the strong absorbtion and need to be eliminated unambiguously. By reducing the QW number from five to three one can expect from Figure 9.7(e) an over two-fold increase of the average material gain in the active region. Further reduction in QW number and its influence of the threshold current density is a complicated interplay among the optimum carrier capture-escape mechanisms, optical confinement and the volume of the active region that needs to be excited. For these reasons, the QW number should be optimized experimentally rather than by means of theoretical analysis, due to the lack of sufficient information regarding all mechanisms governing the operation of a real device.

Conclusions

Presented dissertation was devoted to investigation the major properties of semiconductor laser diodes fabricated at Institute of High Pressure Physics of Polish Academy of Sciences. All devices were deposited on high quality bulk GaN crystals achieved in the process of the high pressure synthesis. Original fabrication technology possessed by the Institute offers solid foundations for further development of optoelectronic devices.

In the course of this study it was possible to investigate carrier injection mechanisms determining light-current and current-voltage characteristics of each LD. Having such a background, we also gained some insight into the thermal stability of a given device and unveiled peculiarities of the device annealing by current and temperature. We also traced effects that the EBL imposes on the device performance. Different design approaches aiming at the reduction of the device's sensitivity to temperature changes were investigated, including modification of the QW indium content as well as changing dimensions of the entire active region core.

Practical work carried out in the course of this study led to the construction of the experimental setup enabling the analysis of optical gain in different structures by means of the optical excitation. On grounds of this experimental method we had the opportunity to familiarize ourselves with optical gain behavior characterizing laser structures with different QW indium content fabricated by two alternative growth techniques: MOCVD as well as PAMBE. It was also possible to determine approximate values of internal propagation losses.

Additionally, we drew our attention to temporal and spacial evolution of the electromagnetic field excited inside a resonant cavity. The picture we gained by using scanning near-field optical microscopy gave us a detailed insight into complicated dynamics and filamentation of the guided mode. The research also revealed problems with the proper waveguiding of the cavity mode, which need to be eliminated by the improved design of the laser stack.

Finally, we succeeded in determination of the device's junction temperature and also temperature profiles across the entire laser package. The obtained information was used to assess the thermal resistance of different mounting schemes. Simple numerical simulation allowed us to identify practical limits of CW operation and suggest some possible device optimization steps.

The problems undertaken by this dissertation are of fundamental importance in the area of the device physics. They involve original concepts developed by our research group. These topics are currently extensively studied in order to contribute to the device optimization steps. Because of many possibilities for practical applications, they constantly maintain their topicality among the scientific community.

Appendix A

In this Appendix details of the structures investigated in this work are described. Depending on a desired emission wavelength, these laser structures consist of InGaN-, GaN- or AlGaN-based active layers surrounded by Mg doped p-type or Si doped n-type epitaxially deposited waveguiding layers. These films are generally the same in most cases. Consequently, majority of the samples can be distinguished by differences in the active region design, which are presented in detail for each laser structure.

Table A.1 presents a standard sequence of buffer, waveguiding and subcontact layers, which is commonly used in every MOCVD-grown laser structure. Active region details of the investigated samples are depicted separately in Tables A.2, A.3, A.4, A.5.

Table A.6 presents structural details of the entire structure of LD370 investigated in Chapter 6. Due to the shift of the emission wavelength to 370 nm, QWs consist of a pure GaN and are sandwiched by $Al_{0.04}Ga_{0.96}N$-based QBs. Waveguiding and cladding layers consist of $Al_{0.04}Ga_{0.96}N$ and $Al_{0.12}Ga_{0.88}N$, respectively.

Finally, Table A.7 depicts details of a laser structure grown by PAMBE. The difference originates from the necessity of using indium as a group-III species forming a thin dynamic layer on the sample surface in order to assure a step-flow growth mode. Such a growth mode offers the improved structural quality. Excess indium incorporates into EBL and the above lying p-type layers distinguishing the structure from a corresponding sample grown alternatively by MOCVD.

Composition	Thickness (nm)
GaN:Mg	30
80 x (28Å of GaN:Mg / 28Å of $Al_{0.15}Ga_{0.85}N$:Mg)	430
GaN	90
$Al_{0.24}Ga_{0.76}N$:Mg	20
Device-dependent active region described separately	
$In_{0.02}Ga_{0.98}N$:Si	50
GaN:Si	50
110 x (29Å of GaN:Si / 29Å of $Al_{0.16}Ga_{0.84}N$:Si)	610
GaN:Si	450
GaN buffer	2000
GaN substrate	60000

Table A.1: Schematic representation of waveguiding, cladding and subcontact layers commonly used in the majority of the investigated samples.

	Active region design			
Sample	LD3460	LD2681	LD1450	LD2500
QW number	5	5	5	5
QW composition	$In_{0.1}Ga_{0.9}N$	$In_{0.08}Ga_{0.9}N$	$In_{0.1}Ga_{0.9}N$	$In_{0.16}Ga_{0.84}N$
QW thickness (nm)	4.5	4.5	5	5
QB composition	GaN:Si	$In_{0.02}Ga_{0.98}N$:Si	$In_{0.02}Ga_{0.98}N$:Si	$In_{0.04}Ga_{0.96}N$:Si
QB thickness (nm)	10	7	10	8
Cap composition	GaN	GaN	X	GaN
Cap thickness (nm)	6	6	X	6

Table A.2: Schematic representation of the active layers of samples LD3460, LD2681, LD1450, LD2500 investigated in Chapter 5.

	Active region design			
Sample	LD3180	LD3422	LD3411	LD2341
QW number	5	5	5	10
QW composition	$In_{0.1}Ga_{0.9}N$	$In_{0.1}Ga_{0.9}N$	$In_{0.1}Ga_{0.9}N$	$In_{0.1}Ga_{0.9}N$
QW thickness (nm)	4.5	4.5	4.5	5
QB composition	$In_{0.02}Ga_{0.98}N$:Si	$In_{0.02}Ga_{0.98}N$:Si	$In_{0.02}Ga_{0.98}N$:Si	$In_{0.01}Ga_{0.99}N$:Si
QB thickness (nm)	5.5	10	10	7.5
Cap composition	GaN	GaN	GaN	GaN
Cap thickness (nm)	6	6	10	6

Table A.3: Schematic representation of the active layers of samples LD3460, LD2681, LD1450 investigated in Chapter 5 and LD2341 investigated in Chapter 8.

	Active region design	
Sample	MQWLD	SQWLD
QW number	5	1
QW composition	$In_{0.1}Ga_{0.9}N$	$In_{0.1}Ga_{0.9}N$
QW thickness (nm)	5.5	9.5
QB composition	$In_{0.03}Ga_{0.97}N$:Si	$In_{0.02}Ga_{0.98}N$:Si
QB thickness (nm)	6.5	10.5
Cap composition	GaN	X
Cap thickness (nm)	6	X

Table A.4: Schematic representation of the active layers of samples MQWLD and SQWLD investigated in Chapter 5.

	Active region design		
Sample	LD390	LD410	LD430
QW number	5	5	5
QW composition	$In_{0.8}Ga_{0.92}N$	$In_{0.1}Ga_{0.9}N$	$In_{0.14}Ga_{0.86}N$
QW thickness (nm)	5.5	4.5	5.5
QB composition	GaN:Si	$In_{0.02}Ga_{0.98}N$	GaN:Si
QB thickness (nm)	6	7	6
Cap composition	GaN	GaN	GaN
Cap thickness (nm)	6	6	6

Table A.5: Schematic representation of the active layers of samples LD390, LD410, LD430 investigated in Chapter 6.

LD370	
Composition	Thickness (nm)
$Al_{0.12}Ga_{0.88}N$	300
$Al_{0.04}Ga_{0.96}N$	100
QW: 5 x GaN	5 x 5
QB: $Al_{0.04}Ga_{0.96}N$	10
$Al_{0.04}Ga_{0.96}N$	100
$Al_{0.12}Ga_{0.88}N$	350
GaN:Si	100
GaN buffer	2000
GaN substrate	60000

Table A.6: Schematic representation of the structural details of sample LD370 investigated in Chapter 6.

LD405	
Composition	Thickness (nm)
$In_{0.18}Ga_{0.82}N$:Mg	3
$In_{0.02}Ga_{0.98}N$:Mg	14
60 x (25Å of $In_{0.02}Ga_{0.98}N$:Mg / 25Å of $In_{0.02}Al_{0.16}Ga_{0.82}N$:Mg)	420
$In_{0.02}Ga_{0.98}N$:Mg	70
$In_{0.02}Al_{0.16}Ga_{0.82}N$:Mg	140
QW: 5 x $In_{0.1}Ga_{0.9}N$	5 x 3
QB: $In_{0.02}Ga_{0.98}N$:Si	7
$In_{0.02}Ga_{0.98}N$:Si	100
GaN:Si	40
$Al_{0.08}Ga_{0.92}N$:Si	450
GaN:Si	100
GaN buffer	2000
GaN substrate	60000

Table A.7: Schematic representation of the structural details of sample LD405 grown alternatively by PAMBE and investigated in Chapter 6.

Bibliography

[1] A. A. Bergh, *Phys. Stat. Solidi (a)* **201**, 2740 (2004).

[2] S. Nakamura and G. Fasol, *The Blue Laser Diodes*, Springer Verlag, Berlin 1997.

[3] I. data archive.

[4] J. V. Lirman and H. S. Zhdanov, *Acta Physicochem. USSR* **6**, 306 (1930).

[5] W. Utsumi, H. Saitoh, H. Kaneko, T. Watanuki, K. Aoki, and O. Shimomura, *Nature Materials* **2**, 735 (2003).

[6] H. Maruska and J. Tjetjen, *Appl. Phys. Lett.* **15**, 327 (1969).

[7] S. Yoshida, S. Misawa, and S. Gonda, *Appl. Phys. Lett.* **42**, 427 (1983).

[8] H. Amano, N. Sawaki, I. Akasaki, and T. Toyoda, *Appl. Phys. Lett.* **48**, 353 (1986).

[9] S. Nakamura, *Jpn. J. Appl. Phys.* **30**, L1705 (1991).

[10] H. Amano, M. Kito, K. Hiramatsu, and I. Akasaki, *Jpn. J. Appl. Phys.* **28**, L2112 (1989).

[11] S. Nakamura, T. Mukai, M. Senoh, and N. Iwasa, *Jpn. J. Appl. Phys.* **31**, L139 (1992).

[12] S. Nakamura, N. Iwasa, M. Senoh, and T. Mukai, *Jpn. J. Appl. Phys.* **31**, 1258 (1992).

[13] J. Neugebauer and C. V. D. Walle, *Phys. Rev. B* **50**, 8067 (1994).

[14] S. Nakamura and T. Mukai, *Jpn. J. Appl. Phys.* **31**, L1457 (1992).

[15] S. Nakamura, T. Mukai, M. Senoh, S. Nagahama, and N. Iwasa, *J. Appl. Phys.* **74**, 3911 (1993).

[16] S. Nakamura, M. Senoh, S. Nagahama, N. Iwasa, T. Yamada, T. Matsushita, H. Kijoku, and Y. Sugimoto, *Jpn. J. Appl. Phys.* **35**, L74 (1996).

[17] S. Nakamura, M. Senoh, S. Nagahama, N. Iwasa, T. Yamada, T. Matsushita, Y. Sugimoto, and H. Kijoku, *Appl. Phys. Lett.* **69**, 4056 (1996).

[18] S. Nakamura, M. Senoh, S. Nagahama, N. Iwasa, T. Yamada, T. Matsushita, H. Kijoku, Y. Sugimoto, T. Kozaki, H. Umemoto, M. Sano, and K. Chocho, *Jpn. J. Appl. Phys.* **36**, L1568 (1997).

[19] S. Nakamura, M. Senoh, S. Nagahama, N. Iwasa, T. Yamada, T. Matsushita, H. Kijoku, Y. Sugimoto, T. Kozaki, H. Umemoto, M. Sano, and K. Chocho, *Jpn. J. Appl. Phys.* **37**, L627 (1998).

[20] S. Nakamura, M. Senoh, S. Nagahama, T. Matsushita, H. Kijoku, Y. Sugimoto, T. Kozaki, H. Umemoto, M. Sano, and T. Mukai, *Jpn. J. Appl. Phys.* **38**, L226 (1999).

[21] M. Vehse, P. Michler, O. Lange, M. Röwe, J. Gutowski, S. Bader, H. Lugauer, G. Brüdl, A. Weimar, A. Lell, and V. Härle, *Nature Materials* **2**, 735 (2003).

[22] S. D. Lester, F. A. Ponce, M. G. Craford, and D. A. Steigerwald, *Appl. Phys. Lett.* **66**, 1249 (1995).

[23] S. Chichibu, T. Azuhata, T. Sota, and S. Nakamura, *Appl. Phys. Lett.* **69**, 4188 (1996).

[24] S. Nakamura, M. Senoh, S. Nagahama, N. Iwasa, T. Yamada, T. Matsushita, H. Kiyoku, Y. Sugimoto, T. Kozaki, H. Umemoto, M. Sano, and K. Chocho, *Appl. Phys. Lett.* **72**, 211 (1998).

[25] I. Grzegory, *J. Phys.: Condens. Matter* **13**, 6875 (2002).

[26] I.-H. Ho and G. B. Stringfellow, *Appl. Phys. Lett.* **69**, 2701 (1996).

[27] S. Chichibu, H. Marchand, M. S. Minsky, S. Keller, P. T. Fini, J. P. Ibbetson, S. B. Fleicher, J. S. Speck, J. E. Bowers, E. Hu, U. K. Mishra, S. P. DenBaars, T. Deguchi, T. Sota, and S. Nakamura, *Appl. Phys. Lett.* **74**, 1460 (1999).

[28] A. Hangleiter, F. Hitzel, C. Netzel, D. Fuhrmann, U. Russow, G. Ade, and P. Hinze, *Phys. Rev. Lett.* **95**, 127402 (2005).

[29] W. W. Chow and S. W. Koch, *Semiconductor-Laser Fundamentals: Physics of the Gain Materials*, Springer, Berlin, 1999.

[30] B. Witzigmann, V. Laino, M. Luisier, U. T. Schwarz, G. Feicht, W. Wegscheider, K. Engl, M. Furitsch, A. Leber, A. Lell, and V. Härle, *Appl. Phys. Lett.* **88**, 021104 (2006).

[31] Y. Narukawa, Y. Kawakami, S. Fujita, S. Fujita, and S. Nakamura, *Phys. Rev. B* **55**, R1938 (1997).

[32] R. Zimmerman, *J. Cryst. Growth* **101**, 346 (1990).

[33] W. W. Chow, A. Knorr, and S. W. Koch, *Appl. Phys. Lett.* **67**, 754 (1995).

[34] W. W. Chow, A. F. Wrigth, A. Girndt, F. Jahnke, and S. W. Koch, *Appl. Phys. Lett.* **71**, 2608 (1997).

[35] W. W. Chow and S. W. Koch, *GaN and Related Materials II*, Gordon xx Breach, Amsterdam, 2000.

[36] S. Chichibu, T. Azuhata, T. Sota, and S. Nakamura, *Appl. Phys. Lett.* **70**, 2822 (1997).

[37] M. Kuball, E.-S. Jeon, Y.-K. Song, A. V. Nurmikko, P. Kozodoy, A. Abare, S. Keller, L. A. Coldren, U. K. Mishra, S. P. DenBaars, and D. A. Steigerwald, *Appl. Phys. Lett.* **70**, 2580 (1997).

[38] U. T. Schwarz, E. Sturm, W. Wegscheider, V. Kümmler, A. Lell, and V. Härle, *Appl. Phys. Lett.* **85**, 1475 (2004).

[39] W. W. Chow, A. Girndt, and S. W. Koch, *Opt. Express* **2**, 119 (1998).

[40] S. Nakamura, M. Senoh, S. Nagahama, N. Iwasa, T. Yamada, T. Matsushita, H. Kijoku, and Y. Sugimoto, *Appl. Phys. Lett.* **68**, 3269 (1996).

[41] W. W. Chow and H. C. Schneider, *Appl. Phys. Lett.* **81**, 2566 (2002).

[42] W. W. Chow and S. W. Koch, *Semiconductor-Laser Physics*, Springer-Verlag, Berlin, 1994.

[43] L. A. Coldren and S. W. Corzine, *Diode Lasers and Photonic Integrated Circuits*, John Wiley and Sons, Inc., New York, 1995.

[44] D. Courjon, *Near-Field Microscopy and Near-Field Optics*, Imperial College Press, 2003.

[45] T. Tojyo, S. Uchida, T. Mizuno, T. Asano, M. Takeya, T. Hino, S. Kijima, S. Goto, Y. Yabuki, and M. Ikeda, *Jpn. J. Appl. Phys.* **41**, 1829 (2002).

[46] M. Ikeda, T. Mizuno, M. Takeya, S. Goto, S. Ikeda, T. Fujimoto, Y. Ohfuji, and T. Hashizu, *Phys. Stat. Solidi (c)* **1**, 1461 (2004).

[47] S. Uchida, M. Takeya, S. Ikeda, T. Mizuno, T. Fujimoto, O. Matsumoto, S. Goto, T. Tojyo, and M. Ikeda, *J. Sel. Top. Quantum Electron.* **9**, 1252 (2002).

[48] M. W. Fay, G. Moldovan, N. J. Weston, P. D. Brown, I. Harrison, K. P. Hilton, A. Masterton, D. Wallis, R. S. Balmer, M. J. Uren, and T. Martin, *J. Appl. Phys.* **96**, 5588 (2004).

[49] W. Götz, N. M. Johnson, J. Walker, D. P. Bour, and R. A. Street, *Appl. Phys. Lett.* **68**, 667 (1996).

[50] D. P. Bour, *Conf. Lasers and Electro-Optics CLEO* **7** (1999).

[51] W. Götz, N. M. Johnson, C. Chen, H. Liu, C. Kuo, and W. Imler, *Appl. Phys. Lett.* **68**, 3144 (1996).

[52] D. Green, E. Haus, F. Wu, L. Chen, U. Mishra, and J. Speck, *J. Vac. Sci. Technol.* **21**, 1804 (2003).

[53] E. F. Schubert, W. Grieshaber, and I. D. Goepfert, *Appl. Phys. Lett* **69**, 3737 (1996).

[54] T. Lei, M. Fanciulli, R. J. Molnar, T. D. Mauskas, R. J. Graham, and J. Scanlon, *Appl. Phys. Lett.* **59**, 994 (1991).

[55] M. Mizuta, S. Fujieda, Y. Matsumoto, and T. Kawamura, *Jpn. J. Appl. Phys.* **25**, L945 (1986).

[56] O. Ambacher, J. Smart, J. R. Shealy, N. G. Weimann, K. Chu, M. Murphy, W. J. Schaff, L. F. Eastmann, R. Dimitrov, L. Wittmer, M. Stutzmann, and J. H. W. Rieger, *J. Appl. Phys.* **85**, 3222 (1999).

[57] D. V. F. Bernardini, V. Fiorentini, *Phys. Rev. B* **56**, R10024 (1997).

[58] F. Renner, P. Kiesel, G. H. Döhler, M. Kneissl, C. G. V. de Walle, and N. M. Johnson, *Appl. Phys. Lett.* **81**, 490 (2002).

[59] D. Fuhrmann, U. Rossow, C. Netzel, H. Bremers, G. Ade, P. Hinze, and A. Hangleiter, *Phys. Stat. Solidi (c)* **3**, 1966 (2006).

[60] G. Franssen, T. Suski, P. Perlin, R. Bohdan, A. Bercha, W. Trzeciakowski, I. Makarowa, P. Prystawko, M. Leszczyński, I. Grzegory, and S.Porowski, *Appl. Phys. Lett.* **87**, 041109 (2005).

[61] D. A. B. Miller, D. S. Chemla, T. C. Damen, A. C. Gossard, W. Wiegmann, T. H. Wood, and C. A. Burrus, *Phys. Rev. Lett.* **53**, 2173 (1985).

[62] S. Nagahama, Y. Sugimoto, T. Kozaki, Y. Fujimura, S. Nagahama, and T. Mukai, *Proc. SPIE* **57**, 5738 (2005).

[63] M. Ueda, K. Kojima, M. Funato, Y. Kawakami, Y. Narukawa, and T. Mukai, *Appl. Phys. Lett.* **89**, 211907 (2006).

[64] P. Waltereit, O. Brandt, A. Trampert, H. T. Grahn, J. Menniger, M. Ramsteiner, M. Reiche, and K. H. Ploog, *Nature* **406**, 865 (2000).

[65] B. A. Haskell, F. Wu, S. Matsuda, M. D. Craven, P. T. Fini, S. P. DenBaars, J. S. Speck, and S. Nakamura, *Appl. Phys. Lett.* **83**, 1554 (2003).

[66] J. Piprek, *Nitride Semiconductor Devices*, Viley-VCH Verlag, 2007.

[67] A. Kuramata, K. Horino, and K. Domen, *Fujitsu Sci. Tech. J.* **34**, 191 (1998).

[68] S. Nakamura, M. Senoh, S. Nagahama, N. Iwasa, T. Yamada, T. Matsushita, H. Kiyoku, and Y. Sugimoto, *Appl. Phys. Lett.* **68**, 2105 (1996).

[69] P. D. Brewer, D. H. Chow, and R. H. Miles, *J. Vac. Sci. Technol. B* **14**, 2335 (1996).

[70] I. Grzegory, M. Boćkowski, B. Łucznik, S. Krukowski, Z. Romanowski, M. Wróblewski, and S. Porowski, *J. Cryst. Growth* **246**, 177 (2002).

[71] J. Weyher, S. Müller, I. Grzegory, and S. Porowski, *J. Cryst. Growth* **182**, 17 (1997).

[72] S.-B. Che, W. Terashima, Y. Ishitani, A. Yoshikawa, T. Matsuda, H. Ishii, and S. Yoshida, *Appl. Phys. Lett* **86**, 261903 (2005).

[73] S. Keller, N. A. Fichtenbaum, M. Furukawa, J. S. Speck, S. P. DenBaars, and U. K. Mishra, *Appl. Phys. Lett.* **90**, 191908 (2007).

[74] M. Leszczyński, P. Prystawko, R. Czernecki, J. Lehnert, T. Suski, P. Perlin, P. Wiśniewski, I. Grzegory, G. Nowak, S. Porowski, and M. Albrecht, *J. Cryst. Growth* **231**, 352 (2001).

[75] A. Ishizaka and Y. Murata, *J. Phys.: Condens. Matter* **6**, L693 (1994).

[76] B. Heying, I. Smorchkova, C. Poblenz, C. Elsass, P. Fini, S. D. Baars, U. Mishra, and J. S. Speck, *Appl. Phys. Lett.* **77**, 2885 (2000).

[77] C. Adelmann, J. Brault, D. Jalabert, P. Gentile, H. Mariette, G. Mula, and B. Daudin, *J. Appl. Phys.* **91**, 9638 (2002).

[78] J. Neugebauer, T. K. Zywietz, M. Scheffler, J. E. Northrup, H. Chen, and R. M. Feenstra, *Phys. Rev. Lett.* **90**, 056101 (2003).

[79] C. Skierbiszewski, P. Wiśniewski, M. Siekacz, P. Perlin, A. Feduniewicz-Żmuda, G. Nowak, I. Grzegory, M. Leszczyński, and S. Porowski, *Appl. Phys. Lett* **88**, 221108 (2006).

[80] B. Heying, E. J. Tarsa, C. R. Elsass, P. Fini, S. P. DenBaars, and J. S. Speck, *J. Appl. Phys.* **85**, 6470 (1999).

[81] S. Krukowski, C. Skierbiszewski, P. Perlin, M. Leszczynski, M. Bockowski, and S. Porowski, *Acta Phys. Polonica B* **37**, 1265 (2006).

[82] I. Smorchkova, E. Haus, B. Heying, P. Kozodoy, P. Fini, J. Ibbetson, S. Keller, S. DenBaars, J. Speck, and U. Mishra, *Appl. Phys. Lett* **76**, 718 (2000).

[83] V. Ramachandran, R. Feenstra, W. Sarney, L. Salamanca-Riba, J. Northrup, L. Romano, and D. Greve, *Appl. Phys. Lett.* **75**, 808 (1999).

[84] L. Romano, J. Northrup, A. Ptak, and T. Myers, *Appl. Phys. Lett.* **77**, 2479 (2000).

[85] H. Emmerich and C. Eck, *Continuum Mech. Thermodyn.* **17**, 373 (2006).

[86] T. Böttecher, S. Figge, S. Einfeldt, R. Chierchia, R. Kröger, C. Petter, C. Zellweger, H. Bühlmann, M. Dieselberg, D. Rudolff, J. Christen, H. Heinke, P. Ryder, M. Ilegems, and D. Hommel, *Phys. Stat. Solidi (c* **0**, 1846 (2003).

[87] M. Kneissl, D. B. Bour, L. Romano, C. G. V. de Walle, J. E. Northrup, W. S. Wong, D. W. Treat, M. Teepe, T. Schmidt, and N. M. Johnson, *Appl. Phys. Lett.* **77**, 1931 (2000).

[88] G. Franssen, a. S. S. Grzanka, Ł. Marona, T. Riemann, J. Christen, H. Teisseyre, P. Valvin, P. Lefebvre, P. Perlin, R. Czernecki, M. Leszczyński, and I. Grzegory, *J. Appl. Phys.* **97**, 103507 (2005).

[89] O. Gelhausen, H. N. Klein, M. R. Phillips, and E. M. Goldys, *Appl. Phys. Lett.* **81**, 3747 (2002).

[90] V. Tokranov, M. Yakimov, A. Katsnelson, M. Lamberti, and S. Oktyabrsky, *Appl. Phys. Lett.* **83**, 833 (2003).

[91] S. Yamasaki, S. Asami, N. Shibata, M. Koike, K. Manabe, T. Tanaka, H. Amano, and I. Akasaki, *Appl. Phys. Lett.* **66**, 1112 (1995).

[92] *SiLENSE Physics Summary STR, Inc., http://semitech.us/products/SiLENSE* .

[93] P. G. Eliseev, M. Osinski, H. Li, and I. V. Akimova, *Appl. Phys. Lett.* **75**, 3838 (1999).

[94] J. Lee, P. G. Eliseev, M. Osinski, D. S. Lee, D. I. Florescu, S. Guo, and M. Pophristic, *IEEE J. Sel. Top. Quantum Electron.* **9**, 1239 (2003).

[95] P. G. Eliseev and M. O. J. Lee, *Quantum Electron.* **34**, 1127 (2004).

[96] H. Schneider and K. V. Klitzing, *Phys. Rev. B* **38**, 6160 (1988).

[97] S. Kan, D. Vassilovski, and K. L. T. C. Wu, *IEEE Photonics Technol. Lett.* **4**, 428 (1992).

[98] C. Y. Tsai, C. Y. Tsai, Y. H. Lo, R. M. Spencer, and L. F. Eastman, *IEEE J. Sel. Top. Quantum Electron* **1**, 316 (1995).

[99] M. Grupen and K. Hess, *IEEE J. Quantum Electron.* **34**, 120 (1998).

[100] T. Akasaka, H. Gotoh, T. Saito, and T. Makimoto, *Appl. Phys. Lett.* **85**, 3089 (2004).

[101] T. Akasaka, H. Gotoh, Y. Kobayashi, H. Nakano, and T. Makimoto, *Appl. Phys. Lett.* **89**, 101110 (2006).

[102] M. Lundstrom, *Fundamentals of carrier transport*, Cambridge University Press, 2000.

[103] L. Davis, Y. L. Lam, Y. C. Chen, J. Singh, and P. K. Bhattacharya, *IEEE J. Quantum Electr.* **30**, 2560 (1994).

[104] H. Y. Ryu, K. H. Ha, S. N. Lee, T. Jang, H. K. Kim, J. H. Chae, K. S. Kim, K. K. Choi, J. K. Son, H. S. Paek, Y. J. Sung, T. Sakong, O. H. Nam, and Y. J. Park, *Appl. Phys. Lett.* **89**, 031122 (2006).

[105] R. Kersting, R. Schwedler, K. Wolter, K. Leo, and H. Kurz, *Phys. Rev.* **B46**, 1639 (1992).

[106] P. Kozodoy, H. Xing, S. D. Baars, U. Mishra, A. Saxler, R. Perrin, S. Elhamri, and W. Muitchel, *Phys. Rev. A* **46**, 7179 (1992).

[107] V. Bougrov, M. E. Levinshtein, S. L. Rumyantsev, and A. Zubrilov, *Properties of Advanced SemiconductorMaterials GaN, AlN, InN, BN, SiC, SiGe*, John Wiley Sons, Inc., New York, 2001.

[108] S. Grzanka, G. Franssen, G. Targowski, K. Krowicki, T. Suski, R. Czernecki, P. Perlin, and M. Leszczyński, *Appl. Phys. Lett.* **90**, 103507 (2007).

[109] H. P. D. Schenk, M. Leroux, and P. de Mierry, *J. Appl. Phys.* **88**, 1525 (2000).

[110] *Crosslight Software Inc., Laser Technology Intergated Program LASTIP, http://www.crosslight.com* .

[111] K. Domen, R. Soejima, A. Kuramata, K. Horino, S. Kubota, and T. Tanahashi, *Appl. Phys. Lett.* **73**, 2775 (1998).

[112] Y. K. Kuo and Y. A. Chang, *IEEE J. Quantum Electron.* **10**, 437 (2004).

[113] S. W. Lee, D. C. Oh, H. Goto, J. S. Ha, H. J. Lee, T. Hanada, M. W. Cho, T. Yao, S. K. Hong, H. Y. Lee, S. R. Cho, J. W. Choi, J. H. Choi, J. H. Jang, J. E. Shin, and J. S. Lee, *Appl. Phys. Lett.* **89**, 132117 (2006).

[114] Y. C. Shen, G. O. Mueller, S. Watanabe, N. F. Gardner, A. Munkholm, and M. R. Krames, *Appl. Phys. Lett.* **91**, 141101 (2007).

[115] C. Pflügl, M. Litzenberger, W. Schrenk, D. Pogany, E. Gornik, and G. Strasser, *Appl. Phys. Lett.* **82**, 1664 (2003).

[116] B. W. Hakki and T. L. Paoli, *J. Appl. Phys.* **44**, 4113 (1973).

[117] P. W. Milonni and J. H. Eberly, *Lasers*, John Wiley Sons, New York, 1988.

[118] A. Žukauskas, K. Kažlauskas, G. Tamulaitis, P. Pobedinskas, S. Juršėnas, S. Miasojedovas, V. Ivanov, M. Godlewski, C. Skierbiszewski, M. Siekacz, G. Franssen, P. Perlin, T. Suski, and I. Grzegory, *Phys. Stat. Solidi (b)* **243**, 1614 (2006).

[119] Y.-H. Cho, T. J. Schmidt, S. Bindyk, G. H. Gainer, J. J. Song, S. Keller, U. K. Mishra, and S. P. DenBaars, *Physical Rev. B* **61**, 7571 (2000).

[120] L. D. Negro, P. Bettotti, M. Cazzanelli, D. Pacifici, and L. Pavesi, *Optics Comm.* **229**, 337 (2004).

[121] P. S. Cross and W. G. Oldham, *I EEE J. Quantum Electr.* **QE-11**, 190 (1975).

[122] F. Binet, J. Y. Duboz, J. Off, and F. Scholz, *Phys. Rev. B* **60**, 4715 (1999).

[123] J. Shah, *Solid-State Electron.* **21**, 43 (1978).

[124] S. A. Lyon, *J. Lumin.* **35**, 121 (1986).

[125] A. Hangleiter, D. Fuhrmann, M. Grewe, F. Hitzel, G. Klewer, S. Lahmann, C. Netzel, N. Riedel, and U. Russow, *Phys. Stat. Solidi (a)* **201**, 2808 (2004).

[126] G. Biwa, H. Yaguchi, K. Onabe, and Y. Shiraki, *J. Cryst. Growth* **195**, 574 (1998).

[127] H. Ishikawa, S. Kobayashi, Y. Koide, S. Yamasaki, S. Nagai, J. Umezaki, M. Koike, and M. Murakami, *J. Appl. Phys.* **81**, 1315 (1997).

[128] P. Perlin, Wiśniewski, R. Czernecki, P. Prystawko, M. Leszczyński, T. Suski, I. Grzegory, Ł. Marona, T. Świetlik, K. Komorowska, and S. Porowski, *Proc. SPIE* **6184**, 61840H (2006).

[129] V. Kümmler, G. Brüderl, S. Bader, S. Miller, A. Weimar, A. Lell, V. Härle, U. T. Schwarz, N. Gmeinwieser, and G. Wegscheider, *Phys. Stat. Solidi (a)* **194**, 419 (2002).

[130] S.-N. Lee, S. Y. Cho, H. Y. Ryu, J. K. Son, H. S. Paek, T. Sakong, T. Jang, K. K. Choi, K. H. Ha, M. H. Yang, O. H. Nam, Y. Park, and E. Yoon, *Appl. Phys. Lett.* **88**, 111101 (2006).

[131] S. P. Łepkowski and S. Krukowski, *J. Appl. Phys.* **100**, 016103 (2006).

[132] S. Nagahama, N. Iwasa, M. Senoh, T. Matsutshita, Y. Sugimoto, H. Kiyoku, M. Sano, H. Matsumura, H. Umemoto, K. Chocho, and T. Mukai, *Jpn. J. Appl. Phys.* **39**, L647 (2000).

[133] M. Röwe, P. Michler, J. Gutowski, S. Bader, G. Brüderl, V. Kümmler, S. Miller, A. Weimar, A. Lell, and V. Härle, *Phys. Stat. Solidi (a)* **194**, 414 (2002).

[134] T. Asano, M. Takeya, T. Mizuno, S. Ikeda, K. Shibuya, T. Hino, S. Uchida, and M. Ikeda, *Appl. Phys. Lett.* **80**, 3497 (2002).

[135] M. Ikeda and S. Uchida, *Phys. Stat. Solidi (a)* **194**, 407 (2002).

[136] V. Laino, F. Roemer, B. Witzigmann, C. Lauterbach, U. T. Schwarz, C. Rumbolz, M. O. Schillgalies, M. Furitsch, A. Lell, and V. Härle, *IEEE J. Quant. Electron.* **43**, 16 (2007).

[137] G. A. Smolyakov, P. G. Eliseev, and M. Osinski, *IEEE J. Quantum Electron.* **41**, 517 (2005).

[138] U. T. Schwarz, M. Pindl, E. Sturm, M. Furitsch, A. Leber, S. Miller, A. Lell, , and V. Härle, *Phys. Stat. Solidi (a)* **202**, 261 (2005).

[139] J. K. Son, J. S. Hwang, S. N. Lee, T. Sakong, H. Paek, S. Chae, H. K. Kim, O. Nam, J. Y. Kim, Y. H. Cho, and Y. Park, *Phys. Stat. Solidi (c)* **3**, 2178 (2006).

[140] P. Perlin, T. Suski, M. Leszczyński, P. Prystawko, T. Świetlik, Ł. Marona, P. Wiśniewski, R. Czernecki, G. Nowak, J. L. Weyher, G. Kamler, J. Borysiuk, E. Litwin-Staszewska, L. Dmowski, R. Piotrzkowski, G. Franssen, S. Grzanka, I. Grzegory, and S. Porowski, *J. Cryst. Growth* **281**, 107 (2005).

[141] J. I. Pankove, *Optical Processes in Semiconductors*, Courier Dover Publications, 1975.

[142] O. Ambacher, W. Rieger, P. Ansmann, H. Angerer, T. Moustakas, and M. Stutzman, *Sol. State Commun.* **5**, 97 (1996).

[143] R. Stöckle, C. Fokas, V. Deckerrt, R. Zenobi, B. Sick, B. Hecht, and U. P. Wild, *Appl. Phys. Lett* **75**, 161 (1999).

[144] A. Lazarev, N. Fang, Q. Luo, and X. Zhang, *Rev. Sci. Instrum.* **74**, 3679 (2003).

[145] U. T. Schwarz, C. Lauterbach, M. O. Schillgalies, C. Rumbolz, M. Furitsch, A. Lell, and V. Härle, *Proc. SPIE* **6184**, 61840K (2006).

[146] R. Toledo-Crow, P. Yang, Y. Chen, and M. Vaez-Iravani, *Appl. Phys. Lett.* **60**, 2957 (1992).

[147] E. Betzig, P. Finn, and S. Weiner, *Appl. Phys. Lett.* **60**, 2484 (1992).

[148] M. Gregor, P. Blome, J. Schöfer, and R. Ulbrich, *Appl. Phys. Lett.* **68**, 307 (1996).

[149] C. Sasaoka, K. Fukuda, M. Ohya, K. Shiba, M. Sumino, S. Kohomoto, K. Naniwae, M. Matsudate, E. Mizuki, I. Masumoto, R. Kobayashi, K. Kudo, T. Sasaki, and K. Nishi, *Phys. Stat. Solidi (a)* **203**, 1824 (2006).

[150] C. Eichler, D. Hofstetter, W. W. Chow, S. Miller, A. Weimer, A. Lell, and V. Härle, *Appl. Phys. Lett.* **84**, 2473 (2004).

[151] U. T. Schwarz, M. Pindl, W. Wegscheider, C. Eichler, F. Scholz, M. Furtisch, A. Leber, S. Miller, A. Lell, and V. Härle, *Appl. Phys. Lett.* **86**, 161112 (2005).

[152] C. Eichler, S.-S. Schad, M. Seyboth, F. Habel, M. Scherer, S. Miller, A. Weimar, A. Lell, C. Härle, and D. Hofstetter, *Phys. Stat. Solidi (c)* **0**, 2283 (2003).

[153] U. Tisch, B. Meyler, O. Katz, E. Finkman, and J. Salzman, *J. Appl. Phys.* **89**, 2676 (2001).

[154] W. W. Chow and H. Amano, *IEEE J. Quantum Electron.* **37**, 265 (2001).

[155] W. W. Chow, H. Amano, and I. Akasaki, *Appl. Phys. Lett.* **76**, 1647 (2000).

[156] U. T. Schwarz, E. Sturm, W. Wegscheider, V. Kümmler, A. Lell, and V. Härle, *Appl. Phys. Lett.* **83**, 4095 (2003).

[157] K. J. Beernink, J. J. Alwan, and J. J. Coleman, *J. Appl. Phys.* **69**, 56 (1991).

[158] G. Hunziker, W. Knop, P. Unger, and C. Harder, *IEEE J. Quant. Electr.* **31**, 643 (1995).

[159] M. Röwe, P. Michler, J. Gutowski, S. Bader, G. Brüderl, V. Kümmler, A. Weimar, A. Lell, and V. Härle, *Phys. Stat. Solidi (a)* **188**, 65 (2001).

[160] U. T. Schwarz, E. Sturm, W. Wegscheider, V. Kümmler, A. Lell, and V. Härle, *Phys. Stat. Solidi (a)* **200**, 143 (2003).

[161] M. J. Bergmann and H. C. Casey, *J. Appl. Phys.* **84**, 1196 (1998).

[162] P. G. Eliseev, G. A. Smolyakov, and M. Osinski, *IEEE J. Sel. Top. Quant. Electron.* **5**, 771 (1999).

[163] C. Henry, R. A. Logan, and F. R. Meritt, *J. Appl. Phys.* **51**, 3042 (1980).

[164] P. Blood, A. I. Kucharska, J. P. Jacobs, and K. Griffiths, *J. Appl. Phys.* **70**, 1144 (1991).

[165] H. C. Casey and M. B. Panish, *Heterostructure Lasers*, Academic Press, New York, 1978.